Finite element analysis of suspension elements for gravitational wave detectors

Rahul Kumar, B.Sc.
Department of Physics and Astronomy,
University of Glasgow

Presented as a thesis for the degree of M.Sc. by research in the University of Glasgow, University Avenue, Glasgow G12 8QQ.

August 2008

Contents

List of figures

List of tables

Acknowledgements

I would first of all like to thank my supervisor Prof. Sheila Rowan for the guidance and support she provided me throughout my entire MSc. I would also like to thank my second supervisor Dr. Calum Torrie under whom I learned a lot and had a great experience.

I would like to thank Prof. Jim Hough for providing me the opportunity to work in this wonderful group (IGR). Without his intellectual support and continuous guidance the work carried out in this thesis would not have been possible.

My thanks go to Dr. Mark Barton and Dr. Alastair Heptonstall for helpful discussion on various topics. I would also like to thank Dr. G Hammond for fabricating fibre for me, Dr. Liam Cunningham for his ANSYS support and thanks to Russell Jones for his Solidworks drawings. I would also like to thank Alan Cumming for being a great colleague and for providing valuable help every time I needed. I would also like to thank all my present office mates (Alan, Stuart, Peter, Marielle, Ian, Ricardo, Karen and Eleanor) and my ex-office mates (Borja, Kirill, Jamie), it was fun working with you all.

On a personal front I would like to thank my mother and father for supporting me throughout my education and also my sister Aditi. Last but not the least, I would like to thank my friends back in India and here in Glasgow too for being there for me whenever required.

Preface

This thesis is an account of the work carried out between October 2006 and July 2008 on finite element analysis of suspension elements for long baseline gravitational wave detectors.

The introduction to gravitational waves and their production is discussed in chapter one. The sources and techniques for their detection have been described here. The information provided in this chapter has been derived from published literature.

In chapter two the thermal noise issues and their sources in the gravitational wave detectors are discussed. The theory of dissipation dilution and thermoelastic effect has been explained here. The information given in this chapter has been derived from published literature.

In chapter three an introduction to the finite element (F. E) analysis method is given. The F. E analysis has been performed using licensed software ANSYS®, version 11.0 from ANSYS®, incorporated. Description of various analysis methods and modelling of a simple structure in ANSYS® are illustrated here. The theory presented in this chapter has been derived from published literature. Modelling of the structure was done by the author in consultation with C. Torrie.

In chapter four, modelling of a single wire fused silica suspension in ANSYS® is discussed. The designs in ANSYS® were modelled by the author and were done in consultation with C. Torrie, A. Heptonstall and L. Cunningham. The analysis of the pendulum mode of

vibration and development of the technique for the estimation of dissipation dilution factor using finite element modelling were carried out by the author, under the guidance of J. Hough, S. Rowan and M. Barton. The MATLAB® code used for verification of mode frequencies was developed by C. Torrie. The work on fibres of circular cross section was done by the author whereas the structures of the ribbons of rectangular cross section were the work of A. Cumming.

In chapter five a pendulum model having two wires suspending a mass of 20 kg is discussed. The two wire pendulum design was modelled to verify the techniques developed in chapter four before modelling the suspension system for the Advanced LIGO detector. The technique required to build a two wire model in ANSYS® was developed by the author in conjunction with C. Torrie. The CAD® models (Solidworks) were provided by C. Torrie and L. Cunningham.

In chapter six the Advanced LIGO suspension system is discussed. Based on the techniques developed in chapter four and five, the suspension elements of the Advanced LIGO detector have been analysed. Here too the work on silica fibres was carried out by the author and the analysis of ribbons were carried out by A. Cumming. The CAD® (Solidworks) models for the test mass and MATLAB® codes for analytically determining the mode frequencies were provided by C. Torrie. The real silica fibre was fabricated in the laboratory by G. Hammond. The profiling of the real silica fibre and the development of codes required for building an ANSYS® model of the same was the work of A. Cumming.

In chapter seven the optimisation of the Advanced LIGO fibre design to minimise the thermoelastic loss is discussed. F. E analysis of this new fibre design was carried out by the author in conjunction with A. Cumming. The estimation of the mechanical loss in the Advanced LIGO suspension system was carried out by A. Heptonstall and A. Cumming.

Summary

Finite element analysis of suspension elements for gravitational wave detectors

The existence of gravitational waves was predicted by Einstein in 1916 in his General Theory of Relativity. Gravitational waves are considered as ripples in space-time, however there has been no direct evidence to prove their existence. Scientists around the world are engaged in the development of instruments to detect gravitational wave signals. Once these waves are detected new avenues will be opened up in the field of Physics and Astronomy.

Gravitational waves are quadrupole in nature and produce a tidal strain in space. They interact weakly with matter making them difficult to detect. The strains expected for gravitational waves which may be detected on earth are of the order of 10^{-22} to 10^{-23} (over a frequency range from few Hz to a few kHz). A network of instruments based on long baseline Michelson interferometers is being developed around the world, which should be sensitive enough to detect such strains.

The Institute for Gravitational Research in the University of Glasgow in collaboration with the Albert Einstein Institute in Hannover and Golm and the University of Cardiff has been actively involved in the research for the development of instruments and data analysis techniques to detect gravitational waves. This includes construction of a long ground based

interferometer in Germany called GEO 600 having an arm length 600 m and strong involvement in the larger detectors of the LIGO (Laser interferometer gravitational wave observatory) project in USA having arm lengths of 4 km. An upgrade to LIGO called Advanced LIGO has been proposed and is currently under development with significant input from Glasgow.

The work in this thesis discusses the finite element analysis of suspension elements for the Advanced LIGO detectors. The Advanced LIGO suspensions have a quasi monolithic quadruple pendulum design with final stages comprised of four fused silica fibres or ribbons suspending a 40 kg test mass mirror. Minimising the mechanical loss in the pendulum and hence lowering the thermal noise in the suspension system is a fundamental requirement for increasing the sensitivity of the detector and this has been studied here by analysing the suspension elements of the final stage of pendulum system.

Thermal noise is one of the most significant noise sources for gravitational wave detectors. It arises due to the random fluctuations of atoms and molecules in the materials of the test mass mirrors and suspension elements and is related to mechanical loss in these materials. This thesis is devoted to analysis of aspects of mechanical loss in the final stages of the suspension system. This requires modelling the energy distribution in the suspension elements and hence estimating what is known as the ‘dissipation dilution’ of the pendulum. The dissipation dilution factor of a pendulum plays an important role in reducing the mechanical loss in the pendulum and results from the fact that most of the energy associated with the pendulum is stored in the lossless gravitational field of the earth. Mechanical loss can result from internal frictional effects in materials or external frictional effects or thermoelastic effect. The thermoelastic effect tends to be most important of these

for the elements of the suspension system. Minimising the thermoelastic loss in the suspension elements is an important issue for reducing the over-all thermal noise.

Before analysing the suspension elements of the Advanced LIGO suspension system, a prototype design was modelled in ANSYS®. This was of a single fibre or ribbon pendulum system suspending a 10 kg mass (which approximately makes a quarter of the Advanced LIGO pendulum model). At first, pendulum suspensions comprised of fibres or ribbons of uniform cross-sectional area were analysed and later on fibres or ribbons with tapered ends were included and studied for various taper lengths. The study of tapered ends in a fibre or ribbon is very important as any real system requires such necks for joining purposes. Through this model, important aspects of the pendulum design were studied which included the modelling of the strain energy distribution in the fibres or ribbons, with the help of which the dilution factor of the pendulum was estimated. The most important finding from this chapter was the extent to which the tapered ends reduced the dilution factor of the pendulum.

The single fibre pendulum design was then extended to a two-fibre pendulum system comprising of a 20 kg mass. This model was studied as a step between the single fibre pendulum system of the last chapter and the four fibres/ribbons system for the Advanced LIGO detector. There are some other important issues in the two-fibre pendulum model which were observed while studying it and these are related to coupling of the pendulum and tilt modes which leads to reduced dilution factor. The importance of attaching the fibre or ribbons close to a plane through the centre of mass becomes very clear.

The Advanced LIGO suspension system was then modelled. The focus was on comparing the performance of silica fibres and ribbons and the associated dissipation dilution factor of the pendulum system. Similar to the single fibre and two fibre pendulum cases, here the fibres or ribbons were first studied as having uniform cross section and then for tapered ends. Further the performance achievable using real fibres and ribbons fabricated in the laboratory was also evaluated. The strain energy distribution in these suspension elements was found in order to compare their performance and again it was found that the dissipation dilution factor was seriously impaired compared with that of uniform fibres or ribbons.

Finally given the poor dilution factor which can realistically be obtained, it became very important to investigate whether the major factor contributions to the material loss, i.e. the thermoelastic effect could be reduced. This can be achieved by tailoring the stress level at the point where the fibres or ribbons bends. Realistic designs of fibres or ribbons were analysed and shown to be acceptable for use in the Advanced LIGO detector.

Chapter 1

Gravitational waves and their detection

1.1 Introduction

Albert Einstein, in his 'General Theory of Relativity' proposed the existence of gravitational waves in 1916 [3]. Gravitational waves can be described as ripples in the curvature of space-time and perceived as fluctuating tidal forces on the masses in their path. Theoretically, the 'Linearised Einstein Field Equations' show that gravity propagates as a wave in the universe [4].

Work on the detection of gravitational waves was started in 1960 with Joseph Weber [5; 6]. His experiments were not successful in directly detecting gravitational waves; however they stimulated other researchers to build more sensitive detectors and research in this area is still ongoing [7; 8].

Strong evidence for the existence of gravitational waves was provided by work from Hulse [9] and Taylor [10] who were awarded the Nobel Prize for Physics in 1993 for their discovery of the binary pulsar PSR 1913+16 and their subsequent interpretation of the evolution of the orbit of this system. The observation showed the decay of orbital period with time and the corresponding losses of the angular momentum and energy of the system were consistent with the predictions of general relativity for a system radiating gravitational waves. Thus the observations provided indirect evidence for the existence of gravitational waves [11].

At present many groups around the world are working in close collaboration to realize their goal of detecting gravitational waves. The detection of these waves is highly important from an astrophysical point of view. Their detection will provide unique and exciting information about the Universe. Complex phenomena such as the birth, nature and interactions of black holes will be revealed and useful insights will be gained into the collapse of stars. Overall, detection of gravitational waves will open new avenues in astrophysics.

A design of gravitational wave detector which offers high sensitivity over a wide range of frequencies consists of test masses suspended as pendulums whose relative positions are sensed using laser interferometric techniques.

This chapter will discuss the nature of gravitational waves (section 1.2), sources (section 1.3) and some of the techniques for their detection (section 1.4). Finally the noise sources which limit the sensitivity of detectors will be covered in section 1.5.

1.2 The nature of gravitational waves

The gravitational force is the weakest among all the forces in nature. Gravitational waves are produced when matter is accelerated in an asymmetrical way. However due to its weak nature these only reach a level where detection should be possible when very large masses are accelerated in a very strong gravitational field.

In electromagnetism the acceleration of positive and negative charge oscillating about their equilibrium position produces dipole radiation, but in gravity radiation is only from positive mass. This results in the gravitational radiation being quadrupole in nature which means only non-axisymmetric acceleration of mass will produce gravitational waves [12]. The amplitude *'h'* of the gravitational wave can be defined as the strain it produces in space, given by,

$$h = \frac{2\Delta L}{L}, \tag{1.1}$$

where $\frac{\Delta L}{L}$ is the strain.

Gravitational waves which reach the earth from distant sources have two independent polarizations of amplitude h_+ and $h_\times$. Figure 1.1 shows the effect of the resulting strain on a ring of test particles of diameter L for both polarizations. The diameter of the ring increases by ΔL in one direction and decreases by ΔL in the other direction once a wave propagating perpendicular to the page is incident on it.

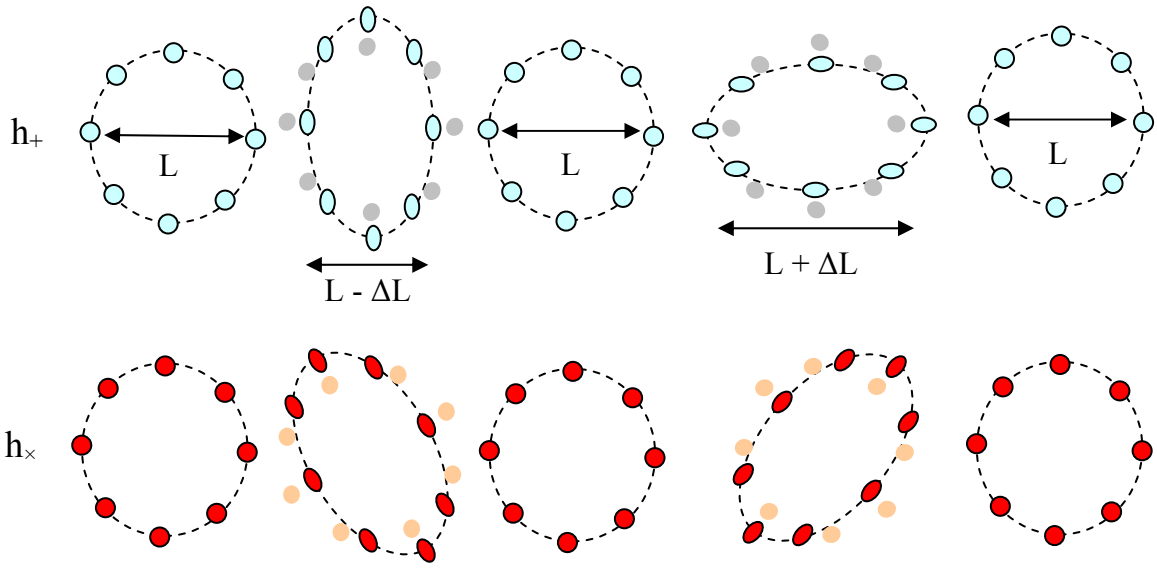

Figure 1.1. The effect of two polarizations of gravitational waves on a ring of test particles, the direction of propagation of wave is perpendicular to the page.

1.3 Sources of gravitational waves

Ground based detectors are expected to detect gravitational waves which have a frequency in the range of a few Hz to few thousand Hz. The sources from which waves may be detectable are outlined in the following subsections.

1.3.1 Burst sources

Supernovae

A supernova is an explosion of a star which causes an extremely luminous burst of radiation. The life of a star is dependent upon the inward and outward pressure which acts on its constituents. The inward pressure is due to the force of gravity. To balance this force outward pressure is produced by thermal radiation from the fusion reaction taking place in the core of the star.

In a star having mass less then approximately 5 solar masses [13], if the fusion reaction stops, when all the hydrogen gets converted into helium, the star would begin to collapse.

Thus a White Dwarf star is formed. If the mass of this star is below the Chandrasekhar limit (1.4 M_Θ) then it will cool down. However if it has a companion star it may start accreting mass from the companion or even merge with it. The companion may be a larger star which does not have a strong enough gravitational force to tightly bind its outer-most layers.

The collapse of the core of a white dwarf star due to accretion of mass is classified as a Type Ia supernova. If the collapse is asymmetric having significant angular momentum, then it will result in emission of gravitational radiation. However if the deformation is symmetric then no gravitational radiation would be emitted.

A larger star may form an iron core which shrinks continuously and is supported by electron degeneracy pressure until its mass exceeds the Chandrasekhar limit. The core of the star would collapse once the electron degeneracy pressure is no longer is able to hold it. If the mass is sufficiently high then the collapse of the core would lead to the formation of a black hole. The collapse of the cores of these larger mass stars is classified as Type II supernovae. Once again if the collapse is asymmetric then gravitational waves would be produced.

The strain amplitude *"h"* as expected from supernovae was given by Schutz [14], and is as follows

$$h \approx 5\times10^{-22}\left(\frac{E}{10^{-3}\mathrm{M}_\Theta c^2}\right)\left(\frac{15\mathrm{Mpc}}{r}\right)\left(\frac{1\mathrm{kHz}}{f}\right)\left(\frac{1\mathrm{ms}}{\tau}\right)^{\frac{1}{2}}, \qquad (1.2)$$

where E is the total energy radiated in the form of gravitational waves, M_Θ is the mass of the sun, c is the speed of light, f is the frequency of the gravitational waves, τ is the time for the collapse to occur and r is the distance from the source.

The event rate for the supernovae out to the VIRGO cluster at a distance of ~ 15 Mpc, is estimated to be several per month [15]. From the fourth science run of the LIGO detectors no gravitational wave signals are detected, with an upper limit of less than 0.15 events per day at signal level greater than equal to 5×10^{-21} $Hz^{-1/2}$ [16].

Coalescing compact binaries

A compact binary system can be defined as a combination of two compact stars (e.g. neutron stars or black holes) orbiting around a common centre of mass. Compact binary systems exists in these forms: neutron / neutron star (NS/NS), black hole / black hole (BH/BH) and neutron star / black hole (NS/BH) combinations. In a binary system like PSR 1913+16, the orbital period decreases because of the loss of energy in the form of gravitational waves. As the distance between the two stars decreases, the amplitude and frequency of gravitational radiation increases. In the last few seconds, before the collision of the two stars, the amplitude and frequency values will increase such that it will be observable with the ground based detectors. According to Schutz [14] the estimated strain amplitude for a coalescing neutron star will be

$$h \approx 1\times10^{-23}\left(\frac{100\mathrm{Mpc}}{r}\right)\left(\frac{M_b}{1.2\mathrm{M}_\Theta}\right)^{\frac{5}{3}}\left(\frac{f}{200\mathrm{Hz}}\right)^{\frac{2}{3}}, \qquad (1.3)$$

where $M_b = (M_1M_2)^{3/5} / (M_1+M_2)^{1/5}$ is the "chirp" mass parameter of the binary system, M_1 and M_2 are the masses of the two stars. The other symbols are defined in equation 1.2.

The population of binary systems having black holes is smaller than for neutron stars; however the higher density and mass will lead to larger amplitudes of gravitational radiation which will increase the chances of detection. In the data taken by the LIGO and GEO detectors no evidence has been observed for a neutron star within a distance of 14 Mpc [17].

1.3.2 Periodic sources

Pulsars

Pulsars are rotating neutron stars and a possible source of gravitational waves. Gravitational waves are expected to be emitted as a result of the non-axisymmetric spin of a pulsar. The waves emitted from such a pulsar are expected to have a frequency of twice the pulsar rotational frequency, f_{rot}. The strain amplitude of the radiation from such a source can be estimated to be [18]

$$h \approx 6 \times 10^{-25} \left(\frac{f_{rot}}{500\ \text{Hz}} \right) \left(\frac{1\,\text{kpc}}{r} \right) \left(\frac{\varepsilon}{10^{-6}} \right). \tag{1.4}$$

The measure of the degree of non-symmetry in the star is given by *"ε"*, the equatorial ellipticity.

In 1054, Chinese astronomers recorded the remnant of a supernova in the Crab nebula which is an expected source of gravitational waves at around 60 Hz with an estimated strain amplitude of $h \sim 10^{-24}$, $\varepsilon \sim 7 \times 10^{-4}$, $r = 1.8$ kpc and $f_{rot} = 30$ Hz [18]. From the fifth science runs of the LIGO detectors, the ellipticity of the Crab Pulsar must be smaller than 1.8×10^{-4} [19].

1.3.3 Stochastic sources

The superposition of signals from many sources may lead to the existence of a background of gravitational waves whose amplitude may be high enough to be detected as a stochastic background. A single detector will not be able to distinguish these stochastic backgrounds from the presence of noise. Hence a combination of several detectors can be used to cross-correlate the data and separate the stochastic background from the random noise.

Assuming the cosmic string scenario for the formation of structure in the universe, a level of background radiation can be predicted whose amplitude is given by [20],

$$h \approx 2.4 \times 10^{-25} \left(\frac{H_o}{75 \mathrm{kms}^{-1} \mathrm{Mpc}^{-1}} \right) \left(\frac{\Omega_{gw}}{10^{-8}} \right)^{\frac{1}{2}} \left(\frac{f}{100 \mathrm{Hz}} \right)^{\frac{-3}{2}} \left(\frac{B}{2 \mathrm{Hz}} \right)^{\frac{1}{2}}. \quad (1.5)$$

For bandwidth B about a frequency f where Ω_{gw} is the energy density per logarithmic frequency interval required to close the universe. H_o is the Hubble's constant. From the fourth science run the amplitude of a stochastic background of gravitational waves is found to be less than 6.5×10^{-25} [21].

1.4 Gravitational wave detectors

Gravitational waves cause a very small strain *'h'*, in space time. In order to detect these signals ultra sensitive detectors are required. Designs which are being currently developed include,

- Resonant bar detectors
- Laser interferometers

These two designs are ground based detectors targeted at sources emitting at frequencies above 10 Hz. A space based detector aimed at lower frequency signals is also planned and will be discussed in section 1.6.

1.4.1 Resonant bar detectors

The bar-type detectors were the first ground based detectors and were initially developed by Joseph Weber of University of Maryland about 40 years ago [22]. Each bar consisted of a large cylinder with a mass of several tons which was well isolated from ground

vibrations and acoustic noise in the laboratory [5; 6]. The bars had a resonant mode at ~ 1600 Hz such that a gravitational wave of the same frequency incident on the bar would lead to vibration of the cylinder, thus causing a mechanical strain which would be measured by a transducer and amplifier.

Weber placed his detectors 1000 km apart and searched for coincident excitations, claiming some success. However similar experiments carried out at other laboratories in USA, Germany, Britain and Russia could not duplicate Weber's results and expected amplitudes of gravitational wave signals were at a level that was below the sensitivity of the Weber-type detectors. The development of the resonant bar types of detector continued and sensitivity levels of around 10^{-20} for millisecond pulses have been achieved.

However the bar detectors have a narrow frequency bandwidth and are sensitive only to signals that have significant spectral energy within this bandwidth.

To overcome this limitation, gravitational wave detectors based on laser interferometry have been designed and developed and will be discussed in the next section.

1.4.2 Ground based laser interferometric gravitational wave detector

In 1970, Forward [23] and Weiss [24] started work on laser interferometry for the detection of gravitational waves. A gravitational wave detector based on the technique of laser interferometry offers high sensitivity over a wide range of frequency. These detectors look for the effects of gravitational waves on the position of test masses, suspended as pendulums which are widely separated from each other and isolated against seismic noise. This technique is based on the principle of a "Michelson interferometer" as shown in figure 1.2.

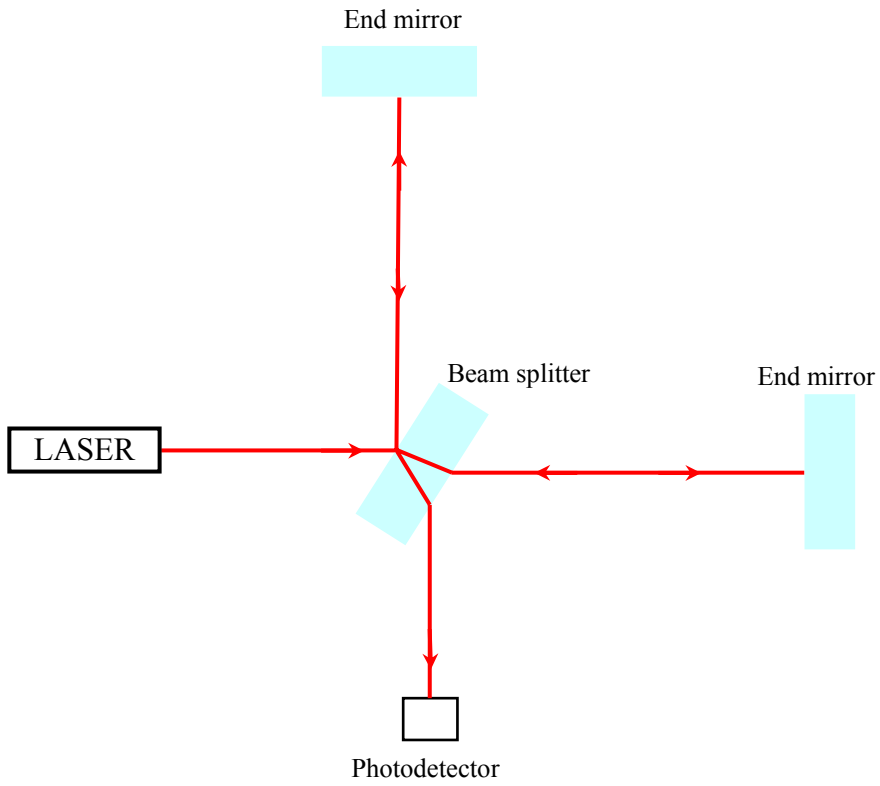

Figure 1.2. Schematic of a simple Michelson interferometer

In a Michelson interferometer light from a laser is incident on a beam splitter where the light is partially reflected and partially transmitted into orthogonal arms, each of similar length L. The light is then reflected back from the end mirrors to the beam splitter where the light is recombined and interference occurs. The interference fringes are then sensed via a photodiode. Any motion of the mirrors changes the relative arm length and thus causes a change in the intensity of the interference pattern. The mirrors are suspended as pendulums and under vacuum so as to isolate them from seismic noise and fluctuation of air pressure.

When a gravitational wave is propagating in a direction perpendicular to the plane of the arms of the interferometer, it produces a fractional change in the arm length, such that one arm will increase by an amount ΔL and the other will decrease by ΔL. Hence it can be

inferred that the detectable signal strength is directly proportional to the length of the arm. The optimum arm length for a wave of frequency 1 kHz can be calculated [12],

$$L_{optimum} = \frac{\lambda_{gw}}{4} \approx 75\text{km}. \tag{1.6}$$

Arm lengths for ground based interferometer are currently limited to around 4 km, due to practical considerations. However a delay line arrangement [24] or a Fabry-Perot cavity in each arm of the instrument [25] can be used to effectively increase the arm length by reflecting the light as shown in figures 1.3 and 1.4.

Delay line interferometer

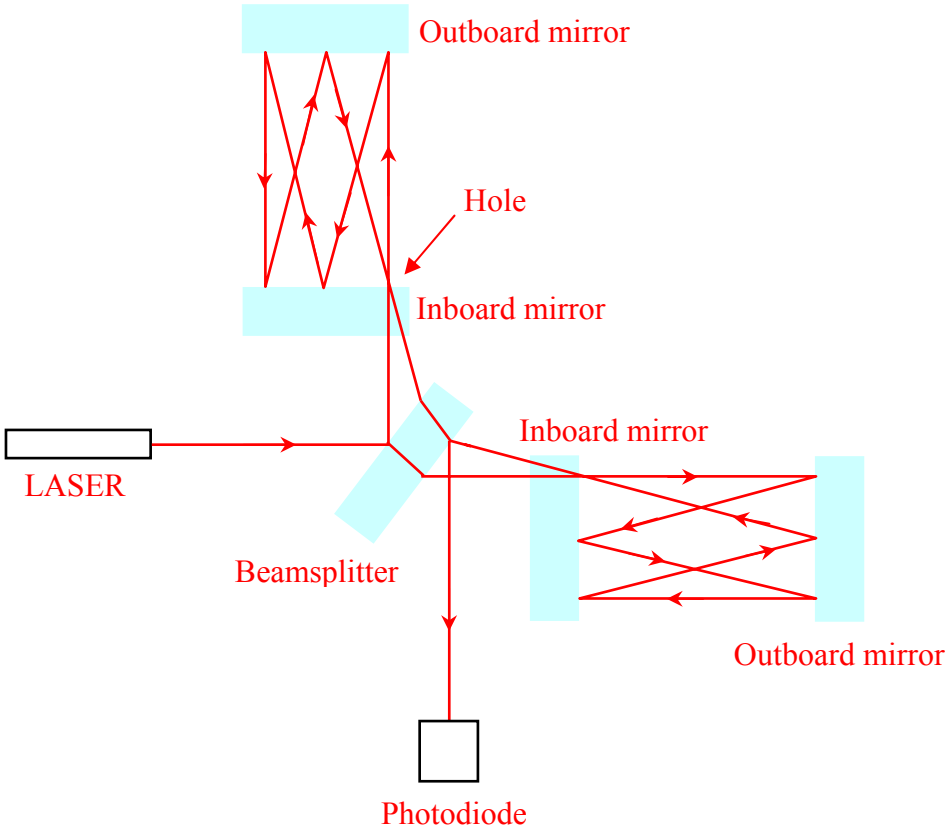

Figure 1.3. Schematic of delay-line interferometer

Proposed by Weiss in the 1970's, the design consists of two additional "inboard mirrors" in between the "beamsplitter" and the "outboard mirrors", as shown in figure 1.3. The reflected or transmitted light from the beamsplitter enters into the inboard mirror through a hole in it. The light then undergoes multiple reflections between the two curved mirrors and thus increases the optical path length. The light then exits the delay line through the same hole.

Fabry-Perot interferometer

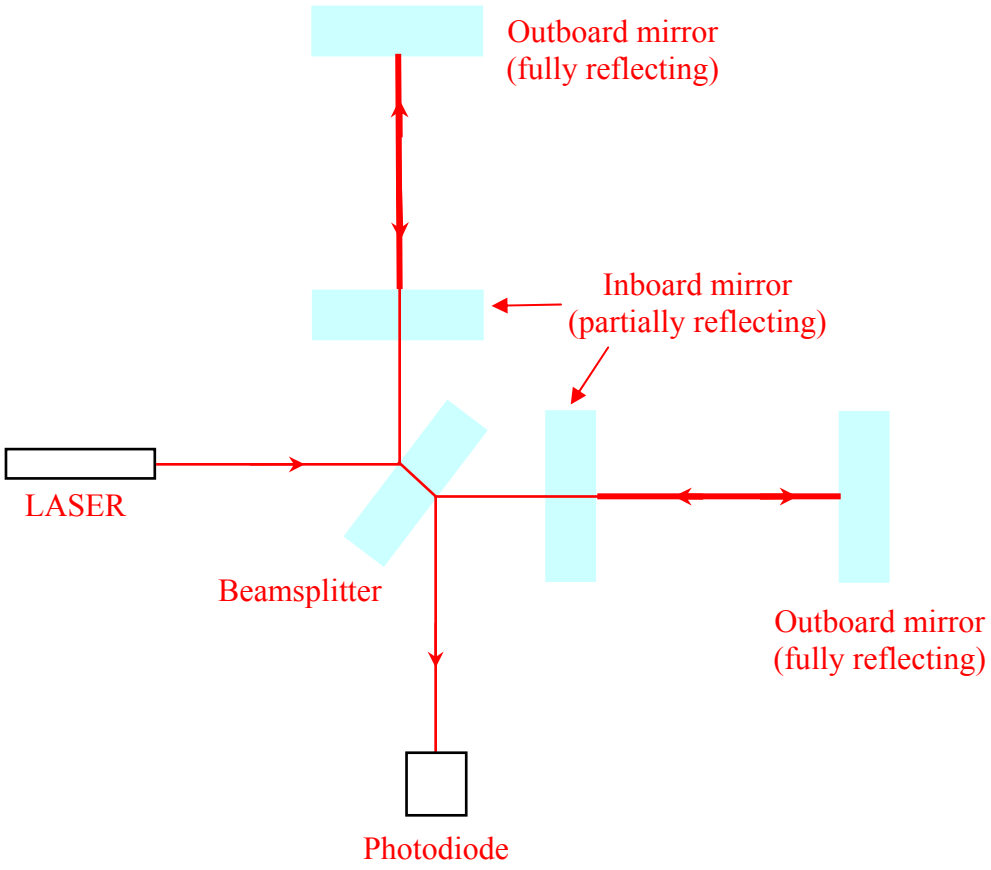

Figure 1.4. Schematic of Fabry-Perot interferometer

The Fabry-Perot interferometer uses Fabry-Perot cavities in the arms of the interferometer so as to increase the storage time. This technique was initially developed in Glasgow in the

early 1980's [25]. The cavities are held at the carrier frequency of the laser light using electronic feedback and actuation systems such that multiple reflections of the light lie on the same spatial path.

One advantage in using this technique rather than the delay-line arrangement is the reduction of noise introduced through scattering of light. However an additional complexity is introduced through the necessity of adding control systems to hold the cavities on resonance.

Power and signal recycling

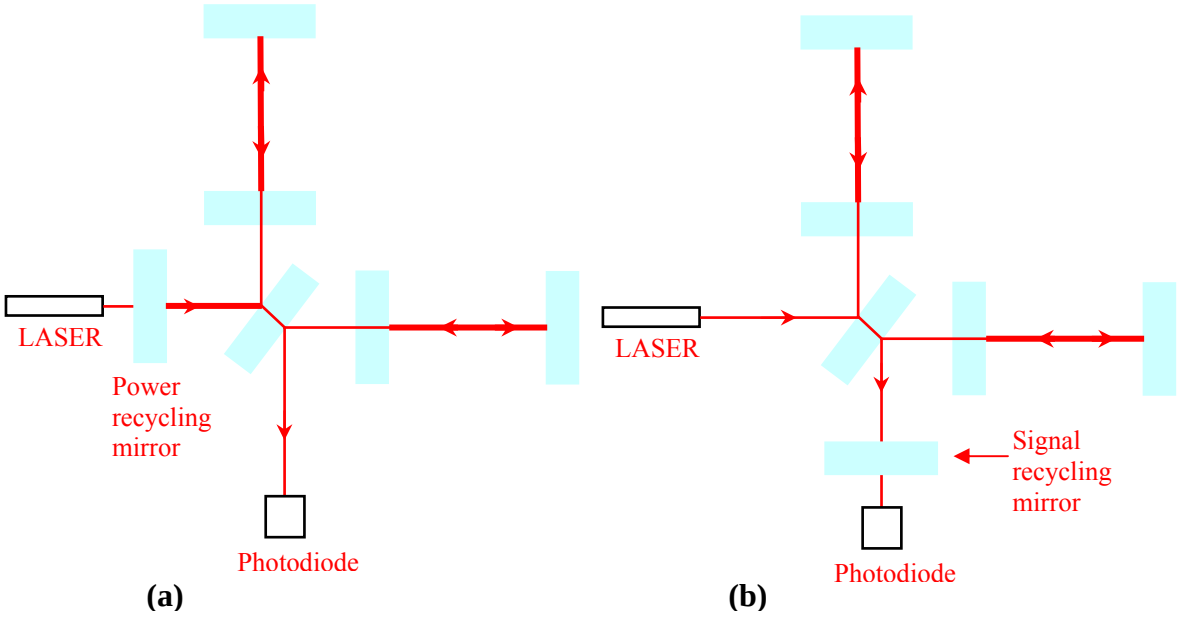

Figure 1.5. Schematic of Fabry-Perot interferometer, (a) - addition of a power recycling mirror and (b) – addition of a signal recycling mirror.

Power recycling is a technique in which an additional mirror is placed before the beam splitter with an intention of re-using the laser light which is coming back from the

interferometer, as shown in figure 1.5 (a). Since the interferometer is operated such that dark fringes are obtained at the output photodiode, to obtain best signal to noise ratio the light exits the interferometer towards the laser. On placing a partially reflecting mirror in between the laser and the beam splitter a resonant cavity can be formed where the interferometer will act as the second mirror [26]. This will increase the laser power and enhance the sensitivity of the instrument.

Similarly, through signal recycling one can reuse the laser light produced by the effect of a gravitational wave signal at the output port to increase the sensitivity of the interferometer. The laser light coming out of the interferometer at the photodiode may be recycled back into the interferometer by placing a partially transmitting mirror in between the beam splitter and the photo diode. This will lead to the formation of an optical cavity between the signal recycling mirror and the interferometer [27]. This will result in an enhancement of the signal produced by an incoming gravitational wave.

1.5 Laser interferometers around the world

A network of laser interferometers for detecting gravitational waves is being built around the world. The LIGO project operates two detector sites; one at Livingston (Louisiana) and one at Hanford (Washington) in USA, each having an interferometer arm length of 4 km with a second half-length instrument also installed in the Hanford vacuum enclosure. An upgraded version of LIGO with improved instrumentation subsystems is currently under development and is called “Advanced LIGO”. The French-Italian collaboration operates the VIRGO detector near Pisa in Italy, whose arm length is 3 km.

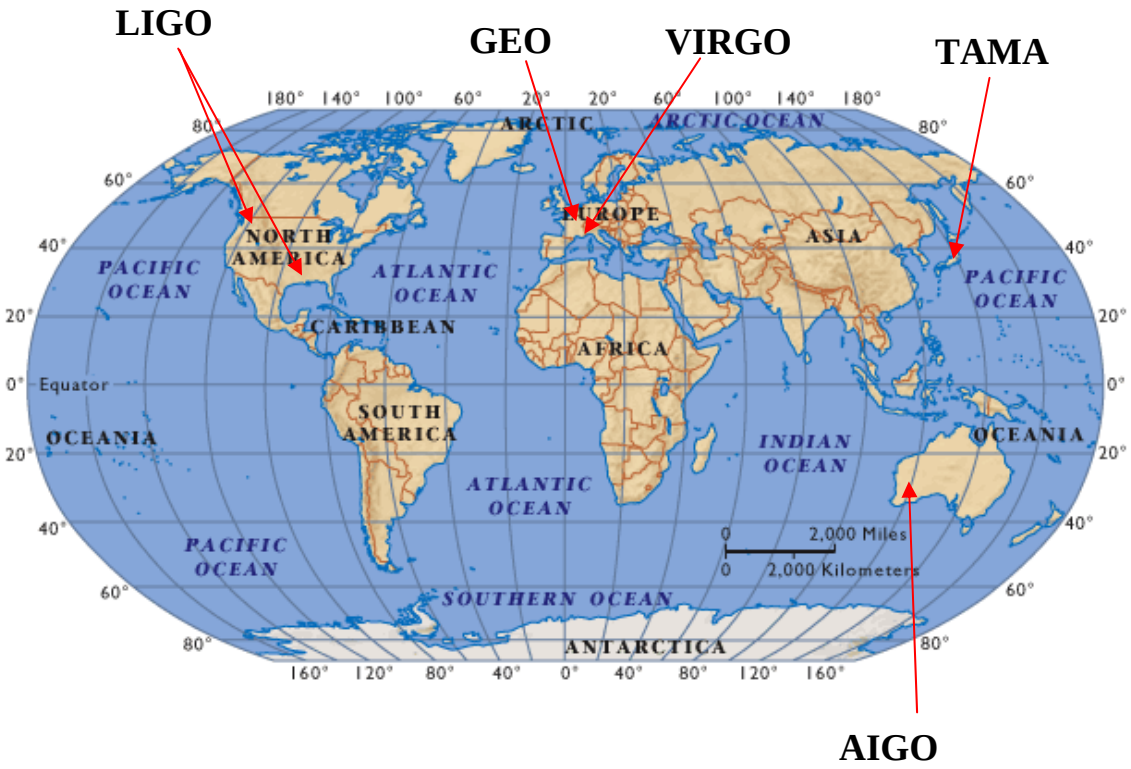

Figure 1.6. Shows the network of major detectors built around the world so as to simultaneously detect signals.

GEO 600 is a German-British project with 600 m arms operating outside Hanover in Germany. In Japan, the 300 m long TAMA detector is running in Tokyo. The AIGO project near Perth in Australia currently has an 80 m prototype detector and has plans to make it longer.

1.6 Space based interferometric detector

The Laser Interferometer Space Antenna (LISA) [28] is a joint project of NASA and ESA (European Space Agency) with a launch planned for 2018. The arm length of the proposed design is 5×10^{9} metres, with three arms forming an equilateral triangle with test masses placed in three separate spacecraft. The strain sensitivity of LISA would be $h \sim 10^{-21}$ / √Hz at 0.1 mHz.

This space based interferometer will complement the ground based detector network by studying gravitational waves from astrophysical sources emitting at frequencies in a band inaccessible to detectors based on earth.

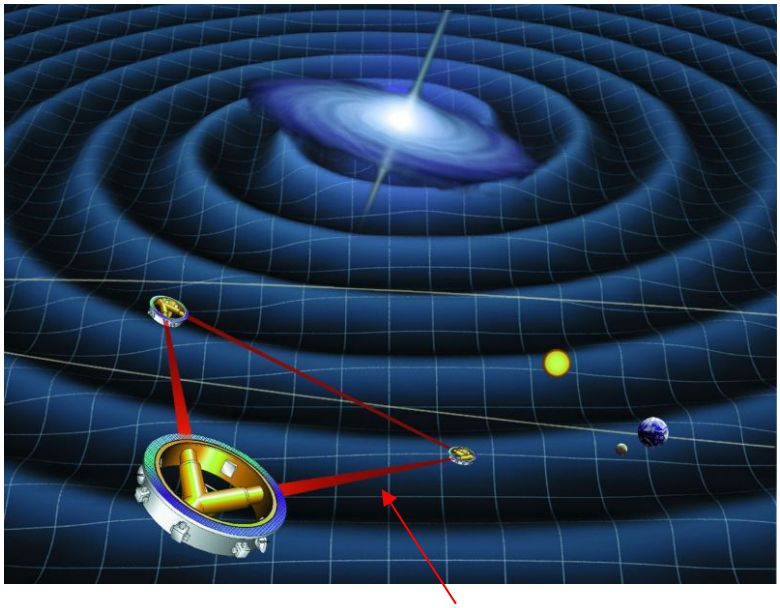

Figure 1.7. Artistic impression of the space based detector proposed as a joint ESA-NASA mission, having arm length of 5×10^9 m. Source - http://lisa.nasa.gov/

1.7 Noise sources

The sensitivity of the interferometric gravitational wave detector is affected by a number of noise sources. These include:

- Photon Shot Noise
- Thermal noise, in the test masses and their suspension systems.
- Seismic noise due to environmental vibrations.

1.7.1 Photon shot noise

Photon shot noise occurs due to the fluctuations in the number of photons at the output of an interferometer. According to Poisson statistics if N photons reach the output of the

interferometer then the uncertainty associated with counting the photons is $\sqrt{N}$. This leads to noise at the photodiode which in turn decreases the sensitivity of the detector. The shot noise limited sensitivity for a delay-line type interferometer is given by [29],

$$h_{shot}(f) \approx \left(\frac{h\lambda}{2\varepsilon I_o c} \right)^{\frac{1}{2}} \frac{f}{\sin(\pi\tau)} \frac{1}{\sqrt{\text{Hz}}}, \tag{1.7}$$

where h on the right hand side is Planck's constant, λ is the wavelength of light and ε is the photodetector quantum efficiency. I_o is the input laser power, c is the speed of light and τ is the storage time. It should be noted that increasing the laser power helps to improve the shot noise limited sensitivity; however it can also lead to an increase in the radiation pressure noise in the instrument. Radiation pressure noise results from the transfer of momentum to the test mass mirrors from photons reflecting off the surface of the test mass. In a simple Michelson type interferometer at a particular frequency the shot noise can be made equal to the radiation pressure noise, however this requires optimization of the input laser power.

1.7.2 Thermal noise

Thermal noise in the interferometer results from the thermal energy of atoms and molecules in the test masses and the suspension system. This will be discussed in detail in chapter 2.

1.7.3 Seismic noise

Seismic noise arises from natural phenomena such as ocean waves beating on the shore or from man made sources like movement of traffic. The level of seismic noise depends upon the location of a site and may vary with time. The pendulum suspensions used in

gravitational wave detectors have been specifically designed for seismic isolation over the range of frequencies in which the detectors operate. For the horizontal direction the pendulum attenuates the displacement by a factor of $\left(\frac{f_0}{f}\right)^2$ where f_0 is the resonant frequency and f is the frequency at which it is driven [12];[30].

1.7.4 Other noise sources

A full discussion on other noise sources can be found in the literature [31; 12; 32] and we do not include further discussion here.

1.8 Status of interferometric gravitational wave detectors

As remarked in section 1.5, there are several long baseline gravitational wave detectors based on laser interferometry in operation around the world. These are the LIGO detectors, the German-British GEO 600 detector, the French Italian Virgo detector and the Japanese TAMA detector. The work in this thesis has been directed towards the development of suspensions relevant to the planned upgrade of the LIGO detector system, Advanced LIGO.

1.8.1 LIGO and Advanced LIGO detectors

LIGO stands for *"Laser Interferometer Gravitational Wave Observatory"*. The LIGO project operates detectors located at two different sites in USA, one at Hanford (WA) and the other at Livingston (LA), shown in figure 1.8. The arm lengths of these detectors are 4 km with a second half-length detector in the same vacuum enclosure as the 4 km

instrument in the Hanford site. The test masses in the interferometer are constructed out of 10.7 kg silica mirrors and each one is suspended in a single wire loop wire suspension, shown in figure 1.9.

Hanford (Washington) *Livingston (Louisiana)*

Figure 1.8. Arial photographs of the two LIGO detector sites in the USA.

Figure 1.9. LIGO optic; fused silica mirror suspended from a single wire loop.

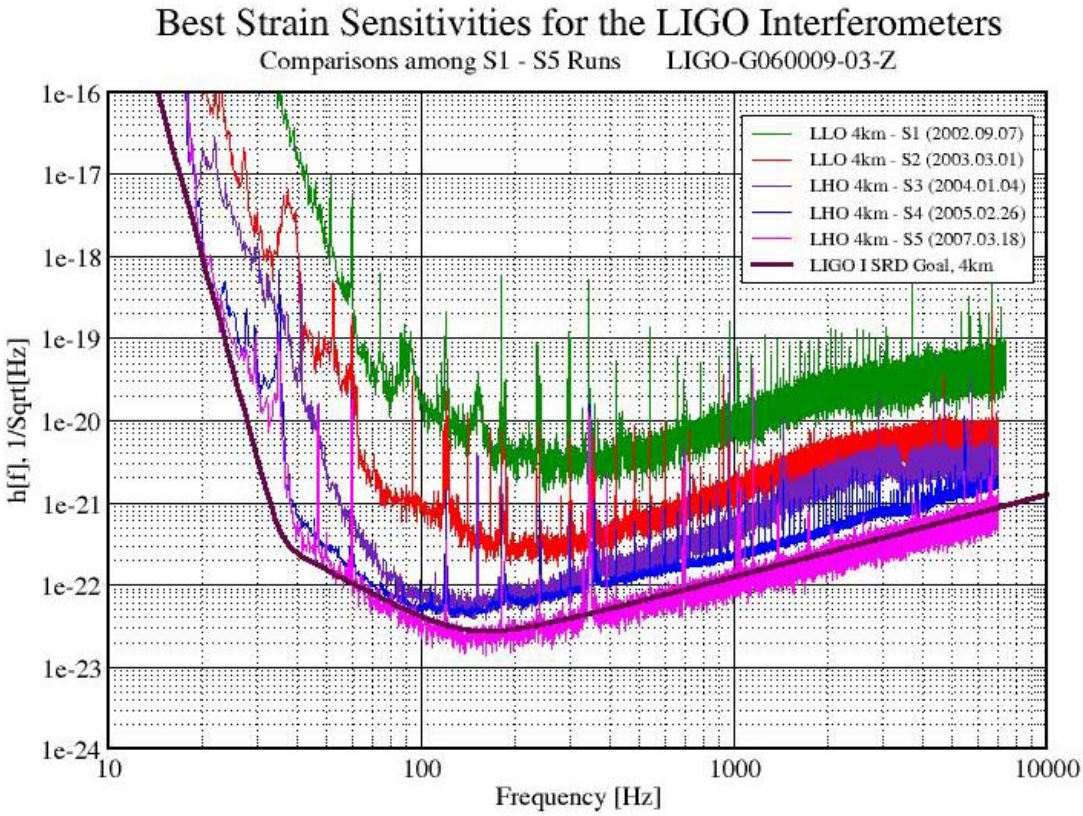

Figure 1.10. Strain sensitivity of the LIGO detectors for different science runs; the most recent data shown is from the fifth science run, S5, in 2007 [2].

Figure 1.10 shows the strain sensitivity (amplitude spectral density) of the LIGO detector for the different science runs made from 2002 till 2007. The best strain sensitivity ($h \sim 10^{-22}$ over a frequency range of 50 Hz to 1000 Hz, since the unit of power spectral density is per Hz, the unit of strain sensitivity is per square root Hz.) was achieved in the year 2007 from the fifth science run.

An upgrade to LIGO is the Advanced LIGO detector which is under development. The Advanced LIGO detector will employ 40 kg silica test masses, suspended from a quadruple pendulum system. The details of the suspension system will be discussed in chapter 6. Figure 1.11 compares the sensitivity of the LIGO detector and the planned Advanced

LIGO detector. The proposed sensitivity for the Advanced LIGO is expected to exceed that of LIGO by a factor of ten.

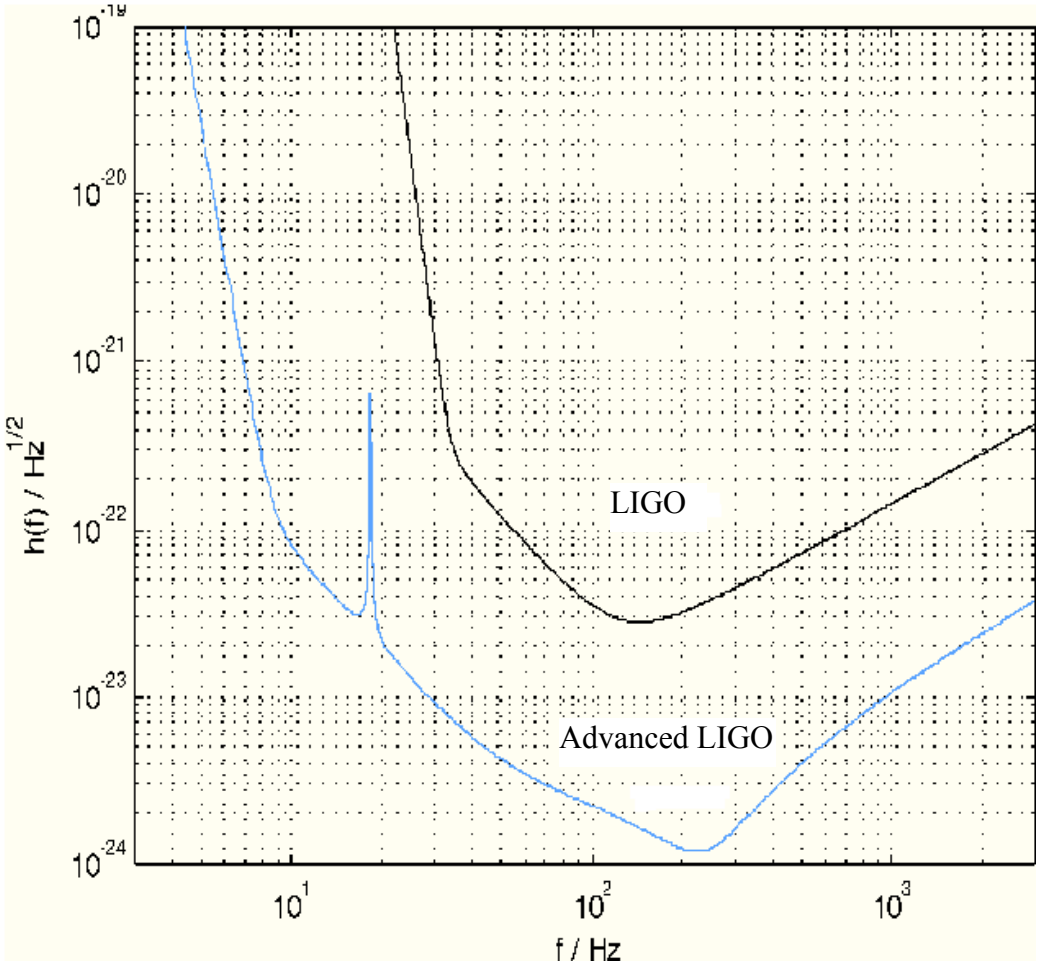

Figure 1.11. Comparison of sensitivity curves for the LIGO and advanced LIGO detectors [2].

1.8.2 GEO 600 detector

The German British GEO 600 detector is an interferometric gravitational wave detector near Ruthe outside Hannover in Germany. The GEO 600 suspension system is unique as it comprises a fused silica triple pendulum system described in detail in [33; 34; 35]. The

overall design sensitivity of the detector in terms of amplitude is $2\times10^{-22}/\sqrt{\text{Hz}}$ at 50 Hz. In order to achieve this sensitivity, a significant degree of seismic isolation has to be provided to the test mass in the horizontal and vertical direction. This can be accomplished by using a double pendulum system suspended from cantilever springs [36]. The details of the suspension system of the GEO 600 detector can be found in the literature [37]. It should be noted that the suspension system for Advanced LIGO is being developed from the GEO 600 detector's design.

(a) **(b)**

Figure 1.12. (a): GEO 600 site at Ruthe near Hannover, the central building for laser and vacuum tank can be seen, (b): the vacuum tubes, 600 m in length,

Figure 1.12 shows the site of the GEO 600 detector at Ruthe near Hannover in Germany, having an arm length of 600 m.

1.8.3 VIRGO detector

VIRGO is a French/Italian detector situated at Cascina, near Pisa. The VIRGO detector has arms of 3 km length. The mirrors are suspended from a multistage pendulum system. The details of the suspension system can be found in the literature [38].

1.8.4 TAMA detector

TAMA is a detector based in Tokyo, Japan, with an arm length of 300 m. The details of this detector can be found in the literature [39].

1.9 Conclusions

Significant progress has been made in recent years regarding the development of gravitational wave detectors. With improving sensitivities of detectors around the world, the direct detection of gravitational waves is becoming closer. Once this is achieved, it will open significant new avenues for observing the Universe via its gravitational signals.

Chapter 2

Thermal noise

2.1 Introduction

Thermal noise is one of the most significant of the noise sources for gravitational wave detectors. Thermal noise in the system reveals itself in two ways:

- Through the random motions of the atoms and molecules (Brownian motion) [40; 41].

- Through temperature fluctuations of different parts of the system. These temperature fluctuations can result in random displacement in the system if the materials have a finite temperature co-efficient of expansion or if the system is under stress and the relevant modulus of elasticity is a function of temperature (Thermo-elastic loss).

In a long baseline gravitational wave detector thermal noise is important in the suspension elements of the test mass mirrors (wires, fibres or ribbons) where it causes random movement of the mirrors at the pendulum modes and also movement at the violin mode frequencies of the suspension elements. It also leads to fluctuation in the position of the

mirror face of the test masses due to random fluctuations of the molecules in the test masses and their dielectric mirror coatings.

This thesis is devoted to studies relevant to thermal noise associated with the suspension elements in gravitational wave detectors.

2.2 Fluctuation-Dissipation theorem

The fluctuation-dissipation theorem states that in thermal equilibrium any linear system (i.e. one having a response proportional to the applied force) undergoing dissipation does have fluctuations of measurable parameters [42]. The power spectral density of the thermal driving force $S_F(\omega)$ is related to the dissipative (real) part of the mechanical impedance $Z(\omega)$ by the equation

$$S_F(\omega) = 4k_B T \Re[Z(\omega)]. \tag{2.1}$$

The suspension designs in gravitational wave detectors are based on models in which the resonant modes of test masses and suspensions are modelled as damped harmonic oscillators [43]. Hence in terms of power spectral density of displacement, $S_x(\omega)$, the fluctuation-dissipation theorem can be expressed as [44]

$$S_x(\omega) = \frac{k_B T \omega_0 \phi(\omega)}{2\pi^3 \omega m[(\omega_0^2 - \omega^2)^2 + \omega_0^4 \phi^2(\omega)]}. \tag{2.2}$$

where $\phi(\omega)$ is the mechanical dissipation or loss factor of the oscillator of mass m at temperature T, ω_0 is the angular resonant frequency and k_B is Boltzmann constant (1.3806×10^{-23} Jk^{-1}). Thus the materials used for the test masses and suspensions in

interferometric gravitational wave detectors are of low loss factors and high quality factor Q, where $Q = \frac{1}{\phi(\omega_0)}$.

2.3 Sources of dissipation

In the mirror suspension of an interferometer there are many sources of dissipation which need to be minimized in order to achieve low levels of thermal noise. These dissipations can be broadly categorised as internal and external sources.

2.3.1 External sources of dissipation

The external sources of dissipation are as follows,

- Frictional: at the point of suspension, where wires are clamped or are joined to the test mass.
- Gas Damping or viscous damping: collision with residual gas molecules in the suspension system.
- Recoil damping: energy loss from the motion of the pendulum suspension to the support structure due to recoil.
- Magnetic hysteresis and eddy current damping

2.3.2 Internal sources of dissipation

Once the external sources of dissipation are minimized, the internal source of loss becomes dominant due to friction within the material. This can arise when a material behaves

inanelastically. The internal dissipations are broadly categorized into two types, i.e. viscous and structural dissipation.

2.4 Thermoelastic dissipation

Thermoelastic loss describes heat flow across thin flexing beams or fibres and was studied by Zener [45] and Norwick [46]. In order to understand this phenomenon, consider a thin wire that is deflected, due to which one side would be in a state of compression and the other in tension. This will lead to a rise in temperature on the side which is under compression while the other side under tension will cool. This in turn will lead to heat flow across the wire until thermal equilibrium is reached. The heat flow results in a loss which is frequency dependent and is related to the relaxation time to reach the equilibrium position.

In an un-deflected wire the local temperature fluctuation will cause motion of the wire. This is due to expansion or contraction resulting from the finite thermal expansion coefficient of the wire material. The expansion coefficient α can be expressed as

$$\alpha = \frac{1}{l}\frac{dl}{dT}. \tag{2.3}$$

Where l is the original length of the wire and dl/dT is the change in length with respect to temperature. The dimensions of the body, its thermal conductivity and specific heat capacity are related to the characteristic frequency for the heat transfer. The characteristic frequency of a wire of circular cross section and diameter d, is given by [47; 46]

$$f_{char} = \frac{1}{2\pi\tau} = 2.16\frac{\kappa}{\rho C d^2} Hz. \tag{2.4}$$

Here κ is the thermal conductivity, C is the specific heat capacity and ρ is the density of the wire material.

For a wire of rectangular cross section, the characteristic frequency can be represented as

$$f_{char} = \frac{\pi\kappa}{2\rho C t^2}. \tag{2.5}$$

The loss associated with the thermoelastic dissipation is given by

$$\phi(\omega) = \Delta \frac{\omega\tau}{1+(\omega\tau)^2}, \tag{2.6}$$

where

$$\Delta = \frac{Y\alpha^2 T}{\rho C}. \tag{2.7}$$

This assumes that the Young's modulus, Y, is approximately temperature independent but this cannot be said for all materials. Hence a parameter, β, called the elastic thermal coefficient which is analogous to the thermal expansion coefficient, can be introduced

$$\beta = \frac{1}{Y}\frac{dY}{dT}. \tag{2.8}$$

This elastic thermal coefficient will not lead to any contribution to thermal noise unless there is a static stress, σ, in the beam. To understand what happens in a situation where there is a static stress the case of a simple pendulum is considered.

For a pendulum of length L the coefficient of thermal expansion is given by,

$$\alpha = \frac{1}{L}\frac{dL}{dT}, \tag{2.9}$$

or for a temperature change *dT*,

$$dL = \alpha L(dT). \tag{2.10}$$

However there is an equivalent *dL* (change in length) which results from the change in Young's modulus with temperature when the pendulum suspension fibre is under tension as will be shown below.

We have

$$\sigma = Y\left(\frac{dL}{L}\right), \tag{2.11}$$

or

$$dL = \left(\frac{\sigma L}{Y}\right). \tag{2.12}$$

Hence we can write

$$\frac{dL}{dT} = \frac{-\sigma L}{Y^2}\frac{dY}{dT}, \tag{2.13}$$

or

$$\frac{1}{L}\frac{dL}{dT} = \frac{-\sigma}{Y^2}\frac{dY}{dT}. \tag{2.14}$$

Thus for a temperature change *dT,* due to the temperature coefficient of Young's modulus

$$dL = \frac{-\sigma L}{Y^2}\frac{dY}{dT}dT. \tag{2.15}$$

Thus in total for a temperature change *dT*,

$$dL_{total} = \alpha L dT - \frac{\sigma L}{Y^2}\frac{dY}{dT}dT. \tag{2.16}$$

Thus there is an effective 'coefficient of expansion' $\alpha' = \frac{1}{L}\frac{dL_{total}}{dT} = \left(\alpha - \frac{\sigma}{Y^2}\frac{dY}{dT}\right)$ and when thermoelastic noise is calculated this effective 'coefficient of expansion' should be used. Hence when considering the loss factor of suspension materials the thermoelastic loss has to be added to the intrinsic material loss, where the thermoelastic loss is given by,

$$\phi(\omega) = \Delta\frac{\omega\tau}{1+(\omega\tau)^2}, \tag{2.17}$$

where

$$\Delta = \frac{YT}{\rho C}\left[\alpha - \left(\frac{\sigma}{Y^2}\frac{dY}{dT}\right)\right]^2, \tag{2.18}$$

and will be discussed further in chapter 7.

2.5 Dissipation dilution factor

The reason for choosing pendulum suspensions was to provide seismic isolation to the test mass mirror (as discussed in Section 1.7.3). Apart from this, it can also help in minimising thermal noise. This is because it can store most of the energy in the non dissipative gravitational field. In order to understand this effect, let's consider an example of a simple pendulum suspending a mass *m* with the help of a single wire. Once the mass is suspended the wire will be under tension equivalent to *'mg'* and will elongate until the elastic restoring force matches the weight of the mass. Upon vertical excitation, the system will undergo simple harmonic motion and the frequency of its oscillation is set by the spring constant of the wire.

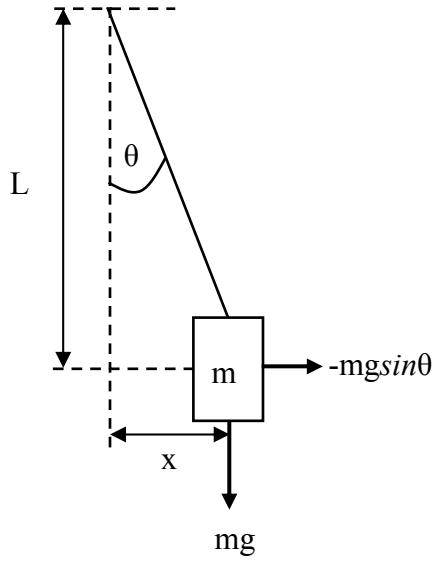

Figure 2.1. A simple pendulum system displaced horizontally, with gravity as a restoring force.

On displacing the pendulum horizontally, as shown in figure 2.1, a restoring force will be developed due to the effect of gravity on the mass and also from the spring constant of the wire. The restoring force for the gravitational field gives the equivalent spring constant of

$$k_{grav} = \frac{mg}{L}. \tag{2.19}$$

This equation can be used to estimate the effect of the loss for such a pendulum system. The energy stored in the bending of the wire is given by

$$E_{stored_{wire}} = \frac{1}{2} k_{wire} x^2, \tag{2.20}$$

where k_{wire} is the spring constant of the wire. If some fraction (χ) of energy is lost per cycle then it can be represented as

$$E_{lostpercyde} = \frac{1}{2} \chi k_{wire} x^2. \tag{2.21}$$

By using a description of loss

$$\phi(\omega_0) = \frac{1}{Q} = \frac{E_{lostpercyde}}{2\pi E_{stored}}, \tag{2.22}$$

The loss of the material can be calculated as follows

$$\phi_{mat}(\omega_0) = \frac{\frac{1}{2} \chi k_{wire} x^2}{2\pi \frac{1}{2} k_{wire} x^2} = \frac{\chi}{2\pi}. \tag{2.23}$$

Adding in the energy stored in the gravitational field,

$$E_{stored_{pendulum}} = \frac{1}{2}(k_{wire} + k_{grav})x^2. \tag{2.24}$$

Hence

$$\begin{aligned}\phi_{pendulum}(\omega_0) &= \frac{\frac{1}{2}\chi k_{wire}x^2}{2\pi\frac{1}{2}(k_{wire}+k_{grav})x^2} \\ &= \frac{\chi k_{wire}}{2\pi(k_{wire}+k_{grav})}.\end{aligned} \tag{2.25}$$

On dividing this by the loss of the material (i.e. equation 2.25 by equation 2.23),

$$\frac{\phi_{pendulum}(\omega_0)}{\phi_{mat}(\omega_0)} = \frac{k_{wire}}{k_{wire}+k_{grav}}. \tag{2.26}$$

If $k_{grav} >> k_{wire}$ then,

$$\phi_{pendulum}(\omega_0) \approx \phi_{mat}(\omega_0)\frac{k_{wire}}{k_{grav}}. \tag{2.27}$$

Hence, since $k_{grav} >> k_{wire,}$ the loss in the pendulum is reduced by the factor known as the 'dilution factor'.

If there are *n* wires suspending the mass (wires attached in a plane through the centre of mass perpendicular to the direction of swing) instead of just one wire, then the elastic spring constant is given by [44],

$$k_{wires} = \frac{n\sqrt{TYI}}{2L^2}, \tag{2.28}$$

where *T* is the tension in each wire, *Y* is the young's modulus of the wire material, *I* is the area moment of inertia. *'I'* for circular cross section wire is given by $I = \frac{\pi r^4}{4}$ [48] and for a wire of rectangular cross section it is, $I = \frac{ba^3}{12}$ [49], where *a* is the thickness of the wire and *b* is the width. Hence the total pendulum loss is given by

$$\phi_{pendulum}(\omega_0) \approx \phi_{mat}(\omega_0)\frac{n\sqrt{TYI}}{2mgL}. \tag{2.29}$$

Since dilution factor $\frac{1}{D} = \frac{\phi_{pendulum}}{\phi_{material}}$ and using '*mg=nT'* gives the dilution factor formula,

$$\frac{1}{D} = \frac{\sqrt{YI}}{2L\sqrt{T}}. \tag{2.30}$$

2.6 Interferometer suspension thermal noise sources

In a low loss oscillator most of the thermal noise comes from its resonant modes. The resonant modes are discussed next.

2.6.1 Pendulum mode thermal noise

The pendulum mode thermal noise is due to the mechanical loss of the suspension material which suspends the test mass. The loss in the pendulum is related to the loss of the suspension material such that in general [44],

$$\phi_{pend}(\omega_0) \approx \phi_{mat}(\omega_0)\frac{\xi n\sqrt{TYI}}{2mgL}. \tag{2.31}$$

ξ is either 1 or 2, depending on whether the wires are bending at the top, or at both the top and the bottom [50].

The pendulum mode frequency should be below the detection band of the instrument and this can be done by keeping the wires long and thin. The loss in the pendulum can be minimized via the effect of the dilution factor as the energy is stored in the gravitational field and in the bending of wires. The thermal noise from the suspension system then depends on the loss factor (Brownian motion and thermoelastic dissipation) and the dilution factor.

This has motivated designs such as those used in the GEO 600 detector and proposed as the baseline design for the Advanced LIGO detector. The suspension elements of the Advanced LIGO detectors have been studied in this thesis.

The GEO 600 suspension is a monolithic fused silica triple pendulum system. The final stage of the suspension system is shown in figure 2.2. Fused silica fibres of diameter 0.3 mm (300 microns) and length 280 mm have been chosen as the suspension elements for the final stage pendulum system, to lower the mechanical loss factor. The dimensions of these fibres were chosen to keep the bounce mode frequency to be as low as possible (around 15 Hz) and the first violin mode (as discussed in 2.6.2) to be as high as possible.

This will help in keeping the thermal noise peaks associated with these mode frequencies out of the detection band of the GEO 600 detector. The fibres are attached to silica ears which have themselves been attached to 5.6 kg test mass mirrors. The silica fibres suspending each test mass of the GEO 600 suspension system and subsequent systems are expanded at their ends for welding and thus are tapered.

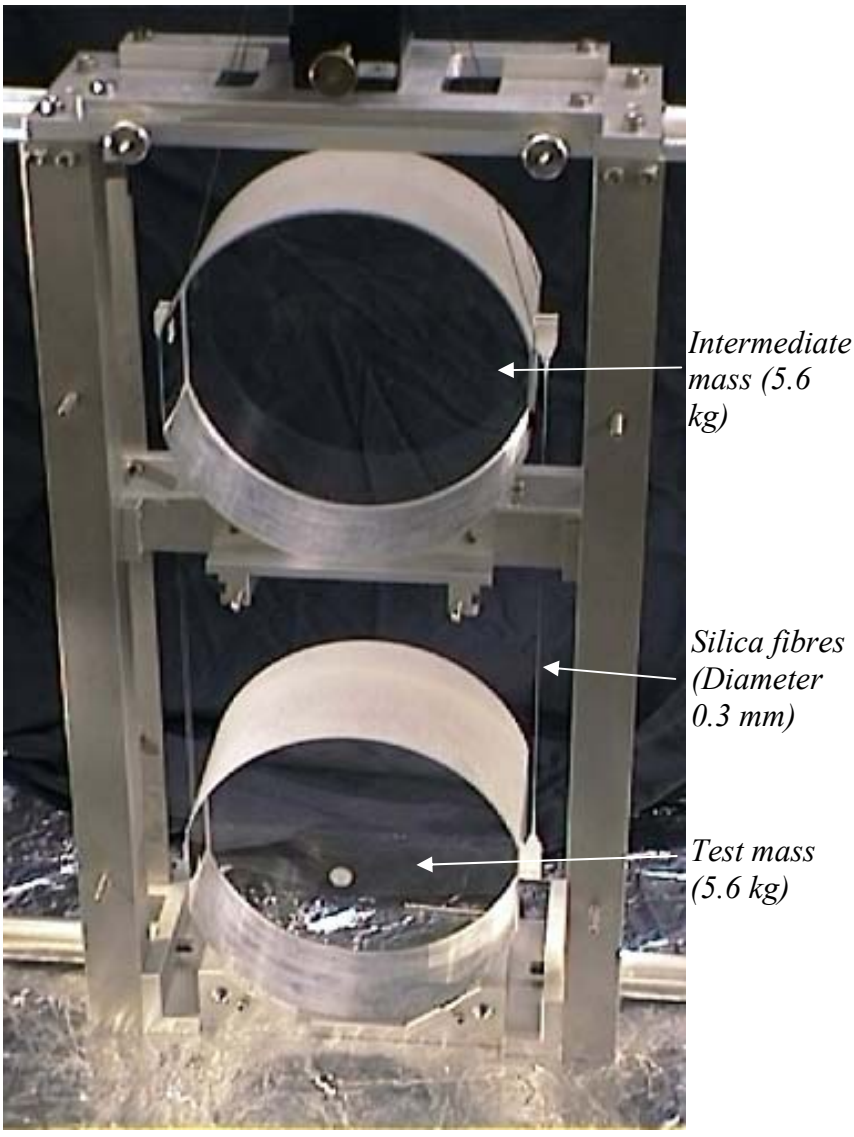

Figure 2.2. Final stage of the monolithic fused silica pendulum of the GEO 600 suspension system. The intermediate mass is suspended by two steel wires in loops and the test mass is suspended by four silica fibres with the help of two ears attached to each side of the test mass.

The Advanced LIGO detector will have quadruple pendulum suspension systems and the suspension design is based on the GEO 600 suspension system. Figure 2.3 shows a CAD drawing (Solidworks) of the monolithic final stage of the suspension system. It consists of a 40 kg penultimate mass suspended by steel wires in loops. The test mass also weighs 40 kg and is suspended by four silica fibres of length 600 mm and diameter 0.4 mm (400 microns) or ribbons of the same length and cross sectional area 1.1 mm thick by 0.11 wide. The fibres or ribbons of these dimensions were chosen to keep the bounce mode frequency below 10 Hz. and the first violin mode frequency above 400 Hz.

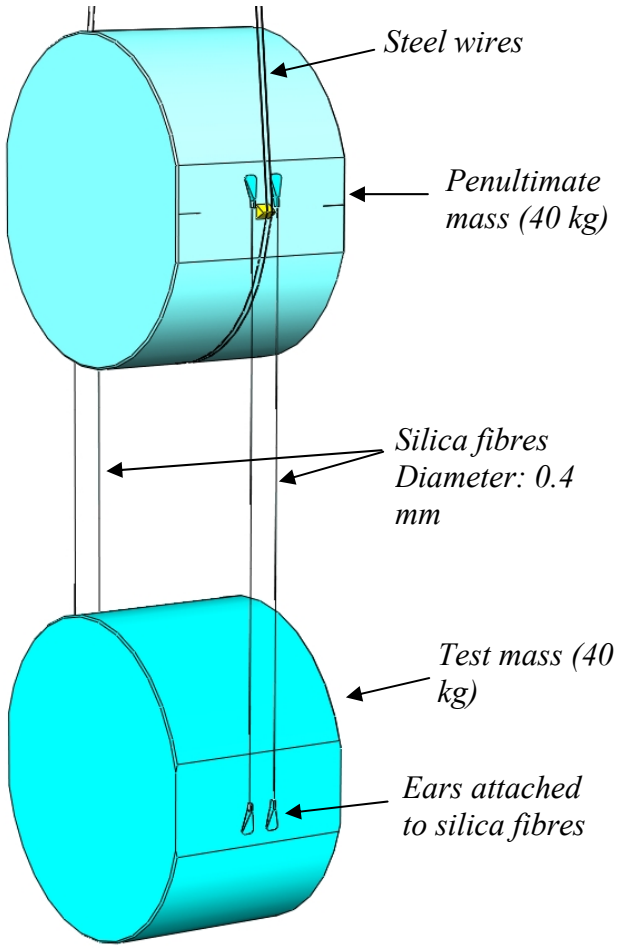

Figure 2.3. CAD® model showing the final stage of the Advanced LIGO suspension system.

The baseline design of the Advanced LIGO suspension system has silica ribbons of uniform cross section area for suspending the test mass, since it has been estimated that silica ribbons of uniform cross section area should have higher dilution factor as compared to silica fibres. This should result in lower pendulum loss and hence reduce the thermal noise in the suspension system. However the ribbons or fibres will always have tapered ends for welding to the test masses and in this situation the consequences of including tapered necks in the suspension elements needs to be further studied. This is a major area of study of this thesis.

The planned suspension elements of the Advanced LIGO detector were studied with the intention of estimating and possibly lowering their predicted thermal noise. For this the energy distribution and the dilution factor estimation of the pendulum system was required. A high dilution factor would result in lower loss in the pendulum which will help in the reduction of the thermal noise. However, for the Advanced LIGO suspension system, apart from the dilution factor, the thermoelastic loss is also an important aspect for determining the thermal noise in the pendulum. Hence a study of thermoelastic loss in the suspension elements of the Advanced LIGO detector has also been carried out towards the end of this thesis.

2.6.2 Violin mode thermal noise

The violin modes, also known as the transverse vibrational modes, of the suspension fibres form a harmonic series and lie within the detection band. The first violin mode will have a loss that is twice the loss associated with the pendulum mode [50; 51]:

$$\phi_{violin}(\omega) = 2\phi_{pendulum}(\omega). \tag{2.32}$$

As the suspension system is made up of low loss material, the thermal noise will be concentrated within a range of narrow frequencies around the resonance, allowing it to be removed easily from the detector noise spectrum.

2.7 Conclusions

Thermal noise is one of the most important areas limiting the sensitivity of the detectors and there are important issues with the designs of the suspension elements that require further study. This will help us to understand and optimise the designs of suspension elements.

Evaluation of the expected thermal noise from the suspension systems can be improved by the use of the finite element techniques to carefully study the behaviour and distribution of energy in the systems. Such a study is carried out in this thesis.

Chapter 3

Introduction to finite element analysis (FEA)

3.1 Introduction

The Finite Element method of structural analysis was created by researchers in the 1950s. However the underlying theory is considerably older.

Finite Element Analysis (FEA) is a way to simulate loading conditions on a system and determine the response of the system to those conditions. The system under study is modelled using discrete building blocks called elements. These elements have equations which describe their response to a certain load. The sum of the response of all the elements in the structure gives the total response of the system.

There are substantial benefits from using FEA in the study of mechanical structures. It can reduce the amount of prototype testing required, as computer models can simulate multiple potential situations, which can be tested quickly and efficiently. This helps in the reduction of cost as well as time. ANSYS® version 11.0 of ANSYS, Inc. USA is one such F. E analysis package which is used for these simulations and the work in this thesis is based on extensive usage of ANSYS®.

3.2 Creating the finite element model

Designing a structure in ANSYS® consists of four major steps which are shown in the chart below,

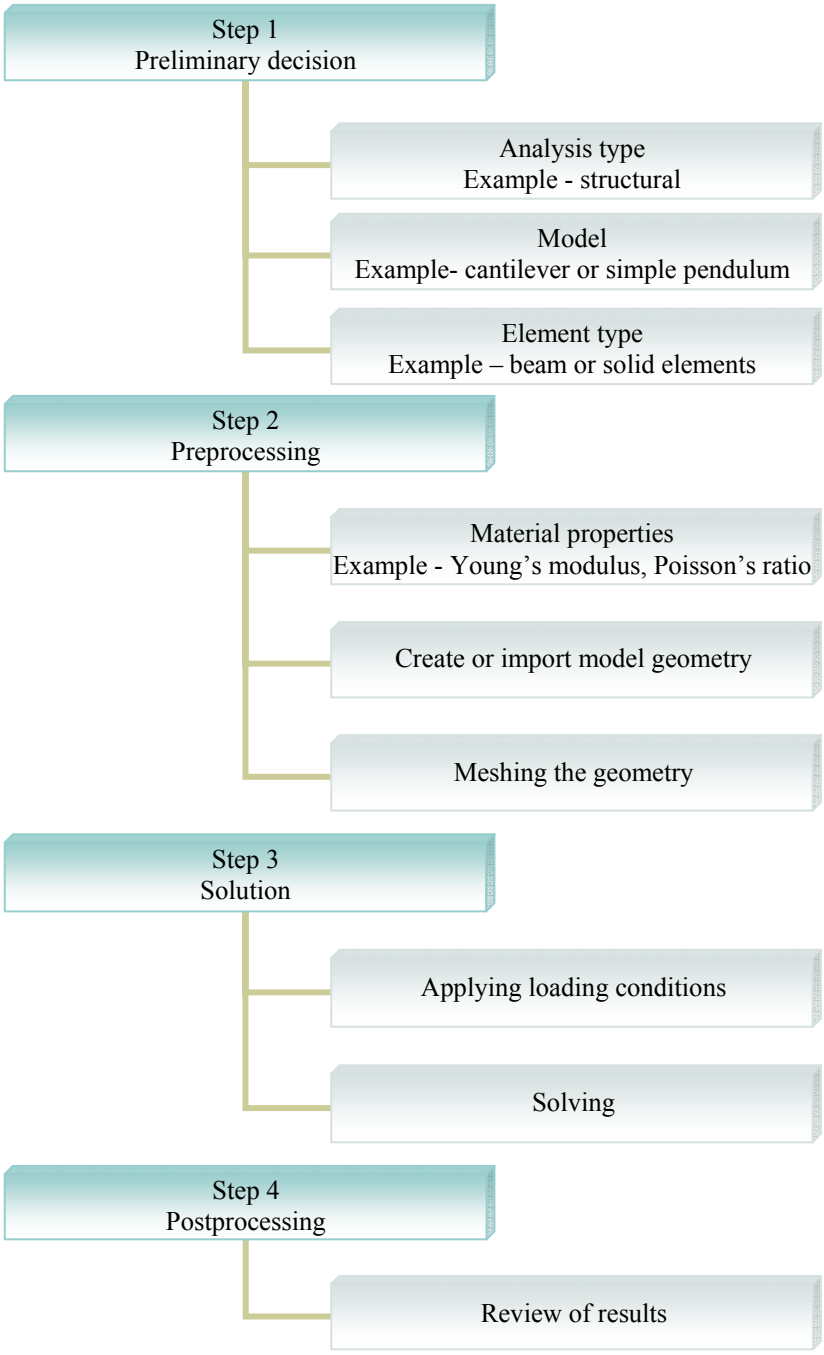

Figure 3.1. Basic steps involved in designing a model in ANSYS®.

3.3 Modelling of a simple structure in ANSYS®

The aim is to design and simulate a real structure in ANSYS® using the four steps shown in figure 3.1. The first step is '*preliminary decisions*' which involves choosing an analysis type, selecting a model and its element types. Suppose the model to be designed in ANSYS® is a thin cylindrical wire, such as one used in a mirror suspension in a gravitational wave detector. Then the appropriate analysis type for this model is a *structural analysis* since it deals with motion, pressure and contact of solid bodies. ANSYS® has a library of 170 'element types' to choose from. The 'element type' which best fits our given (cylindrical wire) model is a *beam element.* 'Beam189' (a specific type of beam element available in ANSYS®) is one such element and is suitable for analysing any long, slender to moderately stubby/thick beam structures. Each element has a number of nodes assigned to it, with six degrees of freedom at each node. These include three translational and three rotational in the x, y, and z directions. Beam189 also includes shear deformation and stress stiffening effects. This is to take into account the effect of buckling and bifurcation behaviour in all geometrically nonlinear analyses.

The next is the 'preprocessing' stage where the material properties are defined. In our example the material was taken as silica having a density of 2202 kg/m^3; Young's modulus 7.2×10^{10} Pascal and Poisson's ratio (ratio of lateral strain and axial strain) as 0.17. The actual model is then designed using keypoints (points used to designate co-ordinates). As an example consider a fibre of length 600 mm and diameter 0.4 mm. The first step is to build two keypoints which define the total length of the wire. These keypoints are then joined by a line. The 'Element attributes' are then defined, including the 'element types', 'material properties' and the dimension of the model. This is then 'meshed' (by issuing

mesh command), i.e. subdivided into a small number of sections whose behaviour can be computed.

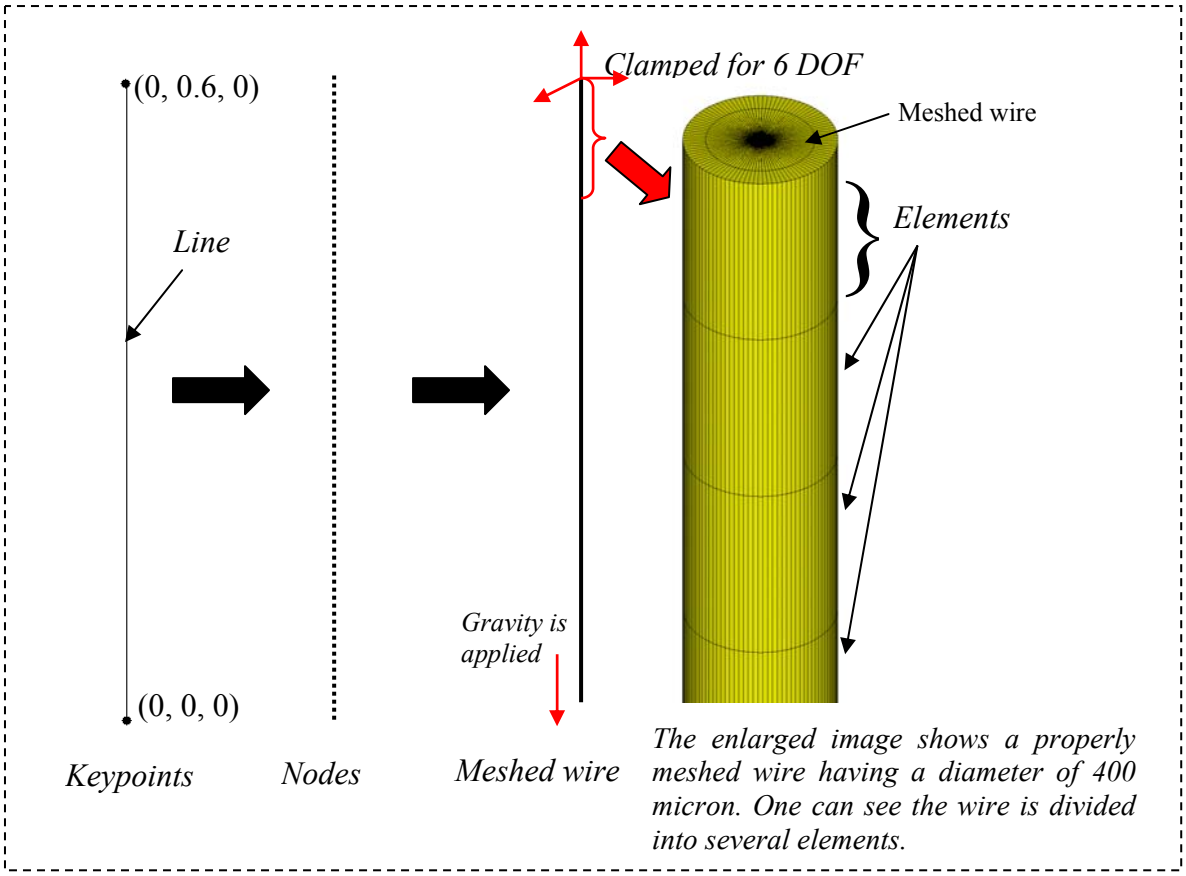

Figure 3.2. Schematic of the process of building up of a wire model in ANSYS®.

After successfully designing the model one moves on to the solution part of ANSYS®. This requires defining the loads applied to the model and applying the relevant constraints. For example the body is subjected to inertial loads due to structural mass or inertia, such as gravity. In our example, one end of the wire is constrained in all six degrees of freedom and the other end is left free. A force of 10^{-4} Newton (chosen to obtain a small displacement) in the horizontal direction is applied to the bottom of the wire. This is then subjected to *structural static analysis*. A static analysis calculates the effects of steady loading conditions on a structure, while ignoring inertia and damping effects, such as those

caused by time varying loads. It can, however include steady inertia loads such as gravity. This analysis can be used to determine the displacements, stresses, strains and forces in structures or components that do not induce significant inertia and damping effects.

The postprocessing helps in reviewing the results of the solved design. The results give the mode shapes and amplitude (although not for all the cases, for obtaining the amplitude of complex structures further analysis is required) of the deformed model due to the applied force. The value of displacement in our simple case can be verified by the beam bending formula given by [52].

$$\Delta = \frac{WL^3}{3YI}, \tag{3.1}$$

where, Δ is the displacement, W is the load (force), L is the Length of wire, Y is the Young's modulus, I is the area moment of inertia.

Displacement, (ANSYS®) (mm)	Displacement, (Theory) (mm)
79.57	79.577

Table 3.1. Comparison of results obtained through ANSYS® modelling and analytically for the bending of a thin beam.

Table 3.1 shows the comparison of displacement values obtained from ANSYS® and estimated analytically using equation 3.1 and the results agree well, showing that the model was designed well and works fine. The structure is then further solved using *Modal Analysis*. Modal analysis is used for determining the natural frequency and mode shapes of the structure. It can also be used to determine the stress and strain energy in the structure.

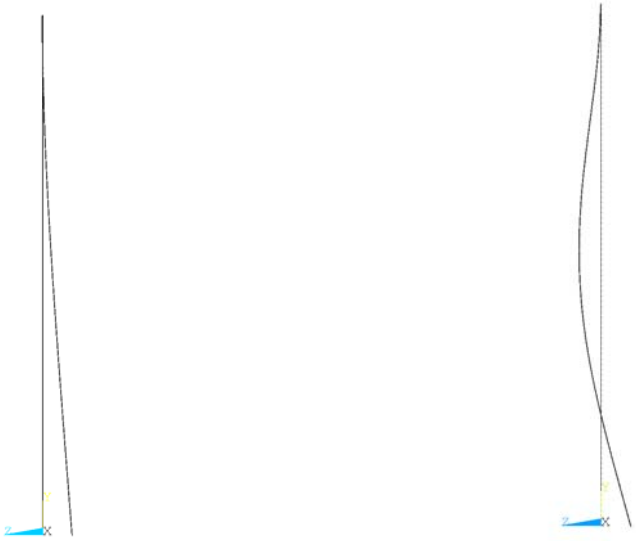

First bending mode
Frequency- 1.20 Hz

Second bending mode
Frequency- 5.86 Hz

Figure 3.3. Mode shape and frequency obtained from ANSYS® for bending of a thin wire, the shown modes are first and second bending modes.

Figure 3.3 shows the first bending mode and the second bending mode for a thin wire under the influence of a horizontal force. The two modes shapes and their respective frequencies shown above are obtained from ANSYS® modelling.

3.4 Convergence of frequencies

In order to successfully design a model in ANSYS® one needs to determine the number of elements to be used in building up the structure. Models with dense meshes and huge numbers (thousands) of elements are best for reliable results, although this consumes substantial computational time. Hence an optimum number of elements needs to be estimated in-order to get the desired results in limited time. Convergence of frequencies

can be achieved through a trial and error method where one needs to start designing the model with small numbers of elements and gradually increase this number till convergence is achieved.

As an example figure 3.4 shows the plot of 'frequency vs. number of elements' for the first and second bending mode of a wire (dimensions same as described in section 3.3). The number of elements for this structure was varied from two to twenty and was meshed accordingly. The model was then solved in ANSYS® to get the desired resonant frequency. Looking at the graph, the frequencies converge after having four (as a factor of safety) elements in the structure.

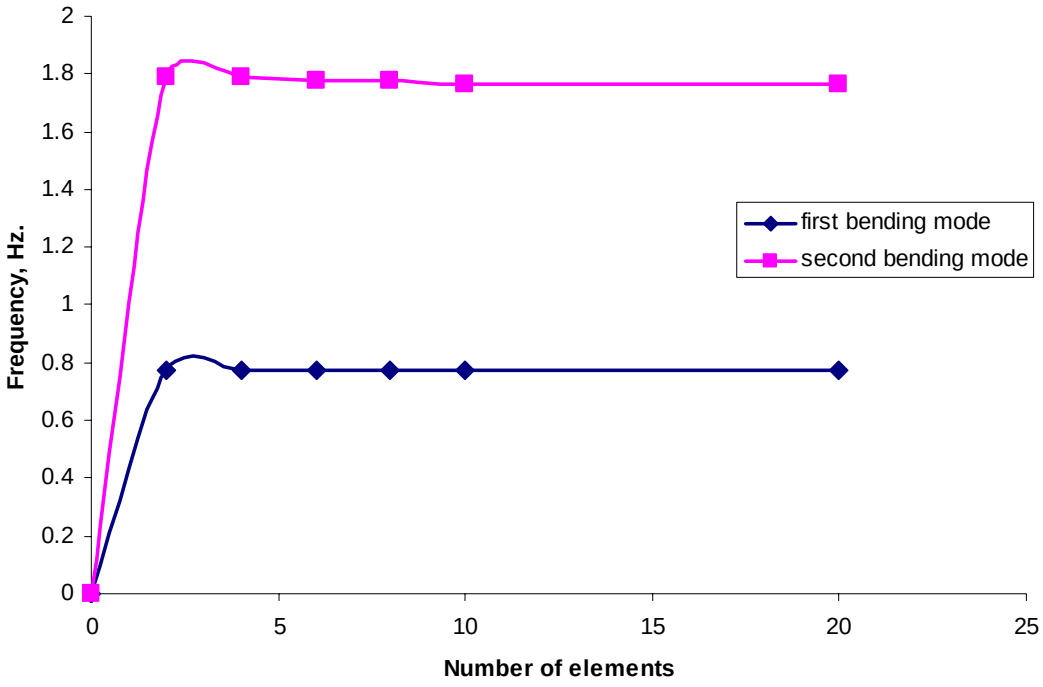

Figure 3.4. Convergence of 'frequencies for a wire modelled in ANSYS®.

3.5 Conclusions

The finite element method was adopted for a simple structure in this chapter to demonstrate the working of ANSYS®. This introduction gives the required confidence to move ahead and design more complex structures. Extensive usage of finite element analysis has been carried out in the chapters ahead to analyse the response of different structures with respect to their loading conditions.

Chapter 4

Designing a single wire fused silica pendulum suspension system in ANSYS®

4.1 Introduction

One of the most important techniques required for the estimation of 'dissipation dilution' and 'energy distribution' for the Advanced LIGO detector's pendulum system is discussed in this chapter using a simple model of a single wire pendulum system, designed in ANSYS®.

The performance of silica fibres and silica ribbons as suspension elements is compared, initially for the case of uniform cross sectional area where dissipation dilution can be estimated analytically and using F. E techniques and later on for the case of elements with linear tapered necks as required for welding fibres or ribbons to attachments on the test masses. In the latter case and in realistic cases with necks of more arbitrary shape simple analytical techniques may not be sufficient and F. E methods of estimating dissipation dilution are extremely useful.

4.2 Modelling a single wire pendulum system in ANSYS®

Before creating an F. E model of a pendulum like that planned for use in the Advanced LIGO system, having four silica suspension fibres fused to a mass (40 kg), it is useful to start with the study of a very simple design of a single wire suspending a proportionally (10 kg) lighter mass, to illustrate and examine some aspects of pendulum behaviour.

A simple pendulum model was designed in ANSYS® and is shown in Figure 4.1. The mass is suspended by a thin fused silica fibre. The length of this fibre was taken as 600 mm and its diameter as 0.4 mm (400 micron) which is the specification for the Advanced LIGO suspension system. The relevant material properties input to ANSYS® are: density (silica) - 2202 kg/m^3, Young's modulus (silica) - 7.2×10^{10} Pascal and Poisson's ratio (silica) - 0.17 [53]. The cylindrical mass is 150 mm thick and 60 mm in diameter. The dimensions and the density of the mass were chosen such that it weighed 10 kg. The number of elements used in the ANSYS® model was chosen on the basis of convergence of frequencies, similar to the one discussed in the previous chapter (however a pendulum model was used this time).

In parallel a similar pendulum model was created by A. Cumming [1] using ribbons of rectangular cross section instead of fibres, such that the behaviour of the two types of pendulum could be compared. The length of this comparative ribbon is 600 mm, with thickness 0.11 mm and width 1.1 mm. Measurement errors on these dimensions are expected to be less than approximately 10%.

The cross sectional area of the ribbon and the fibre taken here are approximately the same and differ by just 3%.

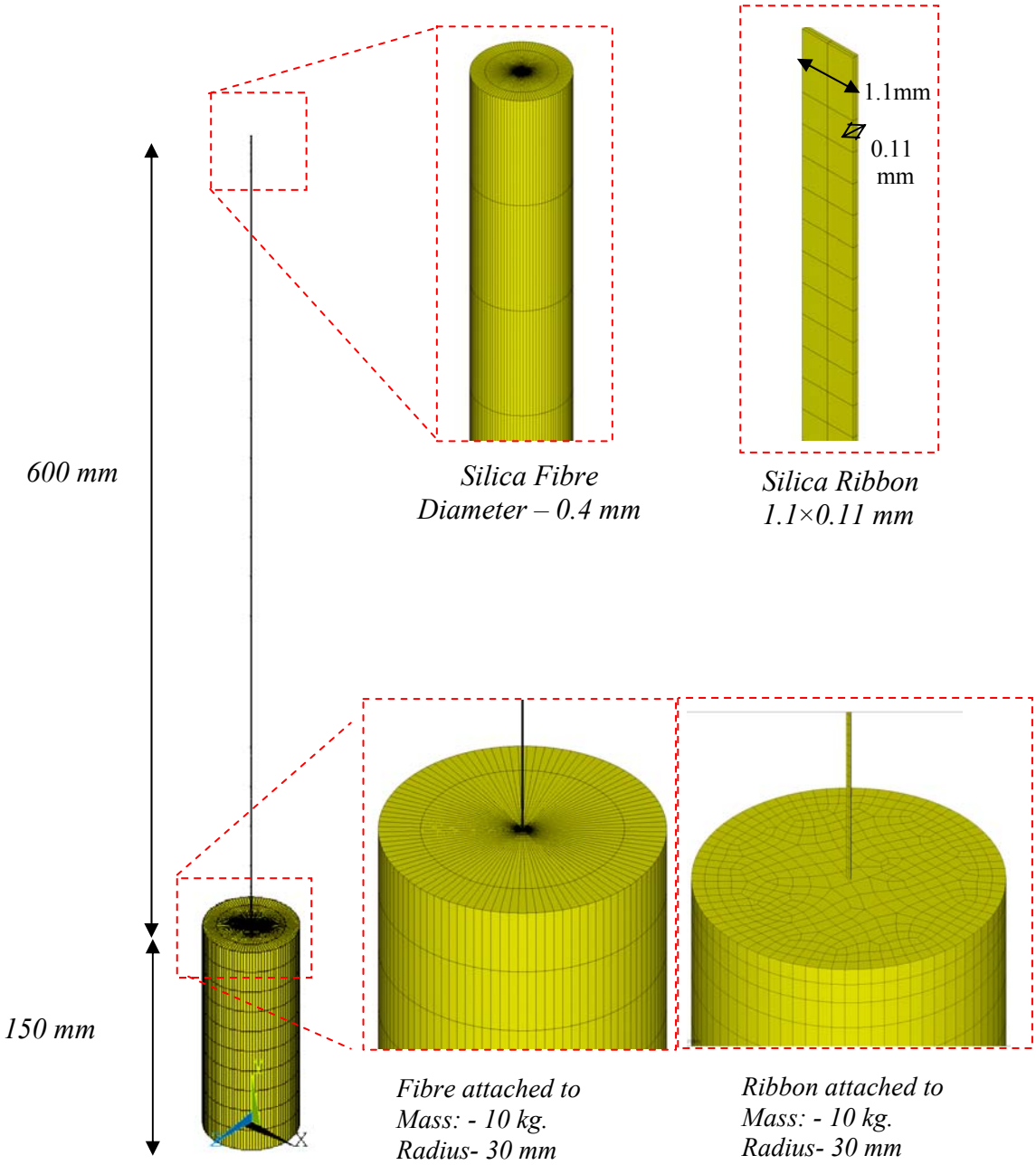

Figure 4.1. A simple pendulum with a cylindrical fibre suspending a mass of 10 kg designed in ANSYS®. Also shown is a pendulum with a ribbon (modelled by A. Cumming [1]) suspension element for comparison. Note: The meshing in the mass looks different as a different meshing style has been adopted while constructing the model, however this does not affect the performance of this particular model.

The designed and finely meshed ANSYS® models were clamped for all six degrees of freedom at the top end of the fibre. The structure was then subjected to loading condition (like gravity) before solving it in ANSYS® to obtain resonant mode frequencies.

Table 4.1 gives a comparison of mode frequency obtained from ANSYS® and verified from theory (assuming the same dimensions and conditions as described previously). Theoretically the frequencies were estimated from MATLAB^R code written by C. Torrie [34].

Mode shape (ANSYS)	**Frequency, Hz. (ANSYS)**	**Frequency, Hz. (MATLAB)**
Rotational mode	0.027	0.027
Pendulum mode	0.606	0.606
Pitch(tilt) mode	3.190	3.167
Bounce mode	6.213	6.829
First Violin mode	497.76	497.79

Table 4.1. Frequencies of oscillation for the first few resonant modes of a pendulum consisting of a single fibre suspending a mass of 10 Kg using ANSYS® and its comparison with analytical values.

The mode frequencies were identified by looking at the deformed mode shape and mode animation in ANSYS®. Shown in figure 4.2, are the mode shapes obtained after solving the system using modal analysis. The first mode is the *rotational mode* where the mass is gyrating. The second mode is the *pendulum mode,* were the mass is displaced along the horizontal axis by a small distance and undergoes simple harmonic motion. The *Pitch mode* follows next, where the mass appears to tilt due to the motion of the pendulum. This is followed by the bounce mode where the pendulum performs a vertical oscillation motion. At higher frequencies the first and second *violin modes* were seen, where the suspension fibre vibrates. This is similar to the vibration of a guitar string.

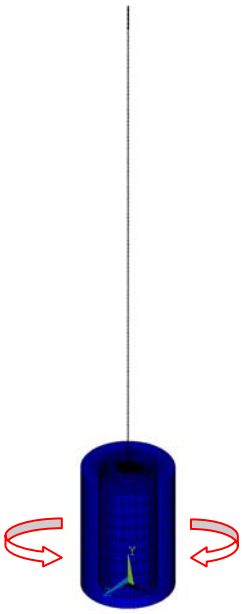

Mode -1
Rotational mode
Frequency: - 0.0271 Hz.

Mode - 2
Pendulum mode
Frequency: - 0.606 Hz.

Mode - 3
Pitch mode
Frequency: - 3.190 Hz.

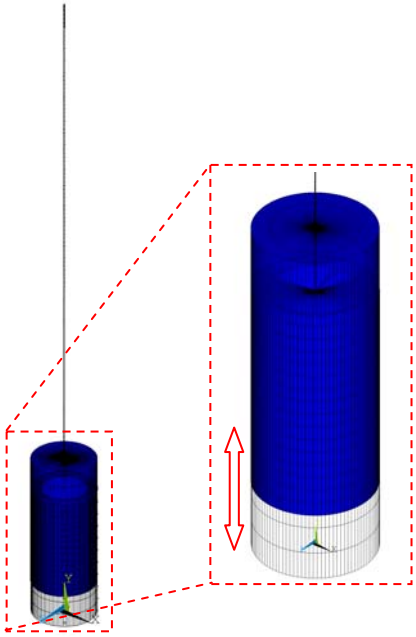

Mode - 4
Bounce mode
Frequency: - 6.213 Hz.

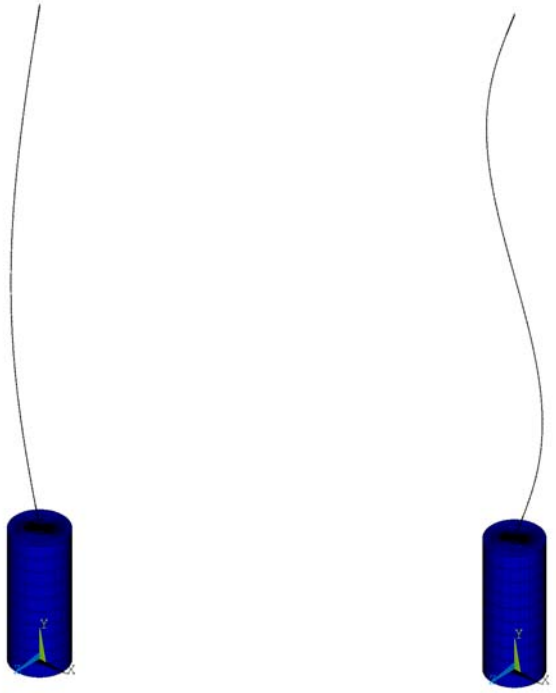

Mode - 5
First Violin mode
Frequency: - 497.76 Hz.

Mode - 6
Second Violin mode
Frequency: - 995.56 Hz.

Figure 4.2. Mode shapes obtained from ANSYS® for a single fibre suspending a mass of 10 kg.

4.3 Analysis of the pendulum mode of vibration

In order to minimize the seismic noise and the thermal noise in the gravitational wave detector, the test masses are suspended as pendulums. When a pendulum oscillates most of the restoring force comes from the effects of gravity on the pendulum mass while only a small amount of restoring force is due to the bending of the wire that supports the suspended mass against gravity. The gravitational potential energy is lossless and the only source of loss comes from the mechanical energy stored in the wire due to bending. It can be shown that the relationship between the loss in the pendulum and the loss in the wire is given by [44]

$$\phi_p = \phi_w \frac{E_{el}}{E_{grav} + E_{el}} \approx \phi_w \frac{E_{el}}{E_{grav}}, \tag{4.1}$$

where ϕ_p is the loss in the pendulum, E_{el} and E_{grav} are the energy stored in the flexing of the wire and in the gravitational field respectively. Thus the mechanical loss of the pendulum can be much lower than the mechanical loss of the material from which its suspension fibres are made. This dilution effect was discussed in chapter 2.

4.3.1 Bending length of a wire

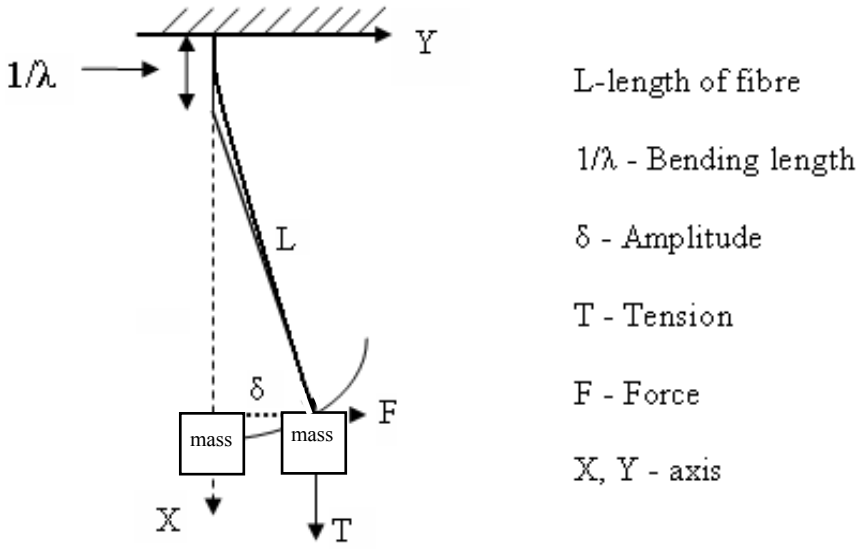

Figure 4.3. A wire under tension is deformed by force F. The pendulum swings with an effective length smaller than the real length L by the amount 1/λ

In a single wire pendulum system where the wire is attached to the top surface of the mass, i.e. well above its centre of gravity, the bending due to the oscillation of the pendulum occurs predominantly at the top section of the wire. Figure 4.3 shows the bending of the

fibre under tension *T*, where *1/λ* is the bending length. When a force is applied, the pendulum is deformed and undergoes a small displacement. The bending length can be visualised by drawing a tangent from the line of the deformed shape. This tangent intersects the un-deformed fibre (the point of this intersection is called flexure point) and from the flexure point to the top-most section of the fibre is the effective bending length. The bending length *1/λ* of the wire can be shown from [54] to satisfy

$$\frac{1}{\lambda} = \sqrt{\frac{YI}{T}}, \tag{4.2}$$

where *T* is Tension in the fibre, *Y* is the Young's modulus of the fibre, *'I'* is the area moment of inertia, ($\pi \times d^4/64$) and *d* is the diameter of the fibre. The bending length can only easily be calculated analytically for a uniform cross section wire. However in all cases including wires of non uniform cross section such as those used in fused silica suspensions in gravitational wave detectors, it can be estimated using a finite element method

For the single wire pendulum model discussed in section 4.3, the flexure point of the fibre and ribbon were estimated from ANSYS® and calculated using equation 4.2. The value obtained using ANSYS® agrees accurately as shown in table 4.2.

Wire used in the pendulum	**Bending length ANSYS®, (mm)**	**Bending length (Theory), (mm)**
Silica fibre	0.960	0.9608
Silica ribbon	0.462	0.461

Table 4.2. Comparison of bending length value calculated from ANSYS® and analytically.

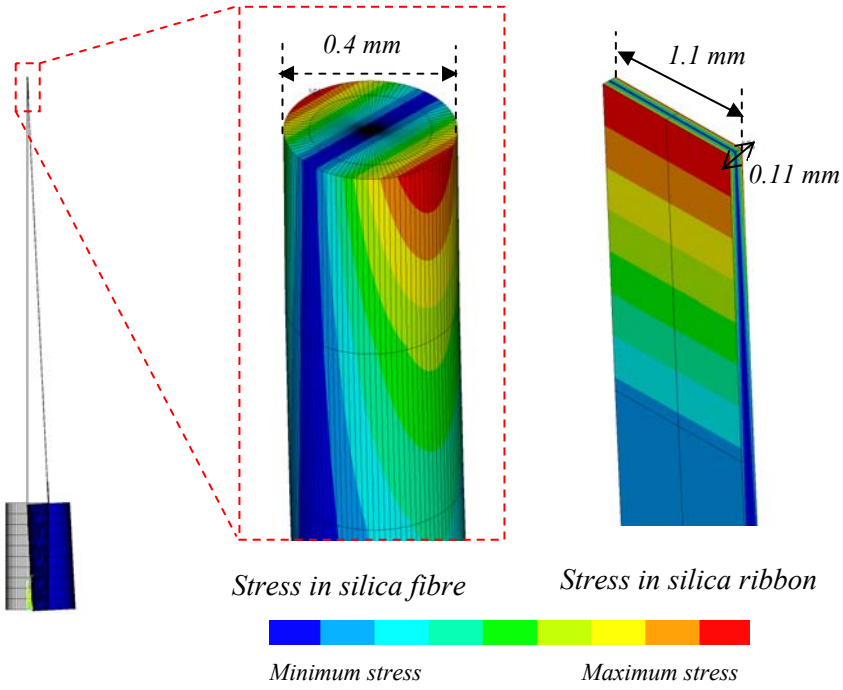

Figure- 4.4. Contour lines plotted in ANSYS® showing the stress distribution in a fibre and ribbon respectively due to their bending close to the top of each suspension element, for the pendulum mode of vibration.

The bending of a fibre due to the swinging of a pendulum results in the development of stress within the fibre. This is shown in the form of contour lines in figure 4.4 for the fibre and ribbon suspension parameters discussed in section 4.2. The figure shows the stress distribution in the fibre compared to the ribbon for a constant displacement of the mass. The location of the maximum stress in the body can be identified by the contour lines plotted in red whereas minimum stress is shown in blue. Most of the stress can be seen to occur at the top of the fibre or ribbon, as most of the bending occurs there. Once the bending length of the fibre has been estimated and a stress plot obtained, the next step is to study the distribution of energy and subsequently to calculate of the dissipation dilution factor of the pendulum system (discussed next).

4.3.2 Dilution calculation in ANSYS® (for pendulum mode)

The theory for the dissipation dilution factor has been previously discussed in chapter 2. The mechanical loss of a pendulum results mostly from flexing at the ends of its fibre where maximum bending occurs. In other words, the loss is concentrated at the bending points of the fibres. The loss of the pendulum is directly proportional to the loss of the material used for its suspension fibres but reduced by the *Dilution factor* (equation 2.30). The dilution factor can be defined as the ratio of the total gravitational energy of the suspension pendulum motion to its elastic energy as discussed in the literature [44; 54].

The elastic energy is the energy stored in bending the fibre when the pendulum reaches its maximum displacement. ANSYS® identifies this as the "strain energy" stored in the fibre of the pendulum. As a pendulum swings, the gravitational potential energy of the mass at the extreme of the swing is converted into kinetic energy, as the pendulum passes through its equilibrium position. This can also be directly obtained from an ANSYS® model. Thus the ratio of the 'total kinetic energy' stored in the system to the 'strain energy' stored in the fibre (or at the ends of the fibre) gives the dilution factor.

Figure 4.5 shows a simple pendulum undergoing simple harmonic motion. The strain energy in the fibre can be found by studying the system at the point where it undergoes maximum displacement. ANSYS® allows the option of finding the strain energy in each element of the fibre. Similarly the total kinetic energy can be obtained by studying the system at the point where it returns to its equilibrium position during oscillation.

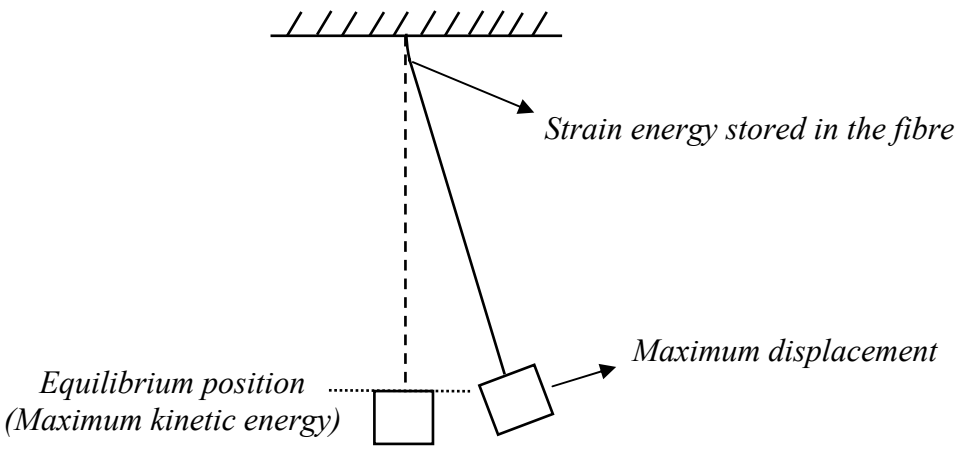

Figure 4.5. A simple pendulum model used to study the effect of displacement on the stored energy in the pendulum.

As discussed in chapter 2, (eqn. 2.30) dilution $\frac{1}{D}$, can be analytically calculated from the following equation [44],

$$\frac{1}{D} = \frac{\xi n\sqrt{TYI}}{2mgL}. \tag{4.3}$$

Here ξ takes the value 1 or 2: (1- if bending of the suspension elements occurs only at the top of each elements), n is number of wires (fibres or ribbons in this case), T is the tension in each wire, Y is the Young's modulus of the fibre or ribbon material, *'I'* is the area moment of inertia, given for fibres and ribbons respectively by [52],

$$I_{fibre} = \frac{\pi d^4}{64}, \tag{4.4}$$

$$I_{ribbon} = \frac{ba^3}{12}, \tag{4.5}$$

where *'d'* the diameter of the fibre, *'m'* is the suspended mass, *'g'* is acceleration due to gravity, *'L'* is the total length of the wire, *'b'* is the width of the ribbon and *'a'* the thickness of the ribbon.

4.3.3 Strain energy distribution in the fibre of the pendulum (ANSYS® model)

The strain energy values can be plotted as a function of length of the wire. The suspended mass is expected to contain a negligible amount of energy. The graph shown in figure 4.6 shows the distribution of strain energy in the fibre. The fibre starts to bend right from the point where it is clamped and hence maximum strain energy is concentrated at this end. As one examines the magnitude of the strain energy at points along the length of the fibre, it can be seen that the energy decreases significantly. ANSYS® suggests that almost 90 % of the total energy is stored within the first 3.5 mm (approximately) of the fibre from the clamped end and thereafter has a negligible value. The bottom section bends very little and the bending energy is almost six hundred times lower than within the top section of the fibre.

A similar study of the distribution of the strain energy in a pendulum suspended by a ribbon was carried out by A. Cumming [1] for comparison with the fibre case and is shown in figure 4.7. The plot shows that most of the strain energy in the ribbon is contained within the starting 1 mm length and is negligible thereafter.

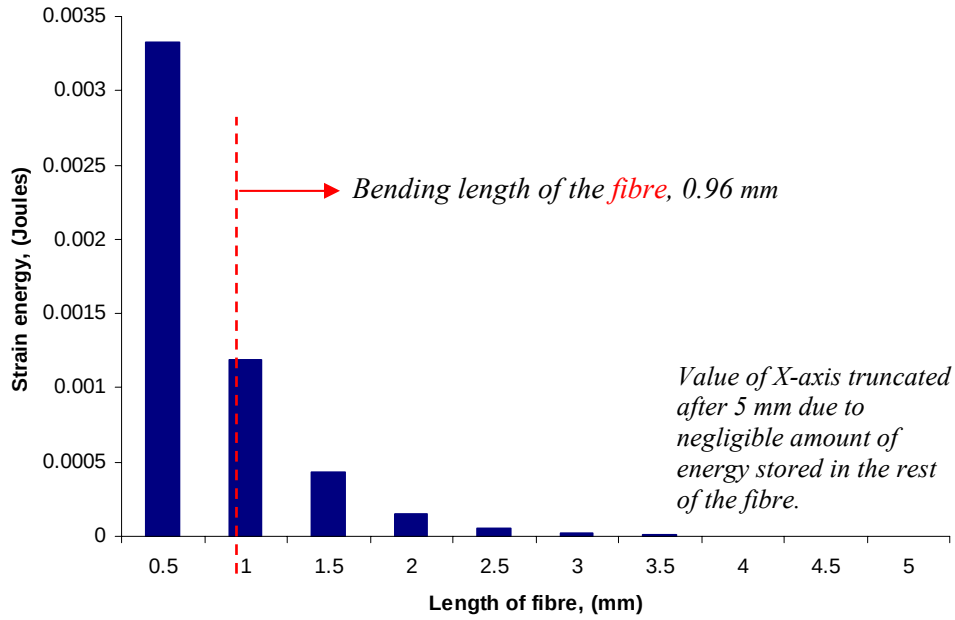

Figure 4.6. Energy distribution in the fibre as a function of its length, for the longitudinal pendulum mode of a single fibre suspending a mass of 10 kg. The length of the fibre plotted in the x-axis of the graph has been truncated after 5 mm as negligible energy is seen after the first 3.5 mm of the fibre.

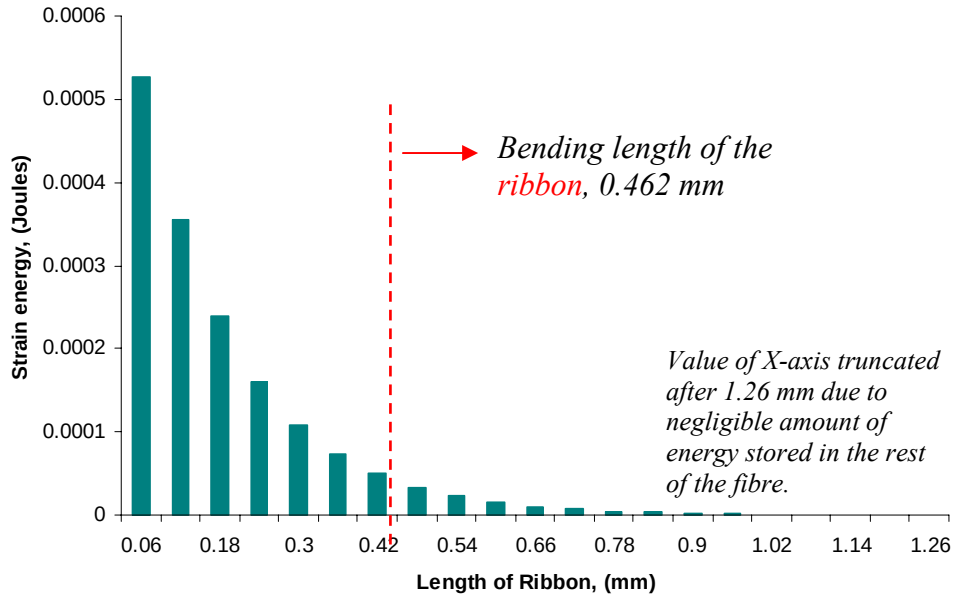

Figure 4.7. Energy distribution in the ribbon as a function of its length, for longitudinal pendulum mode of 'single ribbon suspending a mass of 10 kg'. The length of the ribbon plotted in the x-axis of the graph has been truncated after 1.26 mm as negligible energy is seen after the first 1.02 mm of the fibre.

4.3.4 Comparison of dilution factor for pendulum suspended by a single fibre or ribbon

Using the analytical formula given in equation 4.3, the dilution factor was calculated for the pendulum suspended by a uniform fibre and ribbon respectively.

It can be seen from equation 4.3 that dilution factor is inversely proportional to the square root of the area moment of inertia of the flexing suspension element. The area moment of inertia of the ribbon (1.22×10^{-16} m^4, estimated from equation 4.5) is smaller than that of the fibre (1.256×10^{-15} m^4, estimated from equation 4.4), because the ribbons are thinner than the fibres in the direction of flexing. Hence in this case the pendulum suspended by a ribbon should have a higher dilution factor then a pendulum suspended by a fibre, under equal tension. The ratio of maximum kinetic energy and the strain energy in the fibre, as explained before, allowed the appropriate dilution factor to be obtained from ANSYS®.

The results obtained from ANSYS® and from the analytical formula agree to within 1%, for both fibre and ribbon suspension elements, as seen from table 4.3. The numbers confirm our expectation that ribbons may have an advantage over the fibres for suspension elements because of their higher dilution factor which results in lower loss in the pendulum.

Dilution factor- Fibre (ANSYS)	**Dilution factor – Fibre (Theory)**	**Dilution factor - Ribbon (ANSYS)**	**Dilution factor - Ribbon (Theory)**
1396	1405	4478	4511

Table 4.3. Dilution factor calculated from ANSYS® and compared to theory, for a single fibre and ribbon, suspending a mass of 10 kg.

4.3.5 Summary

The single fibre or ribbon of uniform cross section, suspending a mass of 10 kg is the first step towards building more complex models. The results show that the single wire model works well in ANSYS® and gives us the confidence to move further and design a more realistic model of suspension of the type which will be used in the advanced gravitational wave detectors.

The next section comprises discussion of the inclusion of linearly tapered necks at the ends of a fibre or ribbon while applying the same loading conditions, to study the response of the whole structure. The neck design was then studied for a range of lengths such that the length of the tapered section could be optimised.

4.4 Introduction of linear tapered necks in silica fibre and ribbon of the pendulum system

The *silica fibres* or ribbons fabricated in the laboratory are not uniform in terms of their cross sectional area. Instead they include tapered necks at their ends. The taper design is inherent in the production method used to create silica fibres and ribbons where they are pulled from thicker stock material into fibres and ribbons of chosen dimensions (the fabrication method is discussed in chapter 6). The tapered necks of the fibre or ribbons are also essential for the purpose of welding (like fibres welded to mass via ears). It is of considerable importance to understand and quantify the effects of a tapered cross-section at the ends of the suspension elements on the distribution of strain energy in the suspension elements and hence on the achievable dilution and thus mechanical loss leading to thermal noise of any pendulum using such a suspension fibre or ribbon.

4.4.1 Analysis of 7.5 mm long linearly tapered necks in the fibre or ribbon of the pendulum system

To analyse the design of the tapered silica fibre an ANSYS® model was built and the necks were studied for two different taper lengths. The design of the neck region was kept linear in nature to keep the models simple (although the real necks tend to be curved). At first the length of the neck region was assumed to be 7.5 mm which was then increased to 15 mm. This is because the length of the typical necks fabricated in laboratory varied between these two dimensions. Figure 4.8 represents a 7.5 mm long linear taper neck in the fibre and ribbon.

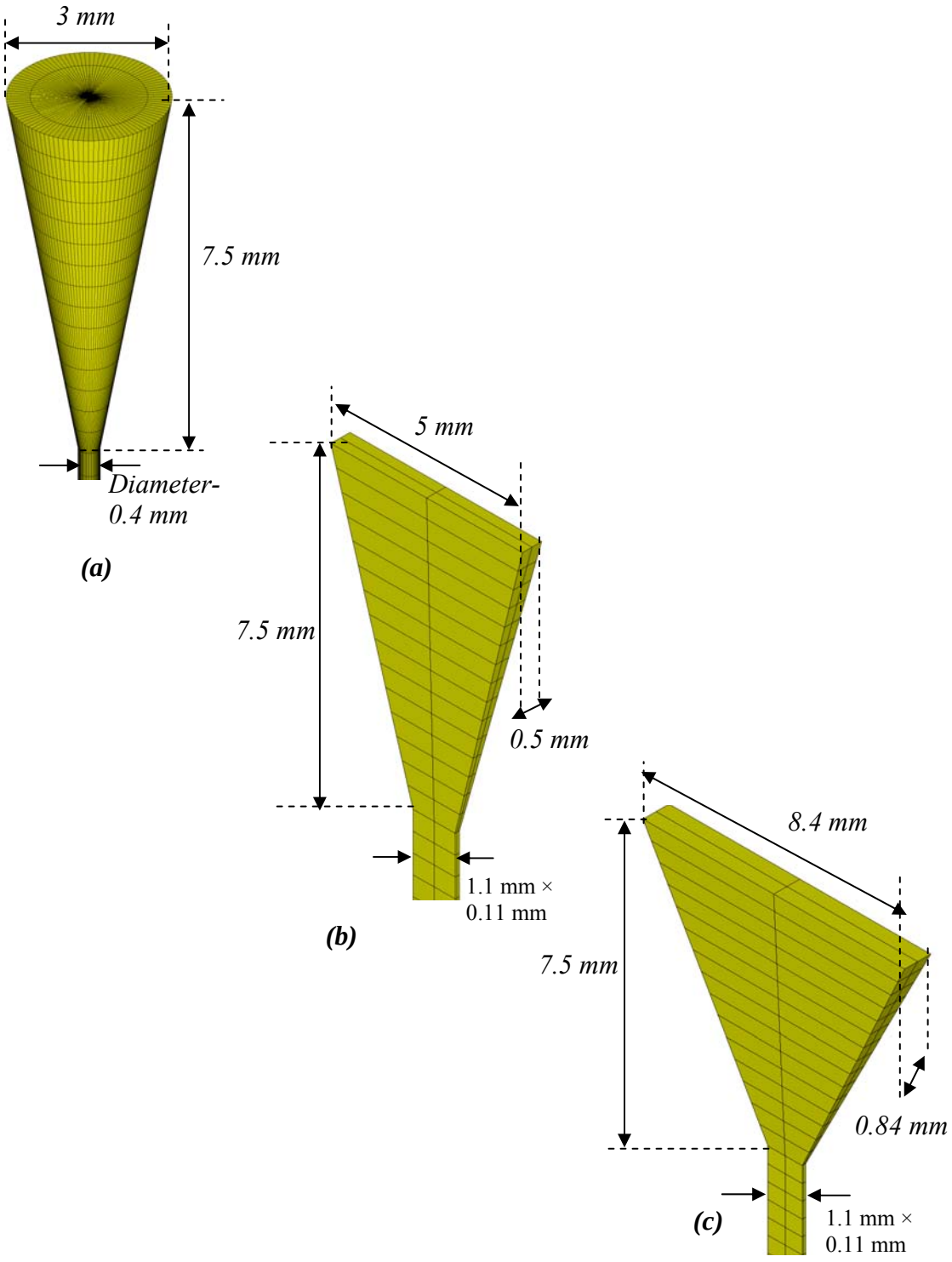

Figure 4.8. ANSYS® model of linear tapered necks of fibres and ribbons used for suspending a mass of 10 kg. (a): 7.5 mm taper (fibre), (b) 7.5×5×0.5 mm tapered (ribbon, (c) 7.5×8.4×0.84 mm tapered ribbon.

The fibres shown in figure 4.8(a) have a starting cross sectional diameter of 3 mm. The second cross section in the fibre is the thinnest section having a diameter of 0.4 mm (400 micron). Similarly the other end of the fibre also consists of linearly tapered design. The dimension of the tapered fibre was based on a real fibre which is usually pulled from a 3 mm diameter cylindrical rod. The total length of the 'tapered fibre' here remains 600 mm and it is attached to the top surface of the 10 kg mass.

The ribbons studied by A. Cumming [1] for comparison are shown in figure 4.8(b), the first having dimensions 5 mm by 0.5 mm decreasing to 1.1 mm wide and 0.11 mm thick. The ribbons are typically fabricated from a silica slide which is 5 mm by 0.5 mm and hence the same starting dimensions were taken for the ANSYS® models. The ribbon shown in figure 4.8(c) (which is 8.4 mm wide by 0.84 mm thick and the second cross section area 1.1 mm wide by 0.11 mm thick) was designed to make its starting cross sectional area the same as that of fibre.

The pendulum model was then solved for static and modal analysis in ANSYS®. The frequency of vibration for the pendulum mode in each case is shown in table 4.4.

ANSYS® model	Fibre (diameter 0.4 mm) with 7.5 mm tapered neck	Ribbon with 7.5 mm tapered neck (5 mm width by 0.5 mm thick)	Ribbon with 7.5 mm tapered neck(8.4 mm width by 0.84 mm thick)
Frequency (Hz)	0.60572	0.60697	0.60788

Table 4.4. Longitudinal pendulum mode frequency for a single fibre or ribbon with a 7.5 mm tapered neck, suspending a mass of 10 kg.

The bending length of the tapered fibre/ribbon was calculated using a static analysis in ANSYS® (as described in section 4.3) and the results are shown in table 4.5.

ANSYS® model	Fibre (diameter 0.4 mm) with 7.5 mm tapered neck	Ribbon with 7.5 mm tapered neck (cross section-5×0.5 mm)	Ribbon with 7.5 mm tapered neck(cross section-8.4×0.84 mm)
Bending length (mm)	8.02	3.766	5.82

Table 4.5. Bending length of single "linear tapered (7.5 mm)" fibres and ribbons, suspending a mass of 10 Kg (estimated using ANSYS®).

It is interesting to note that the fibres are bending beyond the taper section. For the necks which are 7.5 mm long, the bending length of the fibre is 8.02 mm. This shows that both the tapered section and a portion of the uniform cross section area of the fibre are participating in the bending process. However this was not seen in the case of ribbons. The ribbons were seen to experience the bending in the taper section itself (i.e. at 3.766 mm from top). This was due to the fact that the tapered fibres are stiffer than tapered ribbons. The neck of the ribbons is thinner and hence bends more easily at the top, whereas the stiffer fibres are resisting bending at the thicker section. However when the stiffness of both fibres and ribbon are made equal (i.e. ribbon of cross section - 8.4×0.84 mm) then the bending length of the ribbon increases to 5.82 mm, although it still remains lower than the fibre.

Figures 4.9 and 4.10, give visual verification of the difference in the flexing behaviour of the fibres and ribbons studied, as can be seen by plotting the stress distribution in the tapered ends at the top each suspension elements. The contour lines show the stress developed in the necked region due to bending in that region. The red spot signifies the area of maximum stress and the blue areas indicate the minimum stress.

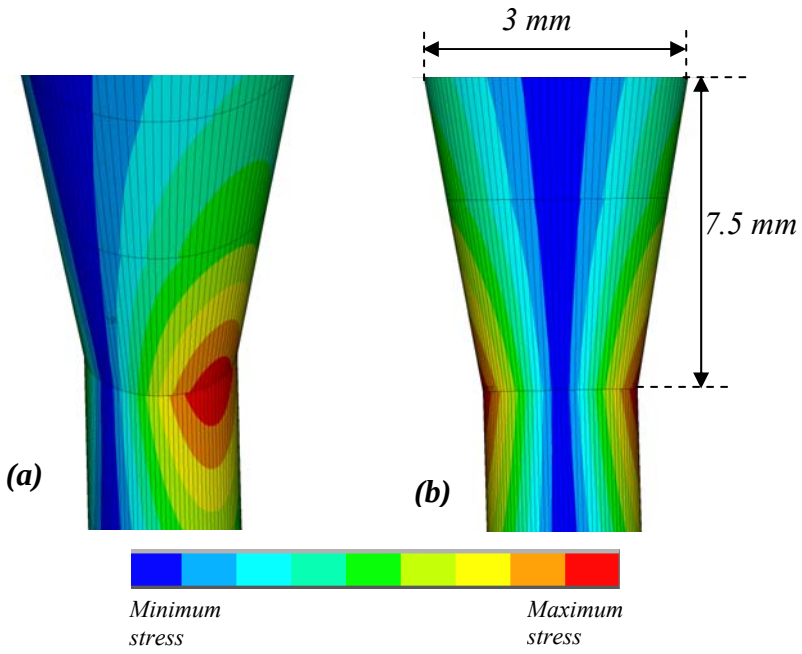

Figure 4.9. (a) Contour lines showing stress due to bending of the tapered (7.5 mm long) fibre , (b) front view of the same fibre seen bending equally from both sides.

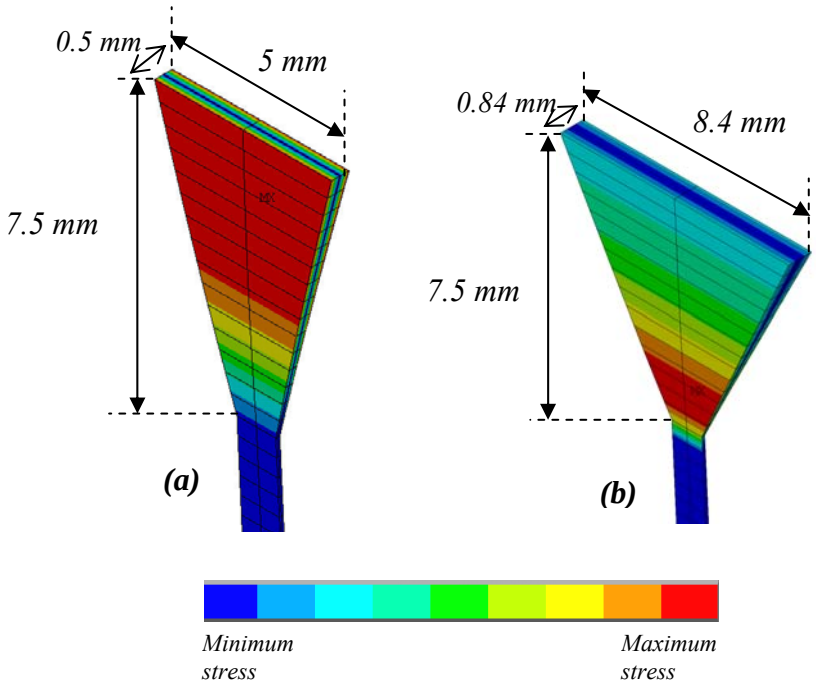

Figure 4.10. (a) Contour lines showing stress due to bending of the tapered (7.5×5×0.5 mm) ribbon, (b) ribbon (7.5×8.4×0.84 mm).

It can be seen that maximum stress due to bending takes place at the junction of the tapered neck and the uniform region of the fibre (figure 4.9a). The stress plot compliments the calculated value of bending length from ANSYS® which is 8.3 mm (exactly the same distance where maximum stress is seen). In Figure 4.9(b) the fibre is seen bending equally on both its sides (which is a useful check of the model). This shows that the necks in the fibres are very stiff and hence they resist bending.

The ribbons behave differently. Figure 4.10(a) plots the stress for the ribbons where the starting dimensions are 5 mm wide by 0.5 mm thick. The stress generated in the ribbon due to bending is seen to occur entirely in its thicker region within the tapered portion. The neck in the ribbon being thinner and hence less stiff bends far more easily than the fibre.

Figure 4.10(b) shows the stress distribution for a ribbon whose starting dimensions are 8.4 mm wide by 0.84 mm thick, thus having a cross sectional area equal to the fibre studied. Now the ribbons are stiffer and hence the bending behaviour is modified. The maximum value of stress is seen at the lower portion of the tapered neck of the ribbon.

The next step is to estimate the magnitude of strain energy in the fibre and ribbon for the tapered cases. This will allow an estimation of dilution factor of the pendulum.

Figure 4.11 shows the energy distribution in the fibre having a 7.5 mm long tapered neck. The dotted line indicates the bending point of the fibre. The strain energy is mostly concentrated at the thick section of the fibre (within the 7.5 mm taper) and the thinner section of the fibre bends very little. As one can see, the strain energy initially increases as a function of length along the fibre and reaches its peak at around 7.5 mm. It then reduces

steeply and finally comes to a negligible value after approximately 10.5 mm. The bottom section of the fibre contains a negligible amount of strain energy and hence has not been plotted.

The strain energy distribution in both the ribbons studied is shown in figure 4.12. The red bars represent strain energy in the ribbon of initial dimensions 5 mm wide by 0.5 mm thickness. The strain energy values decreases as a function of length along the ribbon. The maximum value is seen at the very beginning of the ribbon, which gradually decreases and becomes negligible after approximately 7 mm. The blue bars represent the ribbon with initial dimensions 8.4 mm wide by 0.84 mm thickness. There the strain energy distribution gradually increases, reaches a peak and then gradually decreases. The energy is spread over the first 8.5 mm of the ribbon. Hence on increasing the stiffness of the ribbon, the energy is distributed further along its length.

Simple analytical calculations exist only for the cases where the suspension elements have uniform cross sectional area (i.e. for no neck case), hence F. E analysis is essential to estimate the dilution factors for the more complex cases.

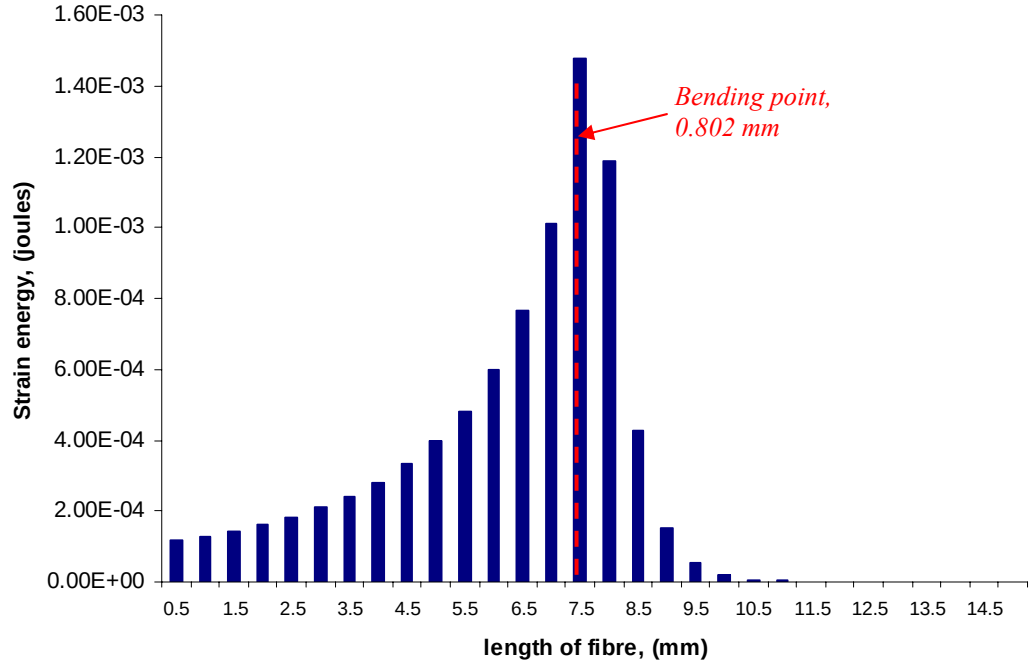

Figure 4.11. Graph showing the energy distribution in a single fibre with 7.5 mm tapered section, suspending a mass of 10 kg. The dotted line shows the bending point of the fibre.

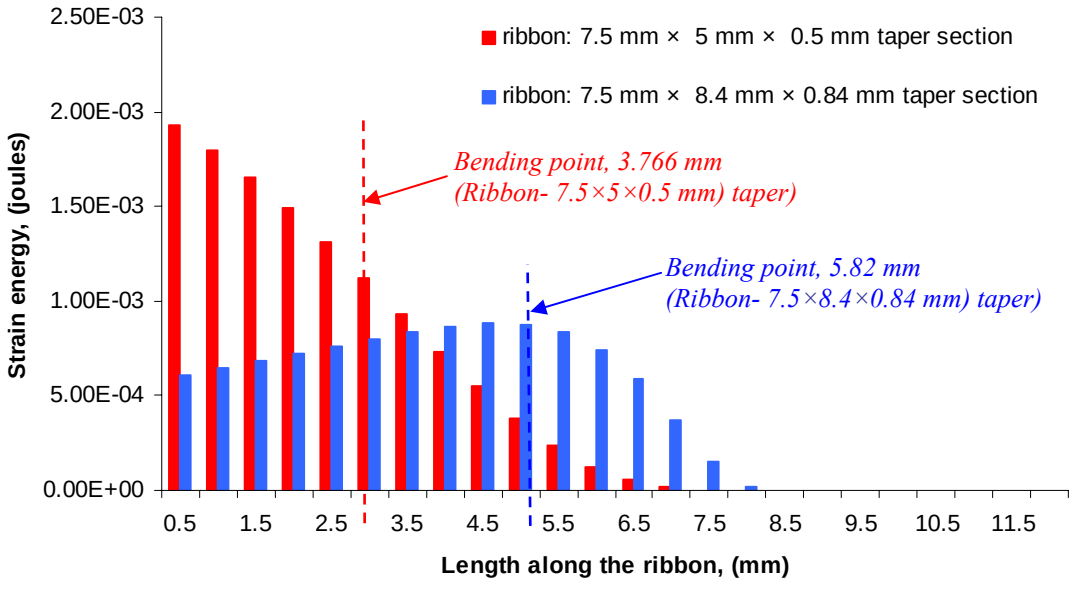

Figure 4.12. Energy distribution in a single ribbon with tapered necks suspending a mass of 10 Kg. The red bar represents energy in the 5 mm×0.5 mm taper cross section ribbon and the blue bars represents the 8.4 mm×0.84 mm tapered cross section ribbon.

Table 4.6(a) shows the dilution factor estimated for the case of a single fibre with 7.5 mm long tapered neck, suspending a mass of 10 kg. The dilution factor in this case is found to be 872 using ANSYS®. This is reduced by a factor of 1.61 over the case where no tapered neck was included. The necks are participating in the bending process and hence reducing the energy contained in the thin section of the fibre. Recall, equation 4.3 says that the dilution factor is inversely proportional to the square of the diameter of the fibre. Hence if bending occurs at the thicker ends, this will result in lower dilution numbers.

Case	Pendulum Design	Dilution factor: (ANSYS®)	Dilution factor: (THEORY) (for no neck case)
(a)	Silica fibre (7.5 mm linear tapered neck)	872	1405
(b)	Ribbon with (7.5×5×0.5 mm) tapered neck	590	4511
(c)	Ribbon with (7.5×8.4×0.84 mm) tapered neck	702	4511

Table 4.6. Dilution factors calculated for (a) a single fibre with 7.5 mm long tapered neck and (b) for single ribbon with a 7.5 mm long tapered neck (5mm×0.8mm) and (c) 8.4×0.84 mm cross sections, suspending a mass of 10 kg.

The ribbons in comparison experience a steeper fall in the dilution factor numbers. Looking at table 4.6, the dilution factor estimated for a ribbon with a 7.5 mm×5 mm×0.5 mm tapered neck decreases by a factor of 7.65 over the case of having no tapered neck. The stiffer ribbon of taper dimensions 7.5 mm×8.4 mm×0.84 mm fares marginally better but is still a factor of 6.42 away from the original case. The decline in the dilution numbers is due to the concentration of strain energy in the thickest section of the ribbon.

4.4.2 Analysis of 15 mm long linear tapered necks in the fibre or ribbon of the pendulum system

The length of the necked region in the fibre was varied to study its effect on the dilution factor. In this case the length was increased to 15 mm as compared to 7.5 mm in the previous case. Figure 4.13 shows the ANSYS® design of the longer neck used in the fibre. Similarly for the case of ribbon, the length of the taper region was increased to 15 mm, as shown in the same figure.

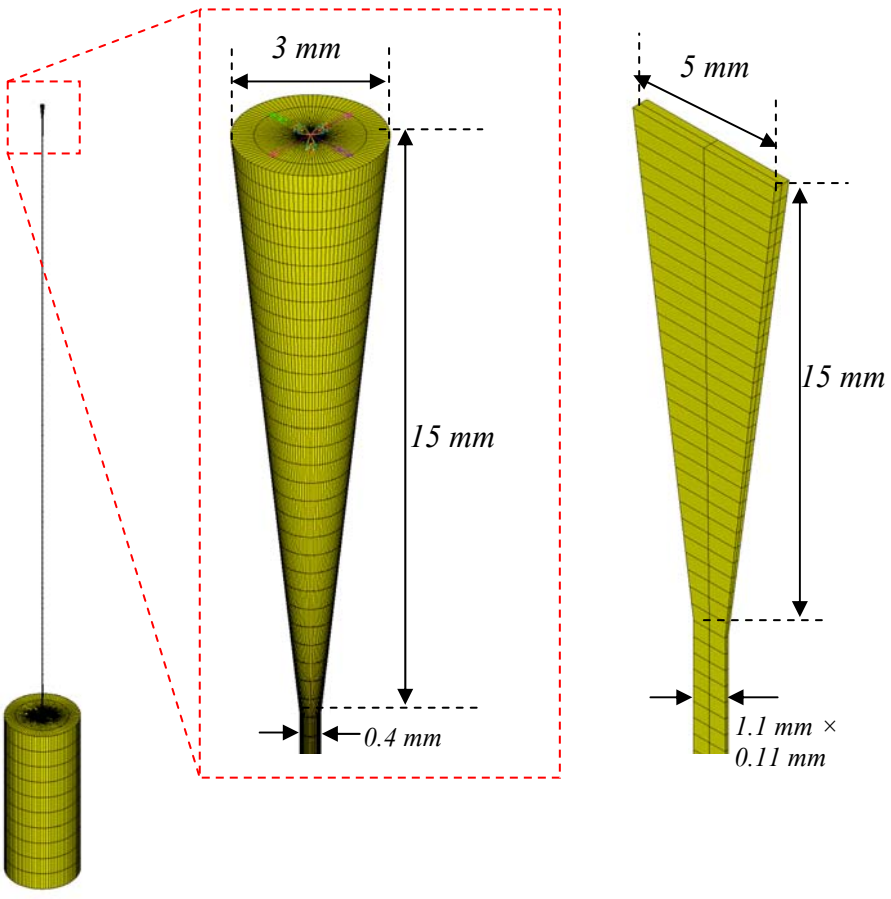

Figure 4.13. ANSYS® model of single fibre consisting of 15 mm long linear tapered neck at its ends, suspending a mass of 10 kg. A comparative ribbon model is shown on the right hand side.

Case	Bending length (ANSYS®), (mm)
Fibre with 15mm tapered neck	13.47
Ribbon with 15 mm tapered neck (cross section-5×0.5 mm)	4.89

Table 4.7. Bending length of a single 'linear tapered (15 mm)' fibre and ribbon, with each suspending a mass of 10 kg (calculated in ANSYS®).

Table 4.7 gives the bending length calculated from ANSYS® for the linearly tapered fibre and ribbon of taper length 15 mm.

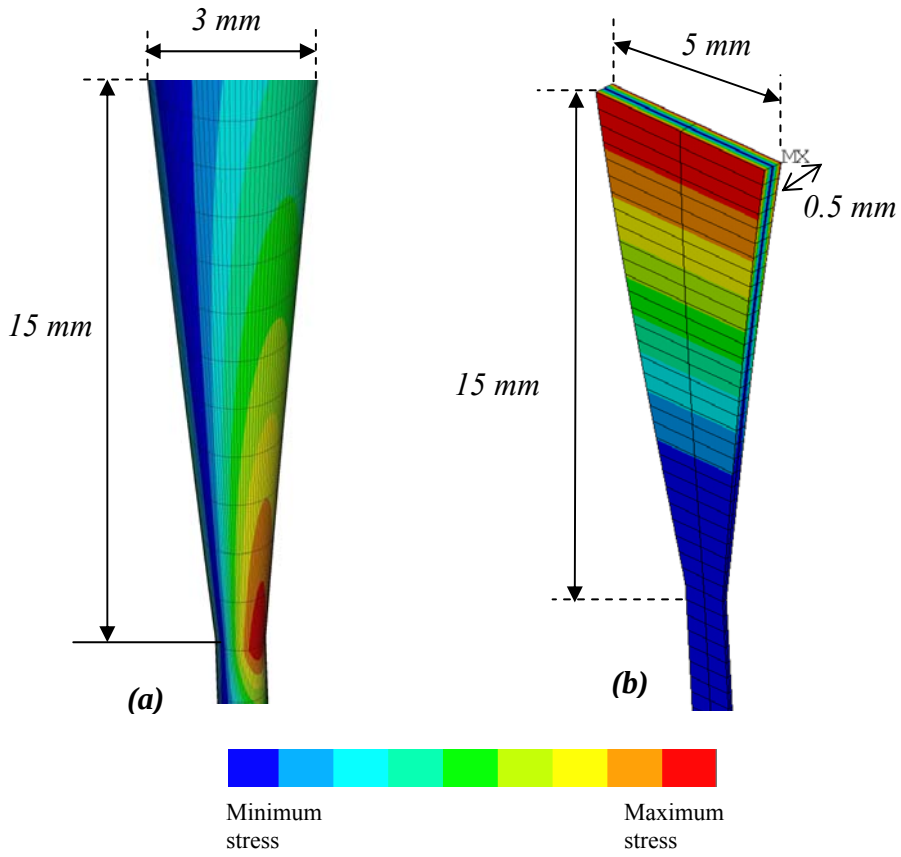

Figure 4.14. Contours showing stress due to bending in a fibre and ribbon with 15 mm linear tapered necks.

The stress distribution in the fibre and ribbon is plotted in the form of contour lines and is shown in figure 4.14. The maximum stress value is found at the junction of the neck and uniform section of the fibre. The ribbon in contrast is mostly stressed at its very top. The difference in the stress distribution is once again related to the stiffness of the suspension material.

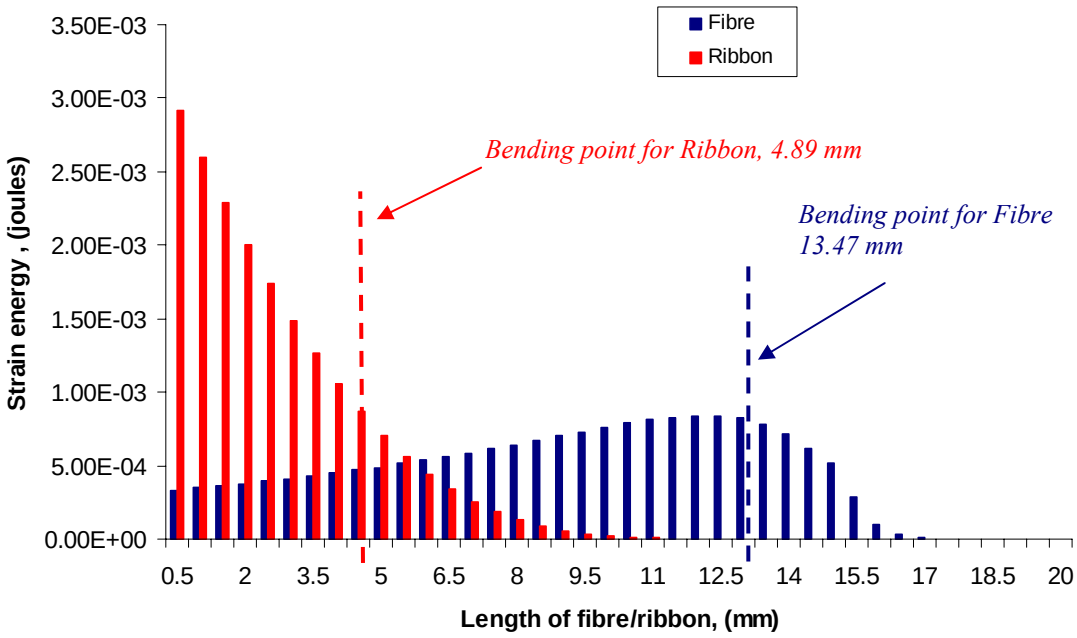

Figure 4.15. Strain energy distribution in a fibre and ribbon with 15 mm tapered neck, suspending a mass of 10 kg.

Figure 4.15 plots the strain energy distribution in the fibre and the ribbon. The red bars correspond to the energy in the ribbon and the blue bars correspond to the energy in the fibre. The dotted lines show the bending point in each case. The graph shows considerable difference in the distribution of energy in the fibre and ribbon respectively.

On increasing the length of the taper region the strain energy is distributed further along the length (Strain energy in the fibre is seen until 17 mm along its length and for the ribbon until 11 mm along its length).

The dilution factors for the cases of single fibre or ribbon pendulum system with 7.5 mm linear tapered neck ends is shown in table 4.8. The table shows a reduction in the dilution number as compared to previous model. If one compares this model with the fibre without necks included, the dilution is reduced by a factor of 3.5. The situation is worse for the ribbon as its value is reduced by a factor of 11.84.

Pendulum Case	Dilution: (ANSYS®)	Dilution: (Theory- for no neck case)
Fibre (15 mm linear taper)	401	1405
Ribbon(15 mm linear taper)	381	4511

Table 4.8. Dilution factor calculated in ANSYS® and compared with theory for the case of a single fibre and ribbon with 15 mm linear tapers suspending a mass of 10 kg in each case.

This shows that the length of the taper section is very critical for obtaining a high dilution factor. Thus the calculations above were extended to cover a range of length of the necks.

4.5 Optimisation of the fibre and ribbon neck length to achieve high dilution factor

The effect of varying the length of the neck region upon the dilution factor is summarised by looking at the graph plotted in figure 4.16. The graph suggests that the ribbons would be only good for use if one can fabricate them with a very short neck (less than 3 mm). However practically that is very difficult to achieve. Once the neck length is more than 4 to 5 mm, then there is virtually no difference between fibre and ribbon with respect to the dilution factor in the pendulum.

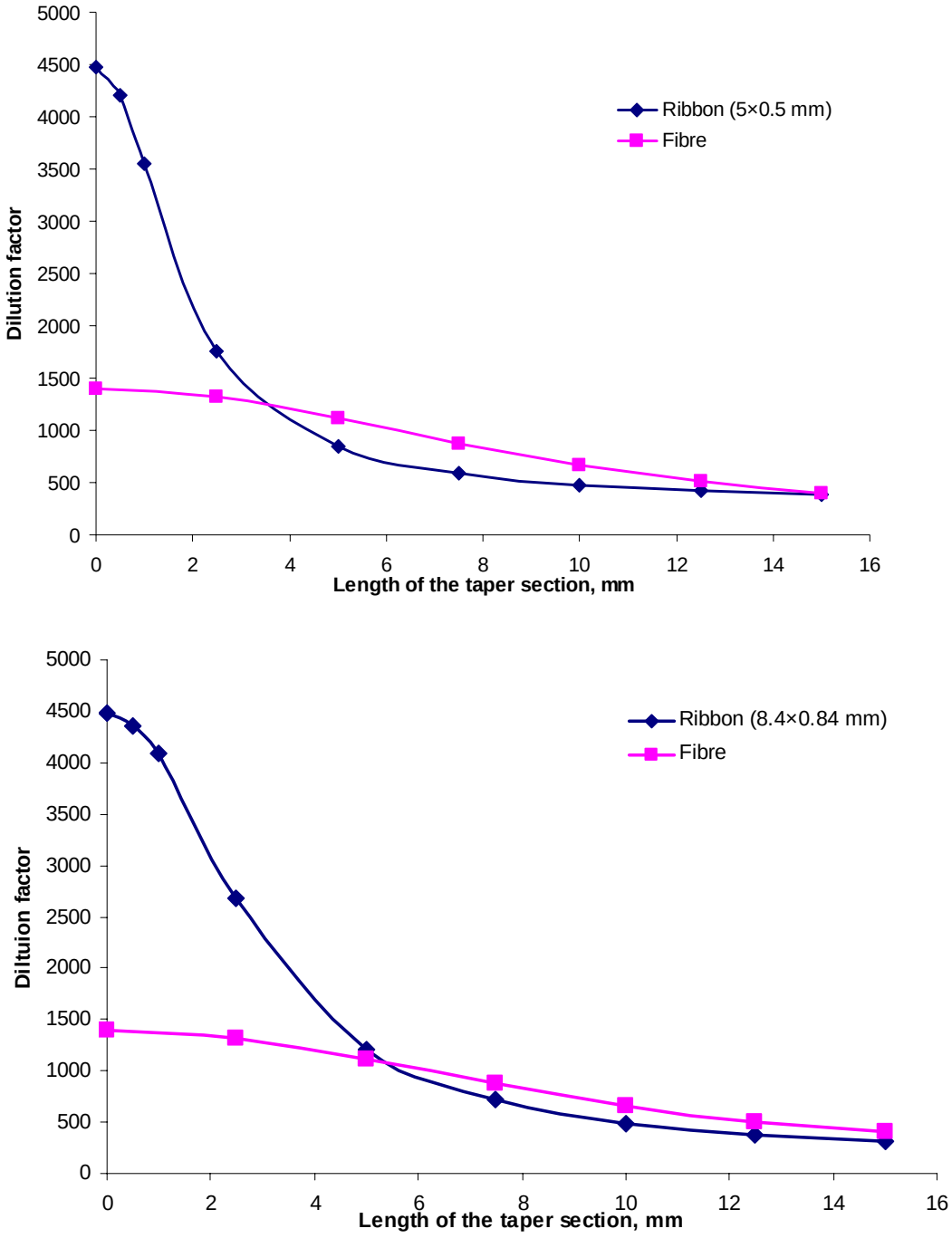

Figure 4.16. Top graph - plot of dilution factor vs. length of the neck (taper) in fibres and ribbons (starting cross section area is taken for a real ribbon, i.e. 5×0.5 mm). Bottom graph – plot of dilution factor vs. length of the neck (taper) in fibres and ribbons (cross section area of ribbons made equal to that of fibre after the neck region).

4.6 Summary of results and conclusions

Pendulum Case	Dilution (ANSYS®)	Dilution (Theory)
Uniform fibre	1396	1405
Fibre with linear tapered neck(taper length 7.5 mm)	872	1405
Fibre with linear tapered neck(taper length 15 mm)	401	1405
Uniform ribbon	4478	4511
Ribbon with linear tapered neck (7.5mm×8.4 mm×0.84 mm)	590	4511
Ribbon with linear tapered neck (7.5 mm×8.4 mm×0.84 mm)	702	4511
Ribbon with linear tapered neck (taper length 15 mm)	381	4511

Table 4.9. Summary of Dilution factor numbers for all the cases studied for single fibre or ribbons suspension elements supporting mass of 10 kg.

Table 4.9 compares the dilution factor for all the cases studied. These results indicate that inclusion of tapered sections in the suspension elements consistently results in a lowering of the dilution factors. The percentage decrease of the dissipation dilution factor for a pendulum employing tapered fibre is much less than that for the tapered ribbon. Results have also shown that the length of the neck region plays a significant role in reducing the dilution factor. The longer it gets, the greater is the effect on dilution. However, in reality

the fibres or ribbons cannot be pulled without the necks. Hence it appears that to maximise the dilution it is desirable to keep the necks as short as possible.

These models of single fibre or ribbon suspending a mass are an important step towards designing a more complex model. Next we consider the case of a pendulum having two suspension elements.

Chapter 5

Two-fibre suspension design

5.1 Introduction

An intermediate model was designed in ANSYS® which acted as a bridge between the single fibre pendulum and the complex four fibres design used for the Advanced LIGO suspension systems. A two fibre model was thus studied to extend the ANSYS® results obtained in chapter 4.

The fibres here are bonded to the top surface of a 20 kg mass. The design of the fibre has been kept the same as discussed in chapter 4. The first section of this chapter discusses suspension elements of uniform cross section, followed by study of linear tapered necks in the fibre. In the final section of this chapter a more complex design is modelled to further investigate some issues observed while analysing this pendulum system. Discussions of ribbons have been omitted for simplicity.

5.2 ANSYS® model of a pendulum system consisting of two silica fibres suspending a mass (20 kg)

The two-fibre suspension model is an extension of the single fibre pendulum design and is an important step towards modelling the Advanced LIGO design. Initially two different models were designed in ANSYS®, one with cylindrical fibres having uniform cross sectional area and the other with linear tapered ends. Figure 5.1(a) shows the ANSYS® model of two cylindrical fibres of uniform cross section area suspending a mass of 20 kg. The length of each fibre is 600 mm with diameter 0.4 mm. The fibres are attached to the top of the mass and are 30 mm apart. The dimension of the mass remained the same, however its density has been increased such that it weighs 20 kg. A second design was modelled where the uniform fibres were replaced by the fibres having tapered neck. Figure 5.1(b) shows two fibres with linear tapered neck at its top and bottom cross section. The length of the taper section was taken as 7.5 mm (with a starting diameter of 3 mm). These models were solved using both static and modal analysis. The mode frequencies were obtained and are shown in the table 5.1.

Case	Rotational mode, Hz.	Longitudinal pendulum mode, Hz	Transverse pendulum mode, Hz	Longitudinal pitch mode	Transverse pitch mode	Bounce mode	1st Violin mode
Uniform fibre	0.4565	0.6057	0.6175	3.19	3.78	6.214	497.759
Tapered fibre	0.4617	0.6087	0.6021	3.384	3.927	6.282	509.09

Table 5.1. Mode frequencies estimated from ANSYS® for the case of uniform fibres and 7.5 mm tapered fibres in the two-fibre pendulum system (mass - 20 kg).

The pendulum mode frequencies are of particular interest and will be discussed next.

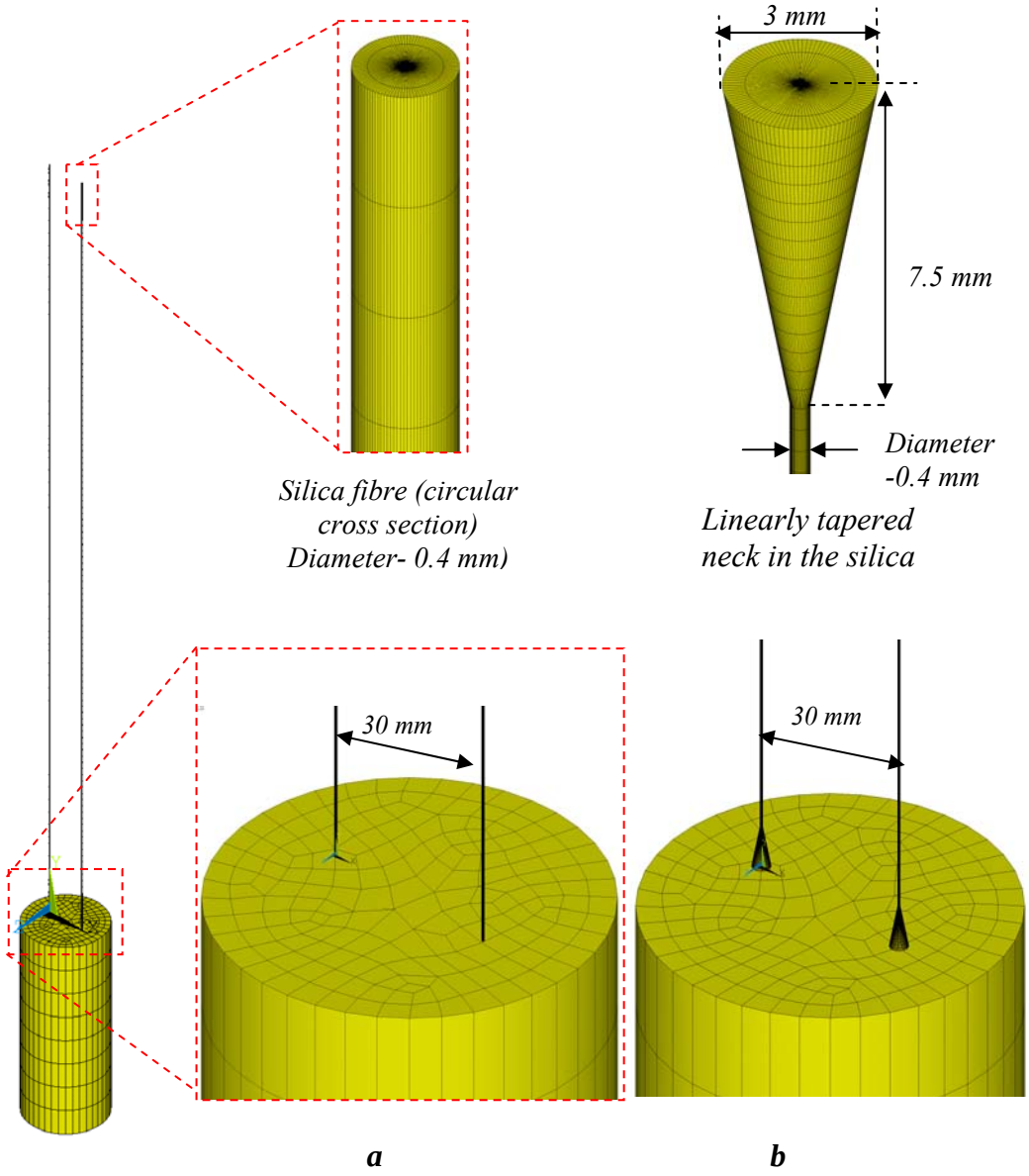

Figure 5.1. Two silica fibres suspending a mass of 20 kg. Case "a" represents simple cylindrical fibres of uniform cross section, case "b" represents "7.5 mm linearly tapered" fibres.

5.2.1 Study of longitudinal pendulum mode (for uniform cross section and linear tapered fibres)

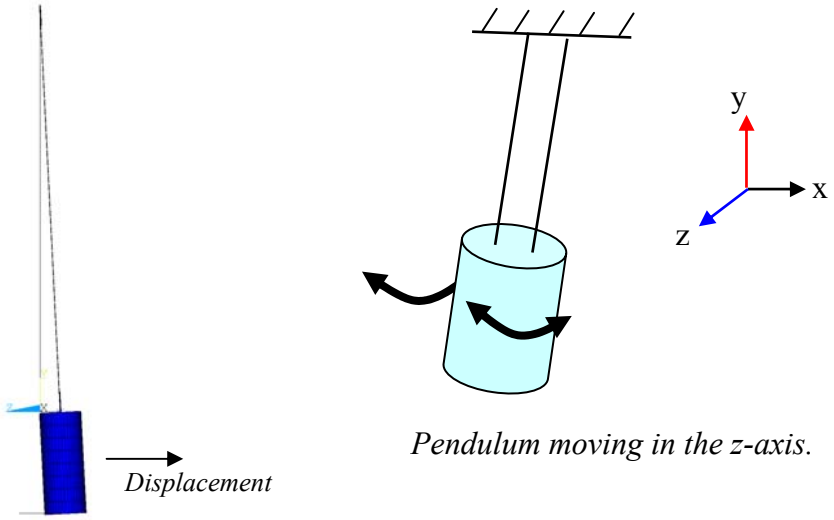

Figure 5.2. Longitudinal displacement of a two fibre pendulum system.

The deformed mode shape for the longitudinal pendulum mode of vibration is shown in figure 5.2. The equilibrium position of the pendulum is shown by the straight line in the figure (shown on the left side of figure 5.2).

The bending length of each fibre is 0.96 mm and is the same as in the case of a single fibre suspending a mass of 10 kg. This is because the two fibres are supporting 20 kg of mass, hence each fibre is under a tension equivalent to 10 kg. The stress distribution in the cylindrical fibre in this case should be no different from the case of a single fibre suspending 10 kg. Figure 5.3 shows a plot of total strain energy distribution in the fibre (energy in both the fibres included in the graph). The fibre as expected is bending from the top, hence most of the energy is concentrated in the first few mm and it decreases sharply.

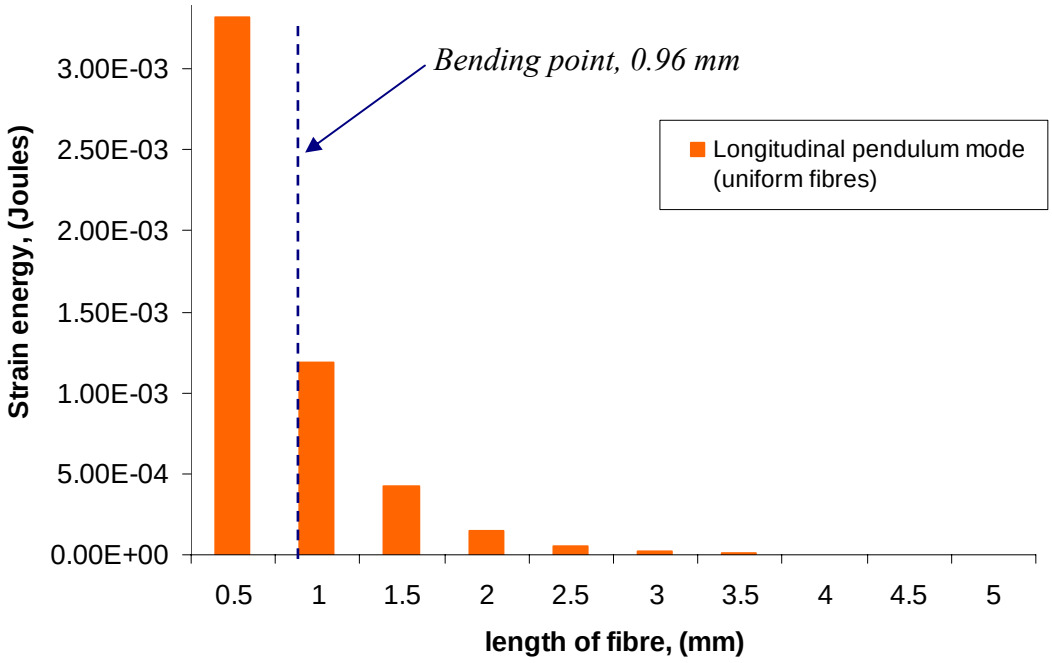

Figure 5.3. Plot showing energy distribution along the first 5 mm of the two-fibre pendulum system. Note: the value takes into account the energy in both the fibres.

For the case of linearly tapered (taper length 7.5 mm) fibres suspending a mass of 20 kg, the total strain energy distribution in the fibre is shown in figure 5.4. The tapered section of the fibres resists bending and hence there is very little energy at the starting few mm, as seen in the single fibre pendulum case too. However once the fibre starts to bend the energy gradually increases. The strain energy value peaks at a distance of 7.5 mm where the thin fibre joins the thick taper, once again this is due to the concentration of maximum stress at that point owing to the proximity of the bending point (8.02 mm).

Once the strain energy in the fibre is studied, the dilution factor in the pendulum can be estimated, which is discussed next.

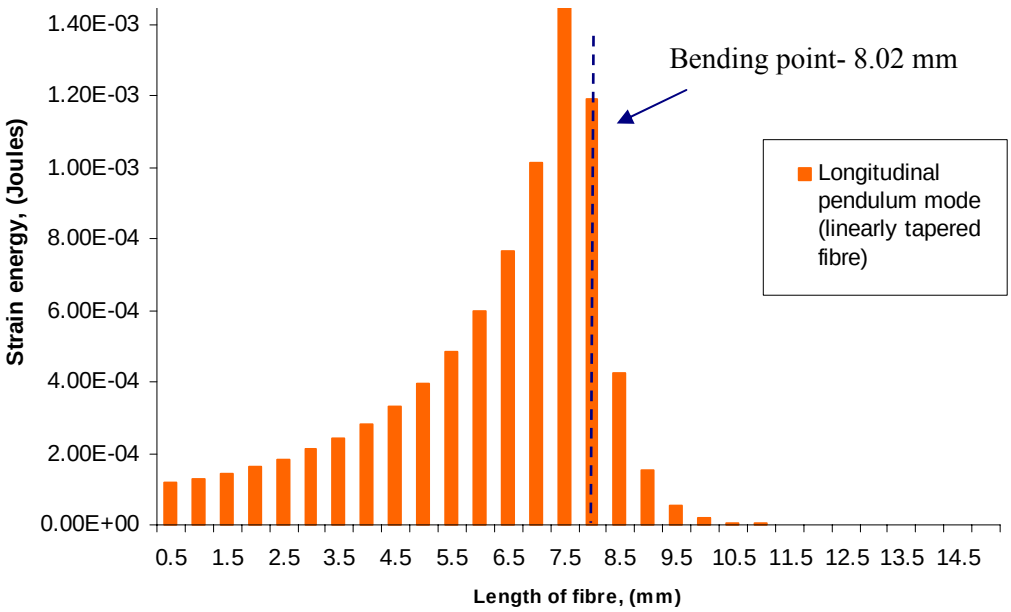

Figure 5.4. Plot showing energy distribution in two linear tapered (taper length-7.5 mm) fibres suspending a mass of 20 kg. Note: the value takes into account the energy in both the fibres.

The dilution factor in the pendulum system was calculated in ANSYS® as well as analytically and is shown in table 5.2. The method adopted was similar to that described in chapter 4.

Dilution factor (ANSYS®) Two fibres (no necks) suspending a mass of 20 kg	Dilution factor (ANSYS®) Two fibres (7.5 mm taper) suspending a mass of 20 kg	Dilution factor (theory) Two fibres (no necks) suspending a mass of 20 kg
1398	872	1405

Table 5.2. Comparison of dilution factor (longitudinal pendulum mode) found analytically and using ANSYS® for two fibres with and without liner tapers suspending a mass of 20

The dilution factor for the case of uniform cross section fibres suspending a mass of 20 kg agrees well (to within 0.5 %) with the theoretically calculated dilution. When the tapers are added to the fibre the dilution factor falls by almost one third. These results are consistent with the ones obtained in the single fibre pendulum case.

5.2.2 Transverse pendulum mode (for uniform cross section and linear tapered fibres)

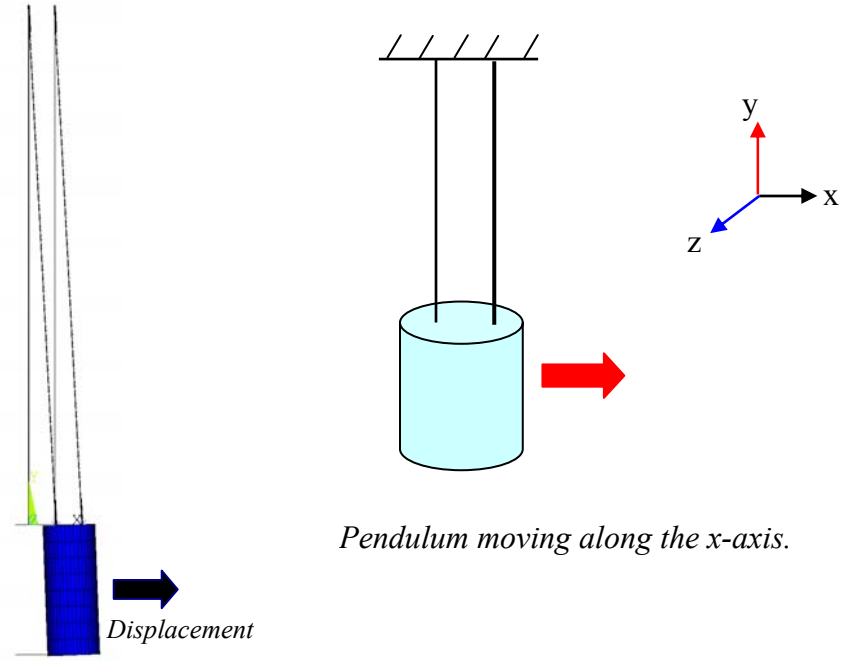

Figure 5.5. Deformed shape showing the transverse pendulum mode of two fibre suspending a mass of 20 kg.

The mode frequency for the transverse pendulum mode is found to be 0.6175 Hz which is slightly higher than the longitudinal pendulum mode. The oscillation of the pendulum system is perpendicular to the axis of the longitudinal pendulum mode. Figure 5.5 shows the deformed and the un-deformed mode shape of the two fibres suspending a mass of 20 kg.

In figure 5.6 the total energy distribution in the fibres suspending a mass (20 kg) is plotted for the transverse pendulum mode. The top and bottom of the fibres are bending in the expected way. However it can be seen that there is a significant amount of energy in the entire fibre. In previous models studied, the energy in the middle section of the fibre

reduced to a negligible value. It was initially postulated that the continuous band of energy seen is actually the stretch energy in the fibre due to a mass of 20 kg stretching the fibre in the presence of gravity. However, this is seen only for the case of the transverse pendulum mode and not for the longitudinal pendulum mode and thus cannot be correct. This will become clearer later in this chapter, where it is shown that this effect arises from coupling of the tilt (pitch) mode of the mass. This coupling of tilt causes the fibres to stretch. A further analysis of this effect has been done by M. Barton and is discussed in the literature [55].

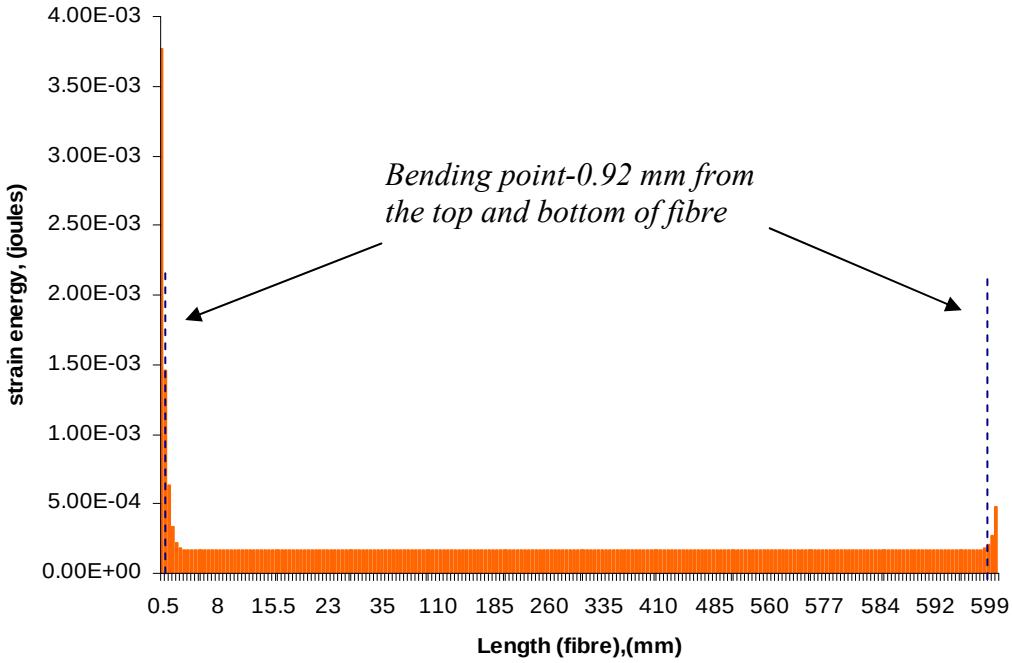

Figure 5.6. Strain energy distribution in two fibres suspending a mass of 20 kg, this is plotted for the transverse pendulum mode.

The plot in figure 5.7 gives the energy distribution in two fibres having tapered ends and is suspending a mass of 20 kg for the transverse pendulum mode. The tapered ends of the fibre bend as expected but the presence of energy in the centre is again unexpected. Before investigating the energy distribution further, the consequences of this energy on the dilution factor of the pendulum were investigated.

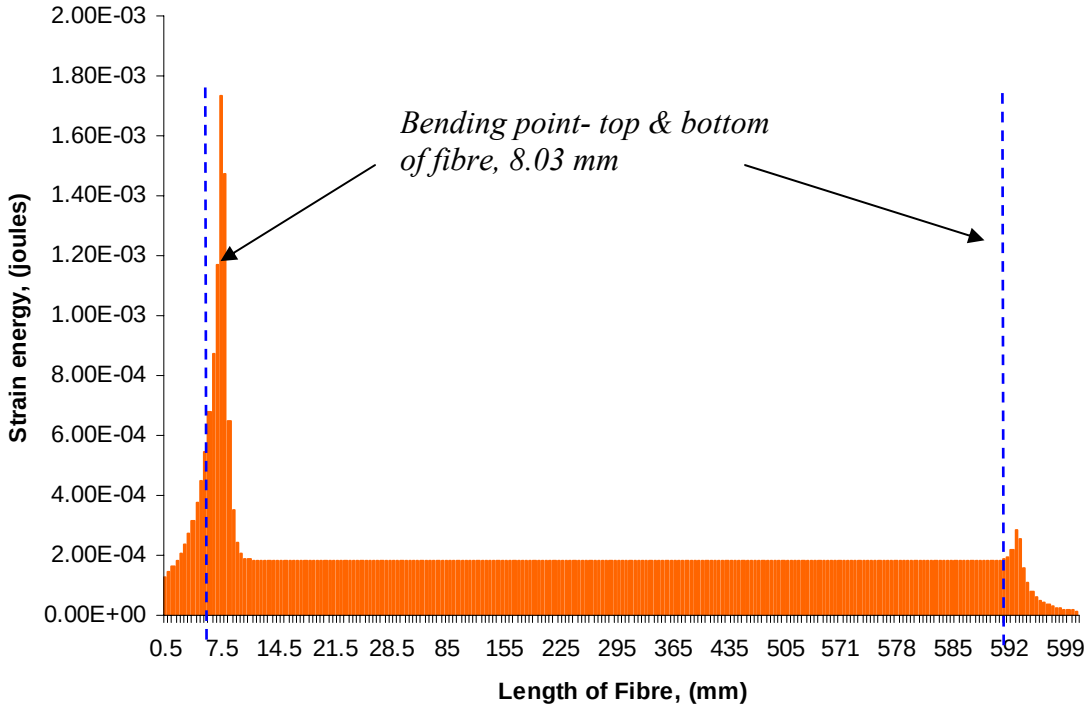

Figure 5.7. Strain energy distribution in two linear tapered (taper length 7.5 mm) fibres suspending a mass of 20 kg, transverse pendulum mode.

The dilution factor for two fibres suspending the 20 kg mass was found using ANSYS® and then compared with theory. Since the transverse pendulum mode showed energy distribution along the length of the fibres, the estimation of dilution factor was broken down into two different cases.

In case one the dilution factor was calculated using the total strain energy present in the entire fibre. In case two the continuous band of energy seen in the middle of the fibre was neglected while the energy within the top and bottom 8.5 mm (approximately) of the fibres considered.

ANSYS Pendulum model	Dilution factor (ANSYS) (total strain energy in the fibre)	Dilution factor (ANSYS) (strain energy only at top and bottom of fibre)	Dilution factor (Theory-for uniform fibre case)
Fibres (of uniform cross sectional area)	37	774	703
Linear tapered (taper length -7.5 mm) fibres	34	534	703

Table 5.3. Comparison of dilution factor obtained analytically and by FEA of a 20 kg pendulum suspended by two fibres for the transverse pendulum mode. Where the fibres were modelled as having uniform cross sectional area and linearly tapered necks of 7.5 mm respectively.

Looking at table 5.3, the dilution factor estimated for the case uniform fibres (where strain energy values are considered only at the top and bottom of the fibres) aggress to within 10% with theory.

The addition of linear tapers in the fibre reduces the dilution factor by 24 %. The results vary significantly once the total energy in the fibre is taken into account. The figure shows that the dilution factor drops to 37 for the uniform fibres and 34 for tapered fibres.

To gather more information on this problem and to test a hypothesis that mode coupling might be affecting the dilution, it was suggested that the fibres be bonded on a line through the centre of mass of the suspended 20 kg mass. This was also more consistent with the Advanced LIGO detector where the fibres are attached very close to the ‘centre of mass’ of the 40 kg suspended mass.

5.3 Two fibres model, fibres attached in level with the centre of mass

Figure 5.8 shows a schematic of the new design. The two fibres are again suspending a mass of 20 kg and the dimensions of the pendulum system remain unchanged. The fibres here are bonded to a line through the centre of the mass of the pendulum. In order to achieve this, a special solid mass was designed with a slot as shown in figure 5.8(a), such that the fibres could penetrate the mass and be attached within the body of the mass. The mass was designed with slots such that the fibres could move longitudinally as well as transversally. The uniform fibres were then replaced with tapered fibres to study the effect on the dilution factor. At first, the strain energy distribution in the pendulum mode for the case of uniform fibres and tapered fibres were studied.

In figure 5.9 the total strain energy distribution along the length of the uniform fibre is plotted. The blue bars represent the energy in the longitudinal pendulum mode and red bars indicate the transverse pendulum mode. The graph shows the energy is concentrated at the top and bottom of the uniform fibre. There were insignificant amounts of energy in the middle of the fibres in contrast to the case studied earlier where fibres were attached to the top of the mass. As seen in the graph, the strain energy decreases to a negligible value after around 3 mm and increases again only after around 597 mm. This shows that the fibres are bending only at the top and bottom few mm and are not stretching significantly.

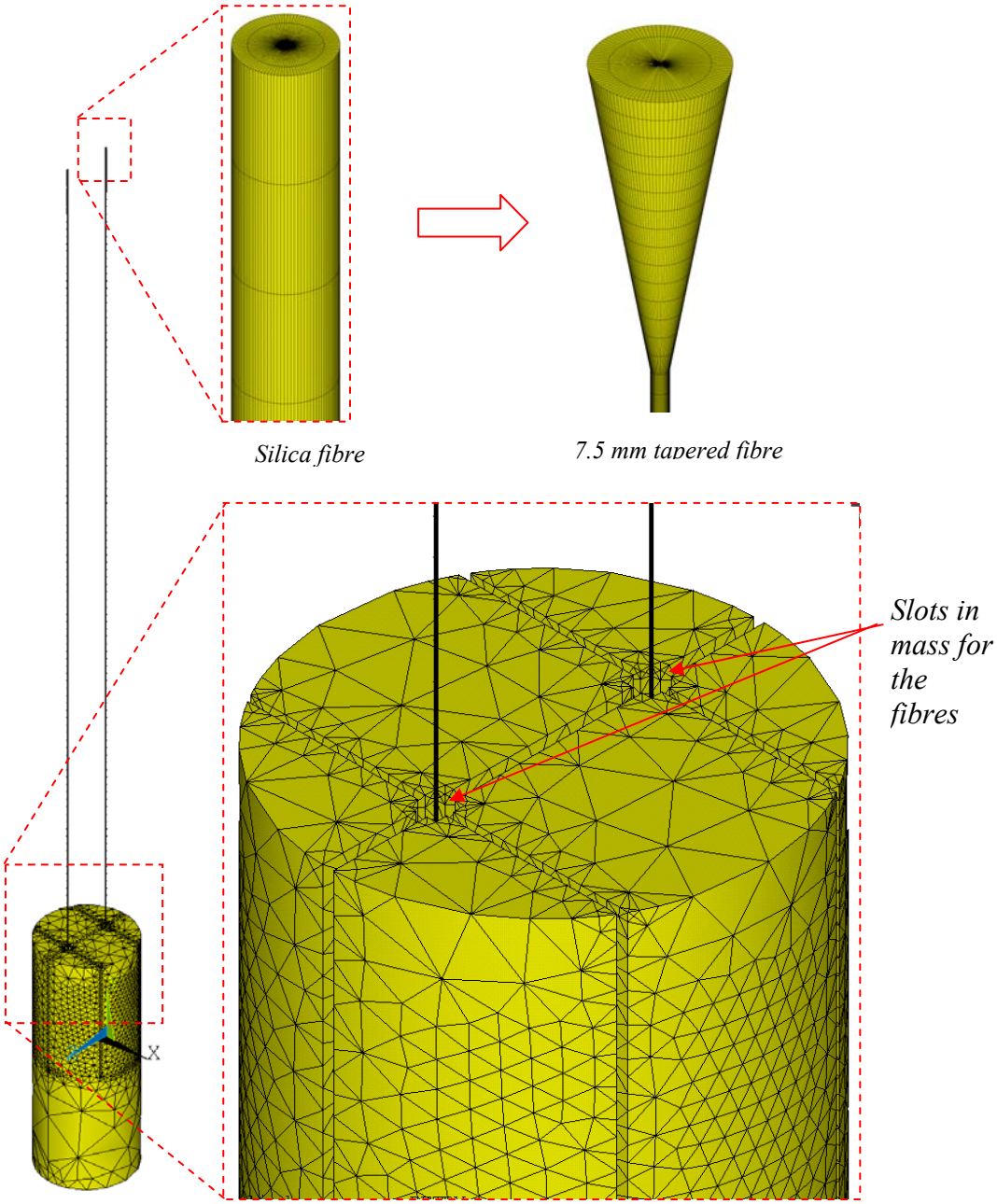

(a), Fibres penetrating the mass through cavity

Figure 5.8. Schematic of two fibres suspending a mass of 20 kg. (a) specially prepared slots in the mass to let the fibres penetrate through it and bond at its centre.(b) tapered fibres (taper length-7.5 mm) replacing the uniform cross section area fibres.

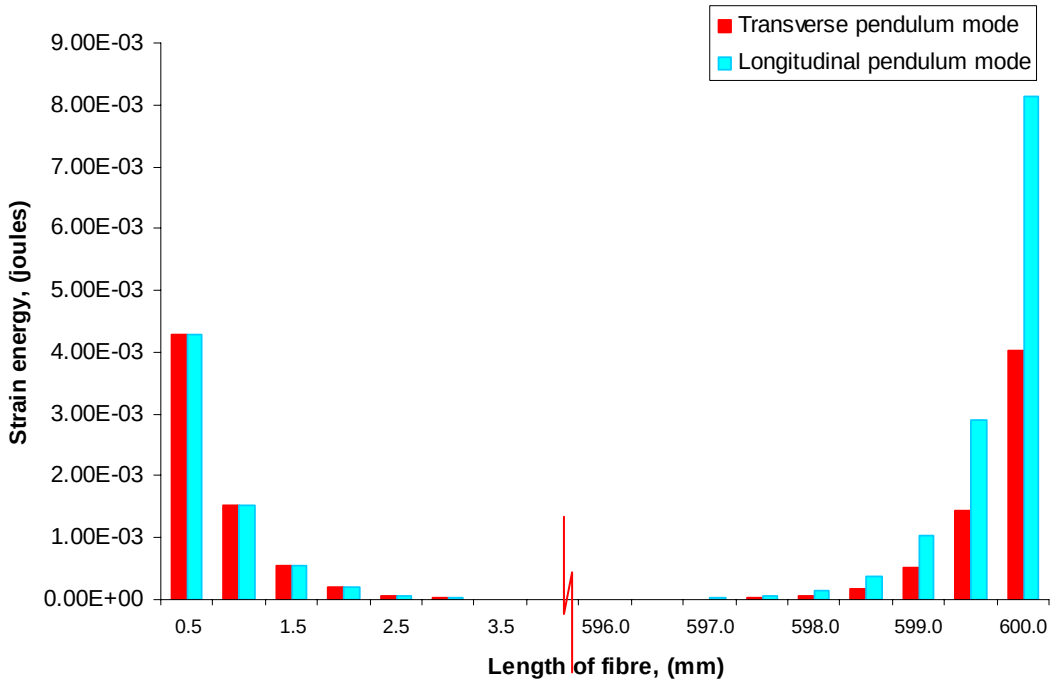

Figure 5.9. Plot showing the strain energy distribution in top and bottom portions of two fibres attached to centre of the mass (20 kg). Blue bars signify the longitudinal pendulum mode; red bars indicate the transverse pendulum mode.

The most important point to note is that for the transverse pendulum mode, there is much less energy associated with the stretch in the fibre, and this is interpreted as there being much lower coupling to the relevant pitch mode of the mass. This is because the bending points of the fibre are much closer to the line of the centre of mass and thus exert a much smaller coupling to excite the pitching. Although it is not really relevant for the Advanced LIGO, it is interesting to consider the situation for the longitudinal pendulum mode (plotted in blue bars in figure 5.9). There is now strain energy in the bottom portion of the fibre and it is higher than that in the top portion. The fibre is seen bending more at its bottom where it is attached to the centre of the mass.

On investigating the deformed shape of the longitudinal pendulum mode in ANSYS®, it was seen that the mass was actually pitching in the relevant dimension for coupling of the longitudinal pendulum mode. This can be seen in figure 5.10.

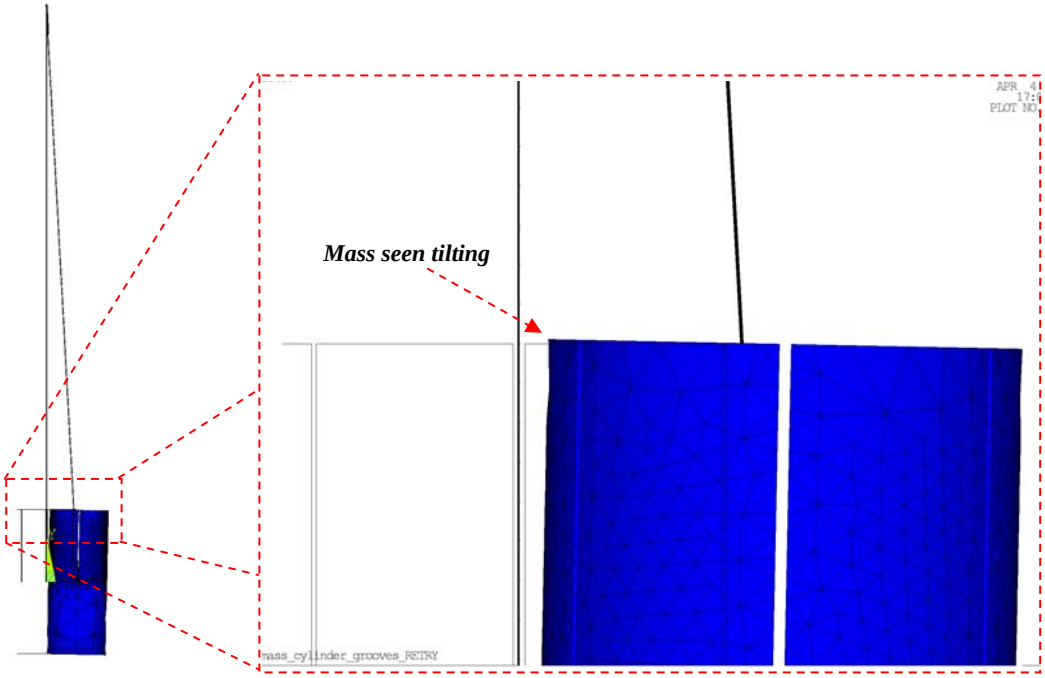

Figure 5.10. The mass is seen pitching due to mode coupling between the longitudinal pendulum mode and the pitch mode.

The figure shows the deformed and the un-deformed mode shape of the longitudinal pendulum mode. The enlarged picture taken from ANSYS® shows the mass tilting.

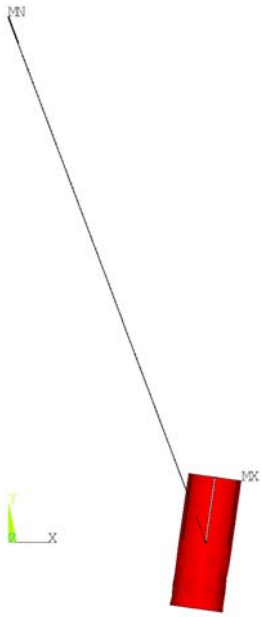

Figure 5.11. Displacement of the two fibre longitudinal pendulum mode attached to the centre of mass, where the mode coupling phenomenon leads to the mass pitching.

Figure 5.11 shows the displacement of pendulum associated with the longitudinal pendulum mode for uniform fibre case. In this figure the pitching of the mass is exaggerated to aid interpretation of the results found for the distribution of strain energy at the bottom of the fibre. To properly understand this, a real pendulum system was built in the lab. The pendulum had two steel wires suspending a cylindrical mass. The wires were attached to its centre of mass. On giving a small push to the pendulum the mass was seen to be pitching very clearly.

Figure 5.12 shows the energy distribution in fibres having linear tapers (taper length 7.5 mm) for the case of the longitudinal and transverse pendulum mode. The energy at the bottom section of the fibre for both the pendulum modes is less than that at the top which suggests that the mass is tilting but with different phase. Due to the inclusion of tapered necks in the fibre, they are stiffer at the ends, and hence the coupling to the pitch mode is changed.

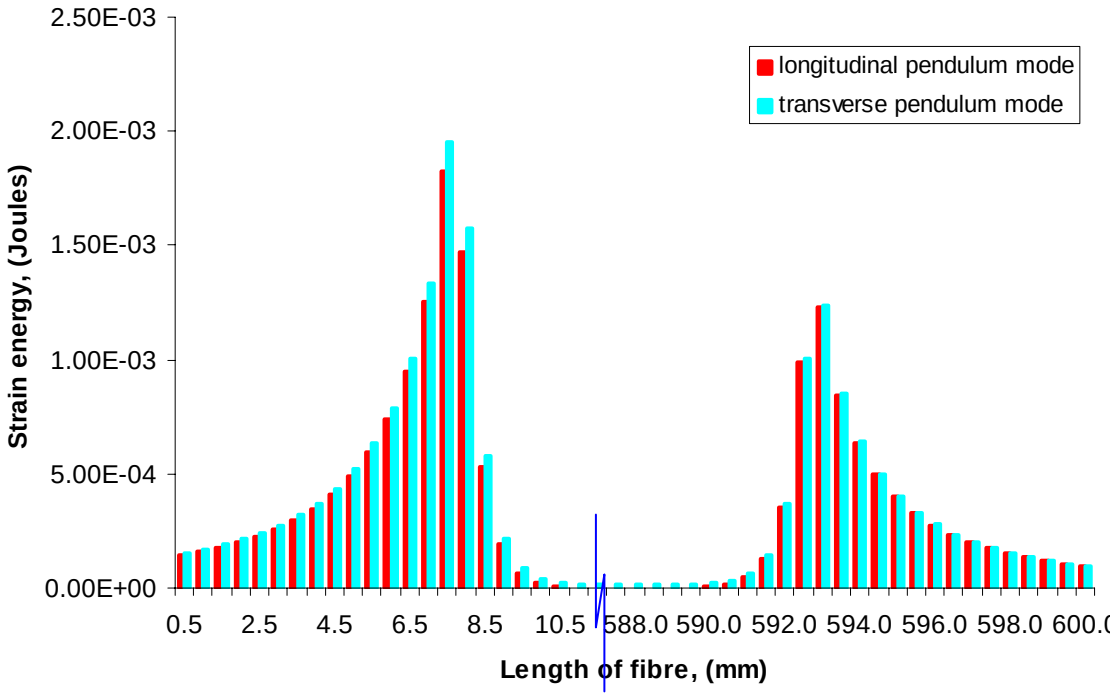

Figure 5.12. Graph showing energy distribution in top and bottom sections of two fibres having linear tapered ends (7.5 mm) attached to the centre of mass (20 Kg).Red bars signify the longitudinal pendulum mode, blue indicates the transverse pendulum mode.

Table 5.4 shows that the dissipation dilution for the transverse pendulum mode for the uniform fibres agrees with the calculated theory to within 1.5 % approximately. Addition of tapers to the fibres decreases the dilution factor in this case by 28 % (approximately). When one looks at the longitudinal pendulum mode, the ANSYS® results suggest that the dilution factor for the uniform fibres is lower than the tapered fibre. The decrease in dilution for the uniform fibres is due to the mode coupling effect or in other words the pitching of the suspended mass, as described earlier.

Cross section area of fibre	**Pendulum mode**	**Dilution factor (ANSYS)**	**Dilution factor (Theory)**
Uniform fibres	Longitudinal pendulum mode	424	625
	Transverse pendulum mode	634	625
Linear Taper (7.5 mm) fibres	Longitudinal pendulum mode	473	625
	Transverse pendulum mode	460	625

Table 5.4. Dilution factor calculated from ANSYS® and compared with theory for two fibres (uniform & tapered ones) attached on a line through the centre of mass of a 20 kg pendulum system.

5.4 Flexure point of the fibre at the centre of mass

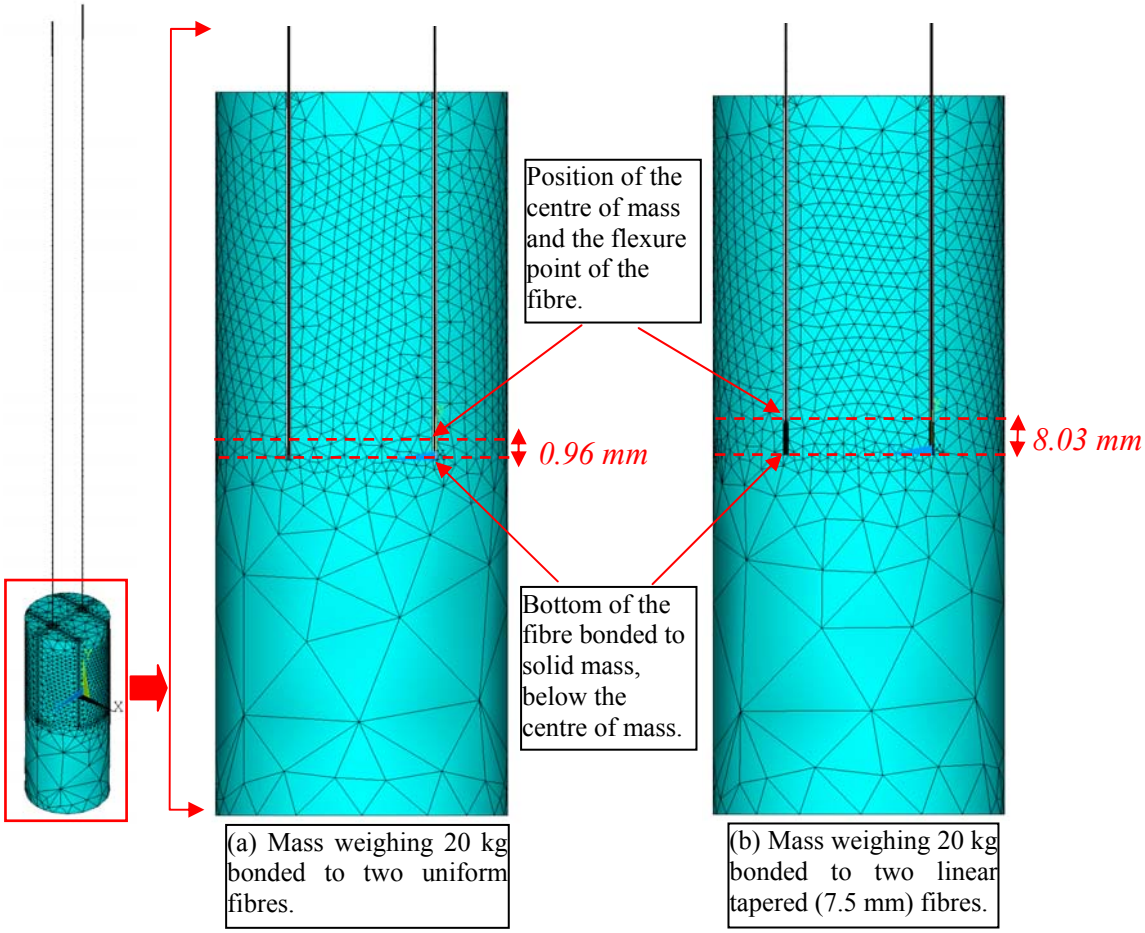

Figure 5.13. Schematic of two fibres suspending a mass of 20 kg. The fibres are bonded to the mass such that the flexure point is at the centre of mass. (a) Uniform fibres bonded to the mass. (b) linear tapered (taper length 7.5 mm) fibres bonded to the mass.

The bending point of the fibre was calculated from ANSYS® and verified from theory. The flexure point of the uniform fibre (diameter 0.4 mm) suspending 20 kg comes out to be 0.96 mm. Hence the fibre was moved 0.96 mm below the centre of mass of the system, as shown in figure 5.13(a). Due to this the flexure point and the centre of gravity of the mass coincide and helps to keep the mass stable. The same procedure was applied to the tapered fibre. Here the fibre was moved 8.03 mm (bending length of the linear tapered fibre for a taper length of 7.5 mm) below the centre of gravity, shown in figure 5.13(b). Once the

flexure point of the fibre was at the correct place, the model was solved in ANSYS® and the strain energy distribution and the dilution factor were studied.

Figure 5.14 shows the strain energy distribution in the uniform fibre of the pendulum system where the flexure point of the fibres is at the centre mass of the whole system, for both the longitudinal and transverse pendulum mode.

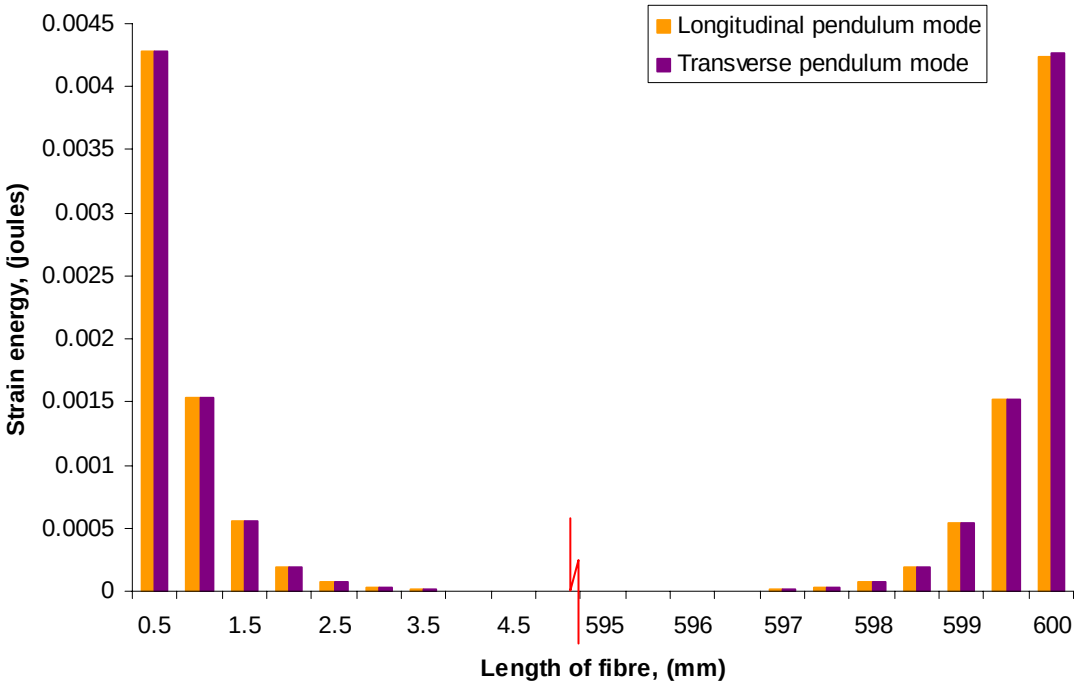

Figure 5.14. Graph showing strain energy distribution in two fibres, whose flexure point is at the centre of mass of the mass (20 kg): the orange bar stands for longitudinal pendulum mode, and the violet bar stands for transverse pendulum mode. The fibre is seen bending at the top and bottom.

The fibres are bending from the top and bottom, which is evident from the presence of strain energy there.

Similarly figure 5.15 shows the strain energy distribution in the linearly tapered fibre of the pendulum system where the flexure point of the tapered fibres is at the centre mass of the whole system, for both the longitudinal and transverse pendulum mode.

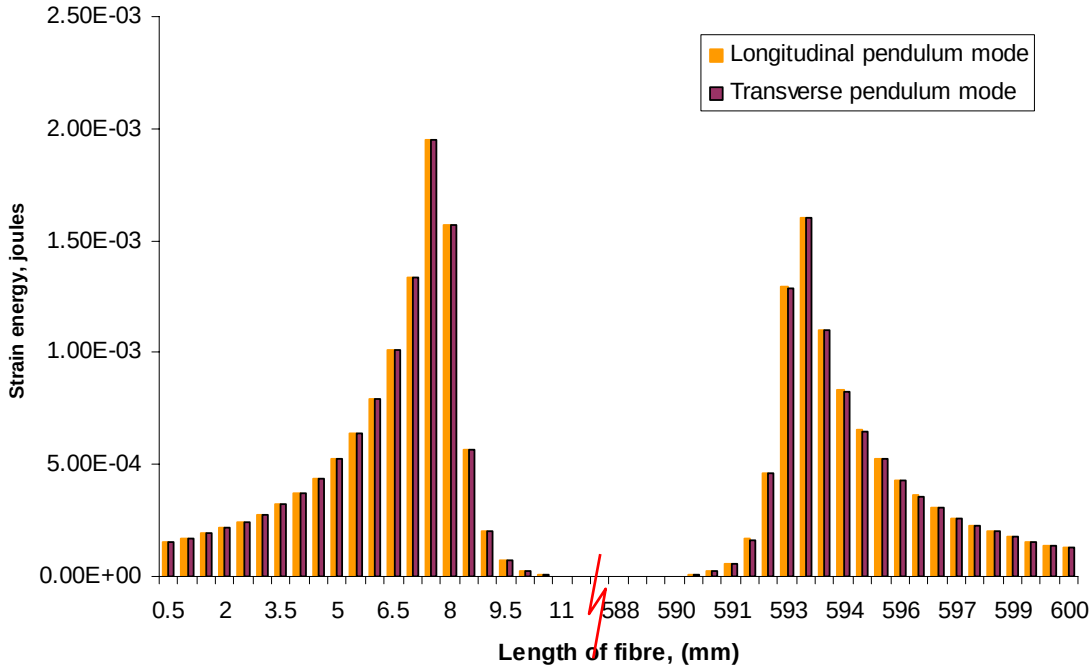

Figure 5.15. Graph showing strain energy distribution in the tapered (7.5 mm) fibres, whose flexure point is at the centre of gravity of the mass. The bar in violet stands for transverse pendulum mode, orange bar is for longitudinal pendulum mode.

Table 5.5 shows the mode frequencies for the case of uniform and linearly tapered two fibres pendulum systems (Note: - the longitudinal pitch mode has zero frequency because the centre of mass is coincident with the flexure point of the fibre).

Case for the pendulum system	Longitudinal pendulum mode (Hz)	Transverse pendulum mode (Hz)	Longitudinal pitch mode(Hz)	Transverse pitch mode (Hz)
Uniform fibre	0.644	0.644	0	2.058
Linearly tapered fibre	0.651	0.651	0	2.07

Table 5.5. Mode frequencies for the case of uniform and linearly tapered two fibres pendulum system.

Table 5.6 shows the dilution factor estimated for the longitudinal and transverse pendulum modes, whose flexure points are positioned at the centre of mass of a 20 kg pendulum system. For the case of the uniform fibre pendulum system, the value of the dilution factor for the longitudinal and transverse pendulum modes are similar, unlike in the earlier case.

For the linearly tapered fibre pendulum system the dilution factor drops by 32 % approximately, however both the pendulum modes (longitudinal and transverse) give similar results.

These results indicate that the relative positioning of the bending point of the fibre and the centre of mass of the pendulum system is very important for achieving the desired results.

Cross section area of fibre	Pendulum mode	Dilution factor (ANSYS)	Dilution factor (Theory)
Uniform fibres	Longitudinal pendulum mode	617	625
	Transverse pendulum mode	616	625
Linear Taper (7.5 mm) fibres	Longitudinal pendulum mode	415	625
	Transverse pendulum mode	414	625

Table 5.6. Dilution factor calculated from ANSYS and compared with theory for two fibres (uniform & tapered ones) for both longitudinal and transverse pendulum mode, whose flexure point is positioned at the centre of mass of a 20 kg pendulum system.

5.5 Conclusions

As discussed earlier, the two-fibre pendulum model is a step between the single fibre pendulum design and that of the Advanced LIGO suspension system. The method used to obtain results in this chapter is consistent with that of chapter 4 and has been successfully applied. Unexpected reductions in dilution factor were observed due to coupling of pendulum and pitch modes. To a large extent this coupling effect can be removed by careful mechanical design and indeed this is an issue which has received significant attention in the suspension design for the current and future gravitational wave detectors.

The method of estimating dilution factor and obtaining the strain energy distribution in the fibres can be further extended to study the suspension system of the Advanced LIGO detectors. This will greatly help in optimising the designs of future detectors (such as Advanced LIGO) to lower their suspension thermal noise.

Chapter 6

Advanced LIGO suspension system

6.1 Introduction

The design of the *Advanced LIGO* (Laser Interferometer Gravitational Wave Observatory) suspension system is based on the *German British GEO 600* detector [56]. The current suspension system used in LIGO consists of test masses hung as single pendulums on wire slings. However the Advanced LIGO detector has more stringent noise level targets to achieve. Hence suspension technology from the GEO 600 detector has been further developed in-order to meet the demands of Advanced LIGO [57].

The target of the Advanced LIGO suspension system is to have a displacement sensitivity of 10^{-19} m/√Hz at 10 Hz at each of the main mirrors [57]. The main mirror suspension for Advanced LIGO is designed as a quadruple pendulum having a monolithic silica final stage. The design requirements are as follows [58; 56; 43]:

- The horizontal thermal noise should be 10^{-19} m/√Hz or lower at 10 Hz, per test mass.
- Technical noise sources should be 10^{-20} m/√Hz or lower at 10 Hz.
- The vertical mode frequency could be 12 Hz or lower and the roll mode is expected to be 1.4 times higher.

- The fundamental violin mode frequency should be 400 Hz or higher.

The work in this chapter analyses the suspension system of the advanced LIGO detector for the estimation of strain energy distribution and dissipation dilution factor. This required an ANSYS® model of the suspension system to be constructed where the performance of fibres and ribbons of uniform cross sectional area was first studied. The consequences of the introduction of tapered necks in the suspension elements are also covered in this chapter.

6.2 Mechanical design of the suspension system

The suspension design planned for use in the Advanced LIGO detector system consists of a quadruple pendulum hung on steel wires and silica fibres or ribbons as shown in figure 6.1 [59]. The upper mass is suspended from two cantilever-mounted trapezoidal pre-curved 'spring blades' (from Marvel 18 (18 % Ni) Maraging steel) and two spring steel wires. Once the blade is loaded it lies horizontally. The mass below this is the upper intermediate mass and is suspended from two blades and two steel wire loops. The upper mass and the upper intermediate mass have a sandwich-type construction and the blades lie in between. This enables the break off points of the wires, which are going upwards and downwards, to lie close to the centre of gravity of these masses. Below the "upper intermediate mass" lies the penultimate mass which is made of fused silica. The penultimate mass is suspended from two cantilever blades and two steel wire loops from the upper intermediate mass. The penultimate mass has flat surfaces on its sides where silica ears are bonded. The ears are fused to four silica fibres or ribbons which suspend the final lowermost mass called the test mass [60]. The test mass has silica ears bonded to flats for attachment to the suspension fibres or ribbons.

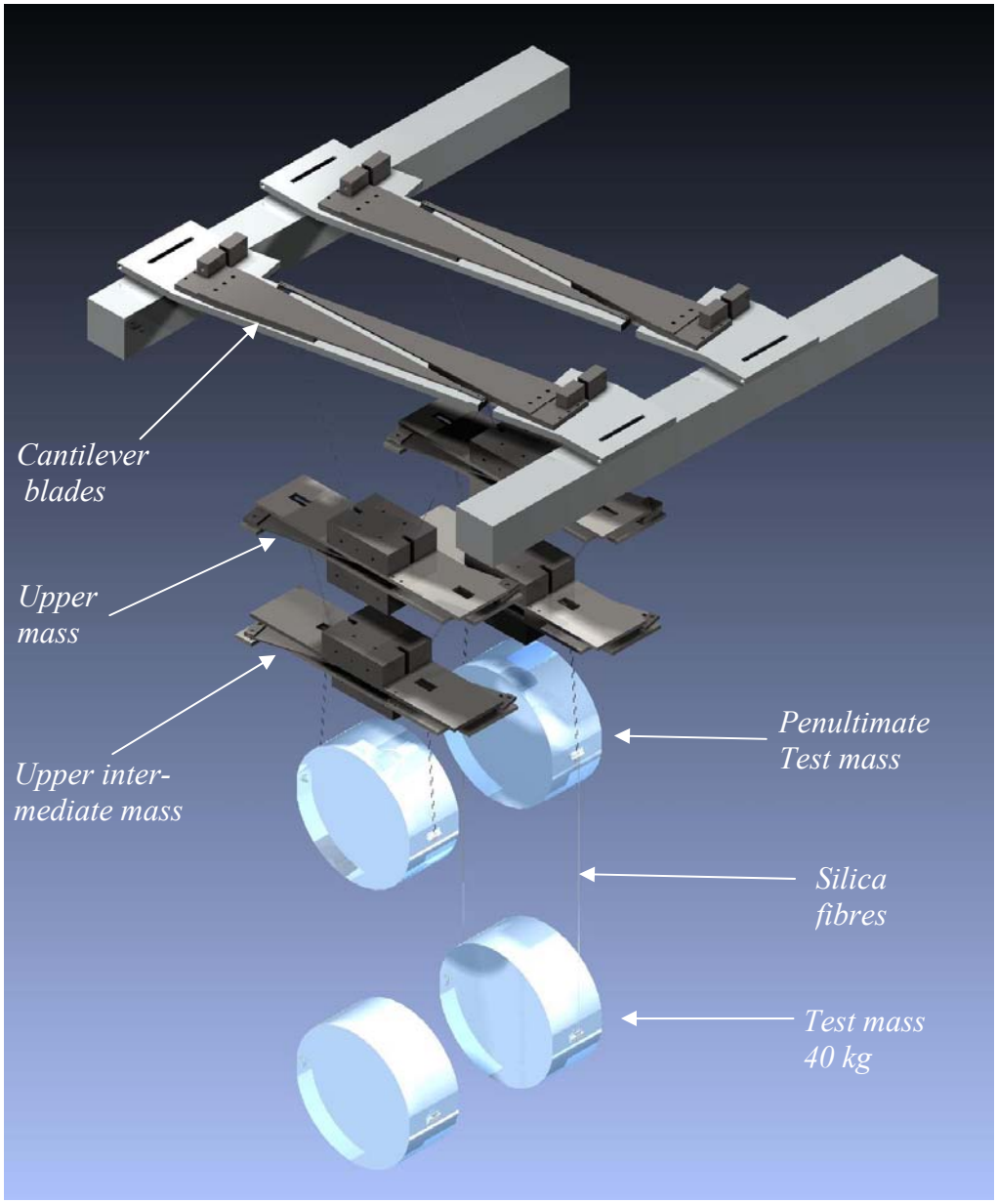

Figure 6.1. Advanced LIGO quadruple pendulum suspension system, designed in auto CAD.(C. Torrie, R. Jones)

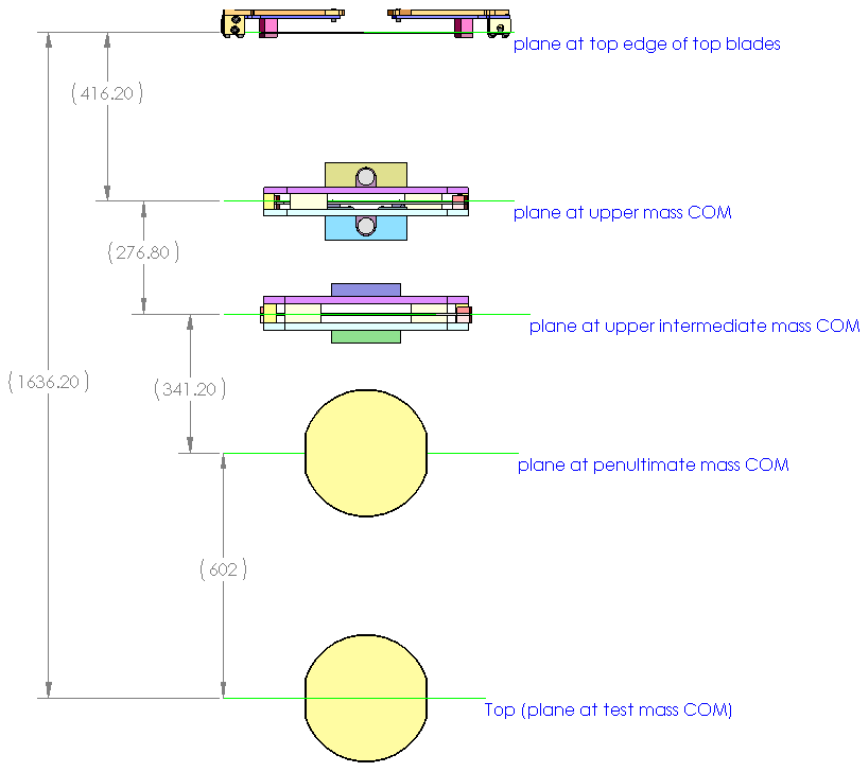

Figure 6.2. Schematic of Advanced LIGO suspension showing the layout of the pendulum system (figures in mm). (C. Torrie)

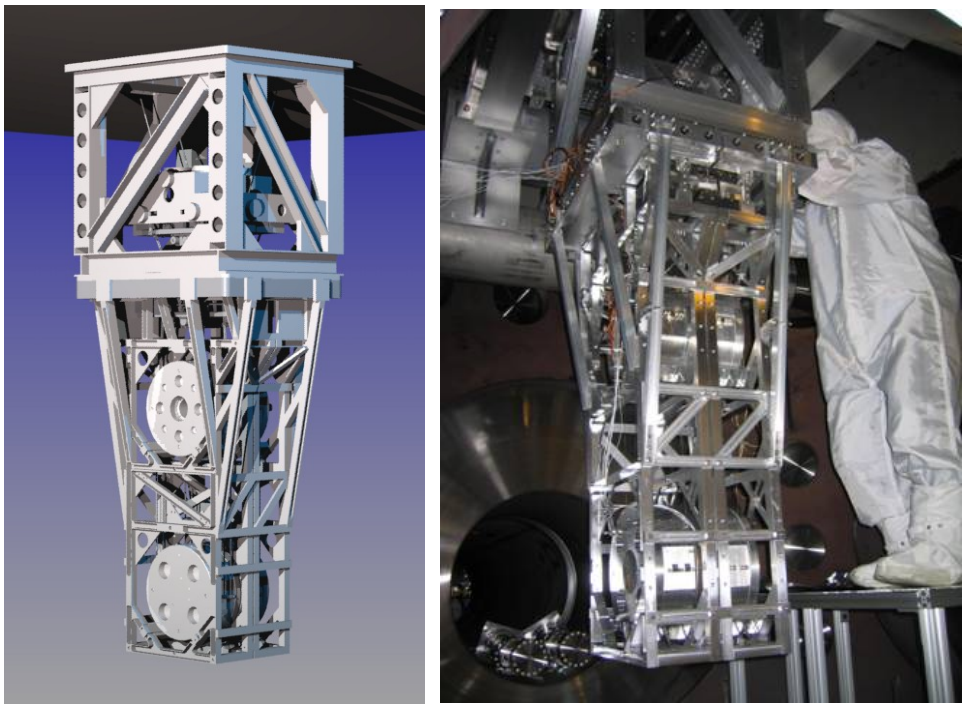

Figure 6.3. Left: - CAD model of the advanced LIGO monolithic suspension system. Right: - All metal prototypes built in MIT-Caltech.

Figure 6.2 shows the layout of the advanced LIGO suspension design. An auto CAD model of the monolithic suspension is shown in figure 6.3 (left hand side). Based on the CAD design an all metal prototype was built in MIT-Caltech (figure 6.3 - on the right side*)*.

6.2.1 Monolithic final stage of the suspensions

Figure 6.4 [59] shows a computer aided design of the final stage of the suspension system. To keep the vertical bounce frequency of the monolithic suspension low several considerations have been made with respect to the suspension fibres or ribbons and the mass. The length of the fibre or ribbon is chosen to be as long as possible while ensuring that the violin modes are high enough for control purpose. The cross sections of the fibre and ribbon are chosen to be as small as practicable and consistent with working at least a factor of 3 away from the breaking stress [56].

Taking into account all the design requirements the diameter of the silica fibre was taken as 0.4 mm (400 micron) and cross section of the silica ribbon as 1.1 mm by 0.11 mm and their length as 600 mm [58; 56].

Test and penultimate masses

Each test mass for the Advanced LIGO final stage suspensions weigh 39.6 kg[56]. The diameter of each mass is 340 mm and the thickness is 200 mm. The test mass material was chosen to be silica Heraeus suprasil 312, having a density of 2202 kg/m^3 [61]. This was a result of this material having a suitable combination of properties, including low optical

loss. The test mass has flats measuring 95 mm by 200 mm on either sides, to allow the attachment, by silicate bonding of the ears to which the suspension fibres are attached [62]. The dimensions of the penultimate masses are same as those of the test masses [60].

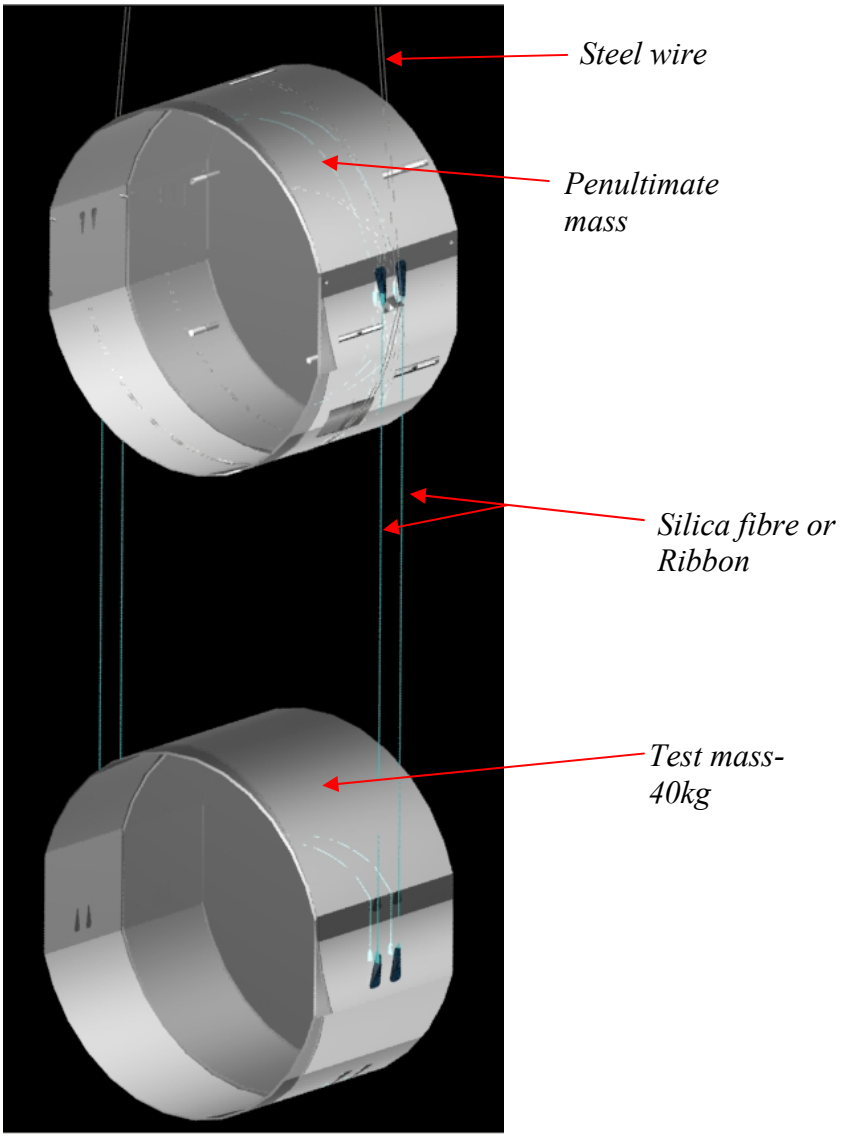

Figure 6.4. CAD® design of the quasi monolithic silica lower stage of the advanced LIGO suspension. The penultimate mass is suspended by steel wire loops from a metal base above. The test mass is suspended using silica fibres or ribbons. Ears act as an interface between fibres and masses.(C. Torrie, R. Jones)

Ear arrangement on the penultimate mass

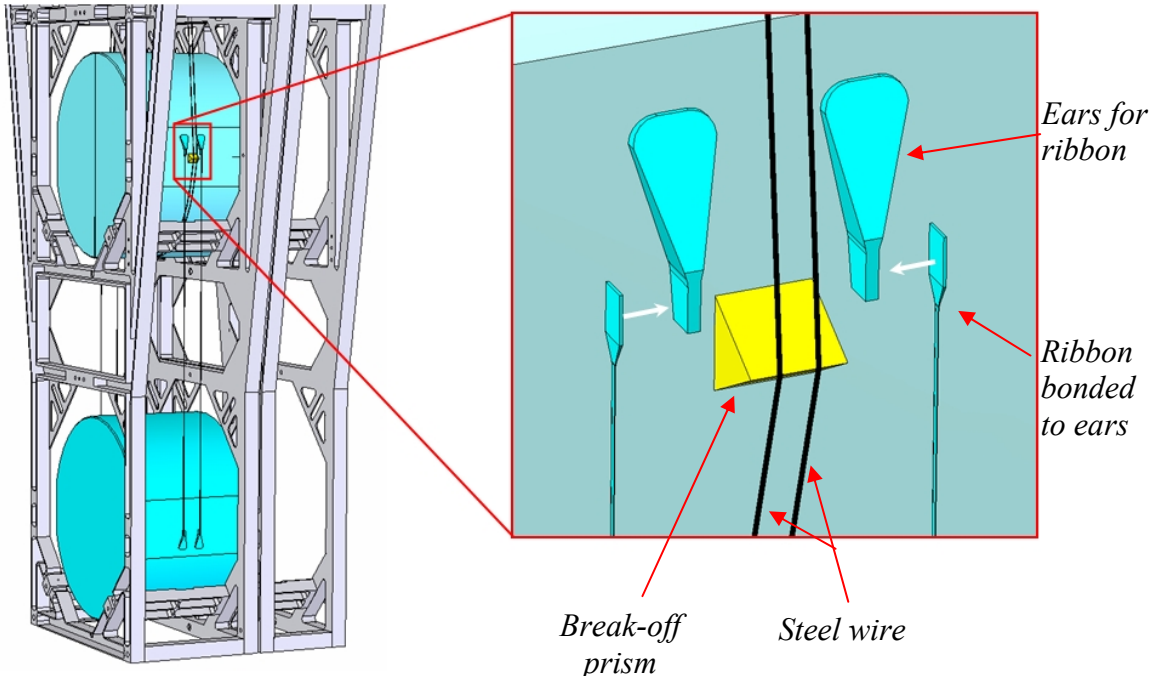

Figure 6.5. CAD® design of the ears, break-off prism and ribbon assembly on the flat surface of the penultimate mass in the advanced LIGO monolithic stage. (C. Torrie, R. Jones)

The CAD design in figure 6.5 shows the arrangement of the ears and in this example ribbons on the penultimate mass. The ears are bonded to the flat surface of the penultimate mass [63]. The current design incorporates ribbons which are laser welded to the lateral side of the ears as shown in the figure above. Also seen is the break off prism for the steel wire loops which suspend the penultimate mass [60].

Ribbons and fibres

A major issue with Advanced LIGO is to reduce the pendulum thermal noise; thus the current baseline design incorporates ribbons for suspension of the test mass [64]. This is

because ribbons have some apparent advantage over the cylindrical fibres [65; 66; 67; 68]. One of the biggest benefits of using uniform ribbons (of uniform cross section area) is their high dilution factor [48]. However it has become clear from the previous chapter that the dilution factor can be significantly reduced by having tapered ends on the fibres or ribbons.

In this chapter the effects of the taper for both idealised and real experimental cases will be evaluated for the Advanced LIGO suspension design.

6.3 F. E Analysis of the Advanced LIGO silica suspension system

Finite element (F. E) analysis of the Advanced LIGO suspension will help in solving some of the issues which has been discussed in the earlier section.

The final stage of the Advanced LIGO suspension system was modelled in ANSYS® using silica fibres and ribbons initially of uniform cross section. Necks were then added to the suspension wires. Realistic tapered fibres and ribbons were then fabricated in the laboratory using a laser pulling machine. The work on ribbons was done by Alan Cumming [1] and the fibres of circular cross section were studied by the author. Finally the results were compared and analysed.

The F. E analysis was mainly used to estimate the distribution of energy in the fibres and ribbons and using this the dissipation dilution factor for the Advanced LIGO suspesnion system was calculated. These results can then be used to optimize the current baseline design to improve its performance with respect to the thermal noise in the suspension system.

6.3.1 ANSYS® model of Advanced LIGO suspension system, employing fibres or ribbons of uniform cross section

The Advanced LIGO final suspension system was designed in ANSYS® as shown in figure 6.6. The design consists of four silica fibres of uniform cross section area suspending a silica test mass weighing 40 kg [57; 56; 60]. The material properties of the silica were taken as; density ~ 2202 kg/m^3, Young's modulus ~ 7.2×10^{10} Nm^{-2} and Poisson's ratio ~ 0.17. The fibres of circular cross section are 600 mm long and 0.4 mm in diameter. Ribbons investigated by Alan Cumming [1] are of length - 600 mm and cross section area: 1.1 mm by 0.11 mm.

The ear design was kept simple in this model, being a rectangular prism of length ~ 40 mm, breadth ~ 5 mm and height ~ 15 mm. The more complicated ears, as suggested in the LIGO documents were avoided as the focus of our investigation is the comparison of the performance on fibres and ribbons initially. The final design of the ears for Advanced LIGO suspension has still to be carried out and will be informed by the work reported here. Hence simple ears were used to allow comparison between cylindrical fibres and ribbons.

Each ear accommodates two fibres or ribbons having a separation of 3 mm. The fibres or ribbons are attached to the top surface of the ears as seen in the enlarged section of figure 6.6. The bending length of the fibre used in this model is approximately 0.96 mm and for the ribbon it is 0.43 mm. This was calculated in ANSYS® and verified analytically (discussed in chapter 4).

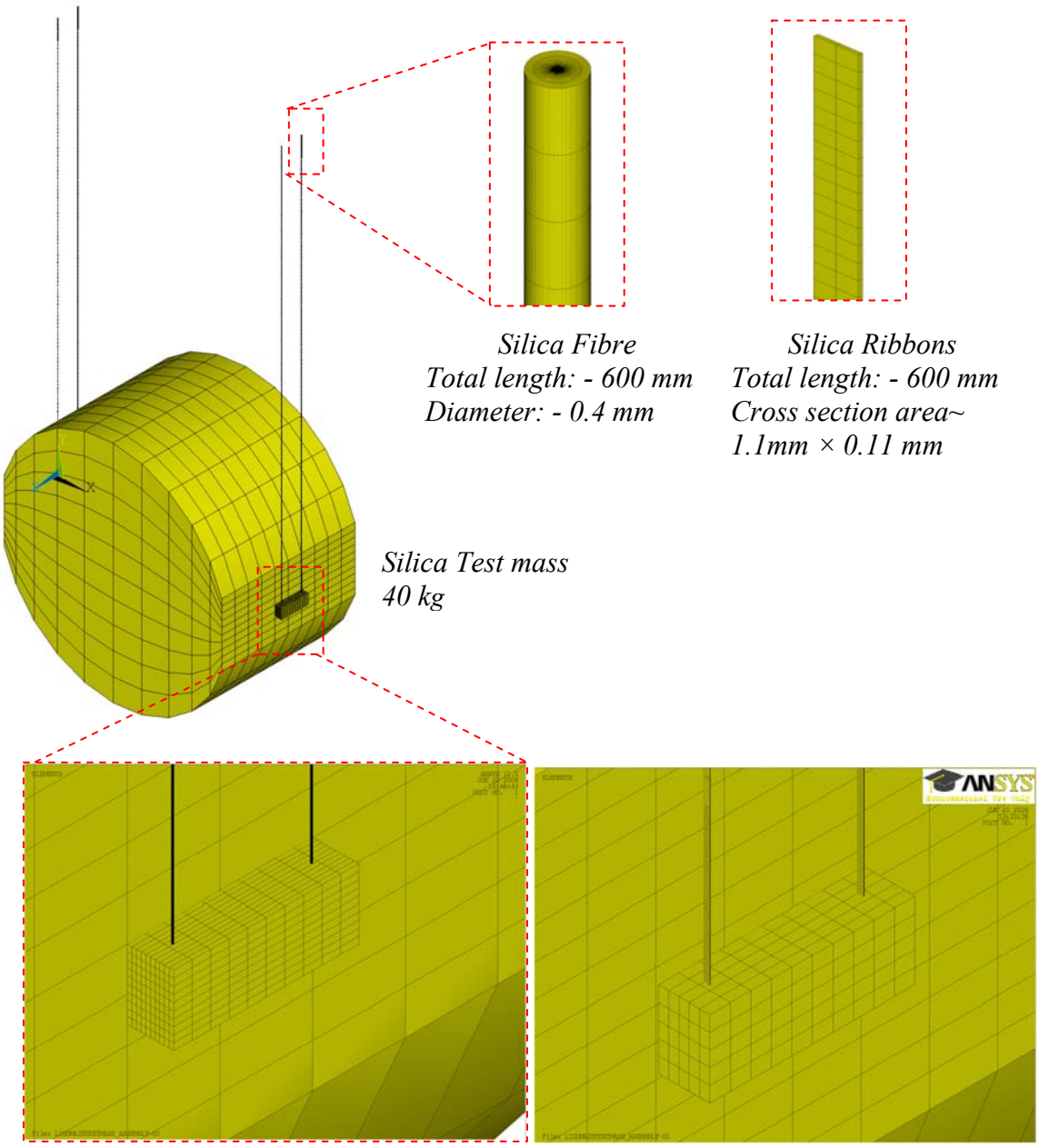

Figure 6.6. Advanced LIGO suspension design using four silica fibres bonded to ears, suspending a mass of 40 kg. Ribbons designed by [1] are shown for comparison with fibres.

The position of the ears on the test mass should be such that the flexure point of the fibre is 1 mm above the *"centre of gravity"* of the test mass. This is a design requirement of the Advanced LIGO final suspension system which helps to keep the mass stable.

Then the free ends of all four fibres or ribbons were clamped for six degree of freedom, three directional and three rotational. The design was subjected to loading condition like gravity before solving it for '*static structural'* and then '*modal dynamic'* analysis.

Table 6.1 shows the mode frequencies for the Advanced LIGO suspension system, obtained using ANSYS® and calculated analytically. The mode frequencies agree to within 1%, thus indicating that the ANSYS® models are functioning properly. The frequencies were identified by inspection of their mode shapes in ANSYS®. The bounce mode frequency is well within 10 Hz and the first violin mode is above 400 Hz, as required by the design specification of Advanced LIGO.

Mode shape (ANSYS)	**Mode frequency (ANSYS)**	**Mode frequency (Theory)**
Longitudinal pendulum	0.644	0.643
Transverse pendulum	0.645	0.644
pitch	0.921	0.915
Yaw	1.067	1.068
Bounce	6.241	6.181
Roll	8.759	8.743
First Violin	495.46	497.791

Table 6.1. Frequencies of the resonant modes for the Advanced LIGO suspension system, having uniform fibres.

The longitudinal pendulum mode of vibration is studied in the next section.

6.3.1.1 Analysis of longitudinal pendulum mode of vibration

The thermal noise associated with the pendulum mode of the suspensions is one of the sources of noise in the Advanced LIGO detector. Figure 6.7(a) shows the deformed and un-deformed mode shape of the longitudinal pendulum mode. The stress due to bending in the suspension elements is shown by the contours in figure 6.7(b). As expected the fibres or ribbons bend close to the very top of their mounting points which causes maximum stress close to those points (shown in red colour in the figure 6.7b). However the fibres or ribbons here also bend from the bottom portion, similar to that of the top portion.

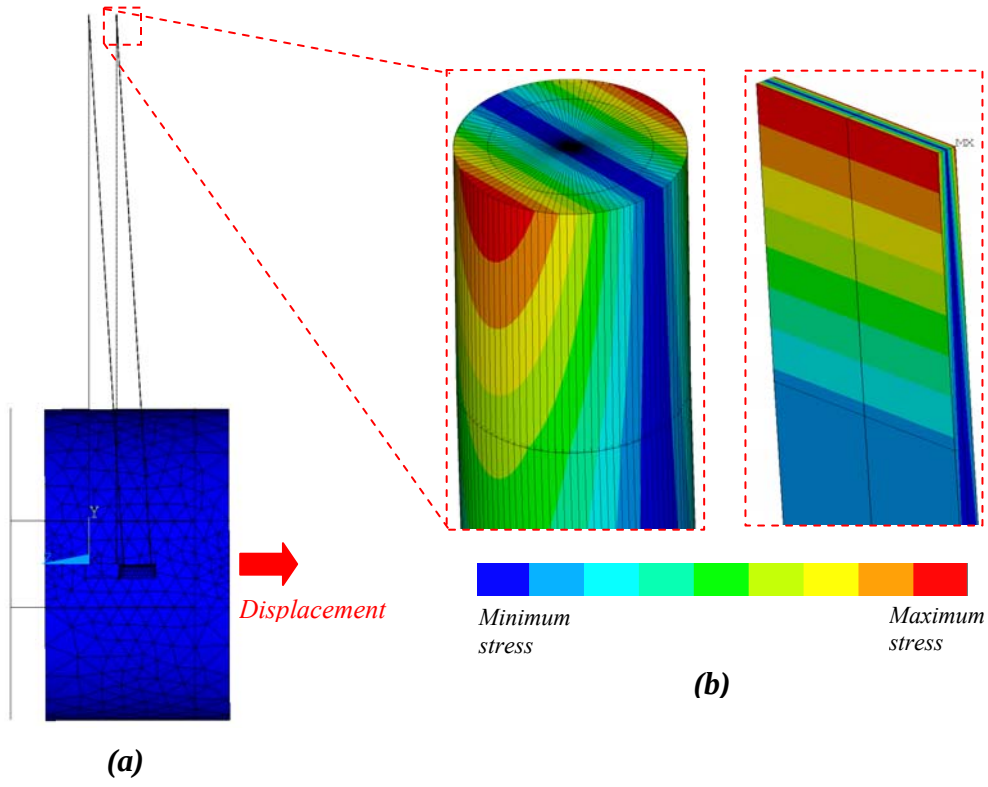

Figure 6.7. (a) Deformed mode shape of the longitudinal pendulum mode of an advanced LIGO suspension.
(b) Stress plot of a cylindrical fibre (left) and ribbon (right) due to bending.

In figure 6.8 the distribution of strain energy as a function of length of the suspension elements is plotted. Fibres are represented by red bars and blue indicates ribbon. The plot suggests as expected that the fibre and ribbons are bending predominantly at the top and bottom. The middle section (from 4 mm till 596 mm) contains a negligible amount of energy. Strain energy in the fibres can be seen as far as approximately 3.5 mm from the top and bottom, whereas for the ribbons the energy is contained in the 1st mm. As discussed in the earlier chapters, this is because the fibres have greater bending length due to their higher stiffness.

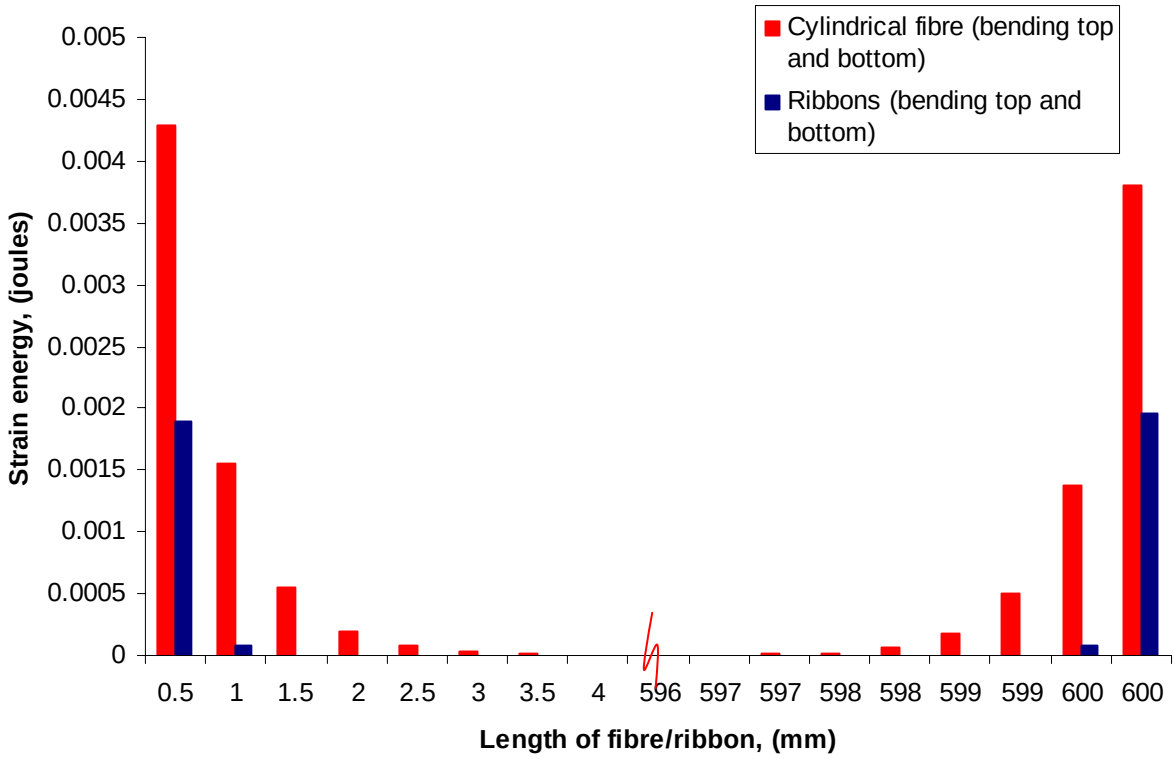

Figure 6.8. Strain energy distribution in the uniform fibre and ribbon of advanced LIGO suspension. The red bars represents cylindrical fibres. The blue bar represents the ribbon which was calculated by Alan Cumming. Both the wires are seen bending at its top and bottom cross section.

Advanced LIGO suspension Design (silica fibre/ribbon)	Dilution factor (ANSYS®)	Dilution factor (Theory)
Fibre	646	625
Ribbon	2040	2048

Table 6.2. Comparison of dilution factor for the advanced LIGO suspension model having silica fibre or silica ribbon as its suspension wires; Calculated for the longitudinal pendulum mode of vibration.

The dilution factor for the advanced LIGO suspension system was estimated from ANSYS® and then compared with the theory as described previously and the results are as expected.

Shown in table 6.2, the dilution factor estimated from ANSYS® and analytically agrees to within 3% for the fibres and within 1% for the ribbons case.

It can also be seen that in theory the dilution factor for a suspension using ribbons is higher than the fibres. It is greater by a factor of 3 and is why it was originally favoured for the baseline design of the advanced LIGO suspension. However a real system will employ suspension elements whose cross sectional area varies and it was seen in earlier chapters that this can significantly affect the dilution factor achievable. The consequences of this for the Advanced LIGO suspension design are discussed in the next section.

6.3.2 Study of linearly tapered necks in the fibres and ribbons of the Advanced LIGO suspension system

The fibres or ribbons to be used in the real suspension require neck at the ends for welding purpose. Initially to represent this type of design, simple linear tapered necks were introduced in the fibre or ribbon. An ANSYS® model of fibres having linear tapered necks at their ends is shown in figure 6.9.

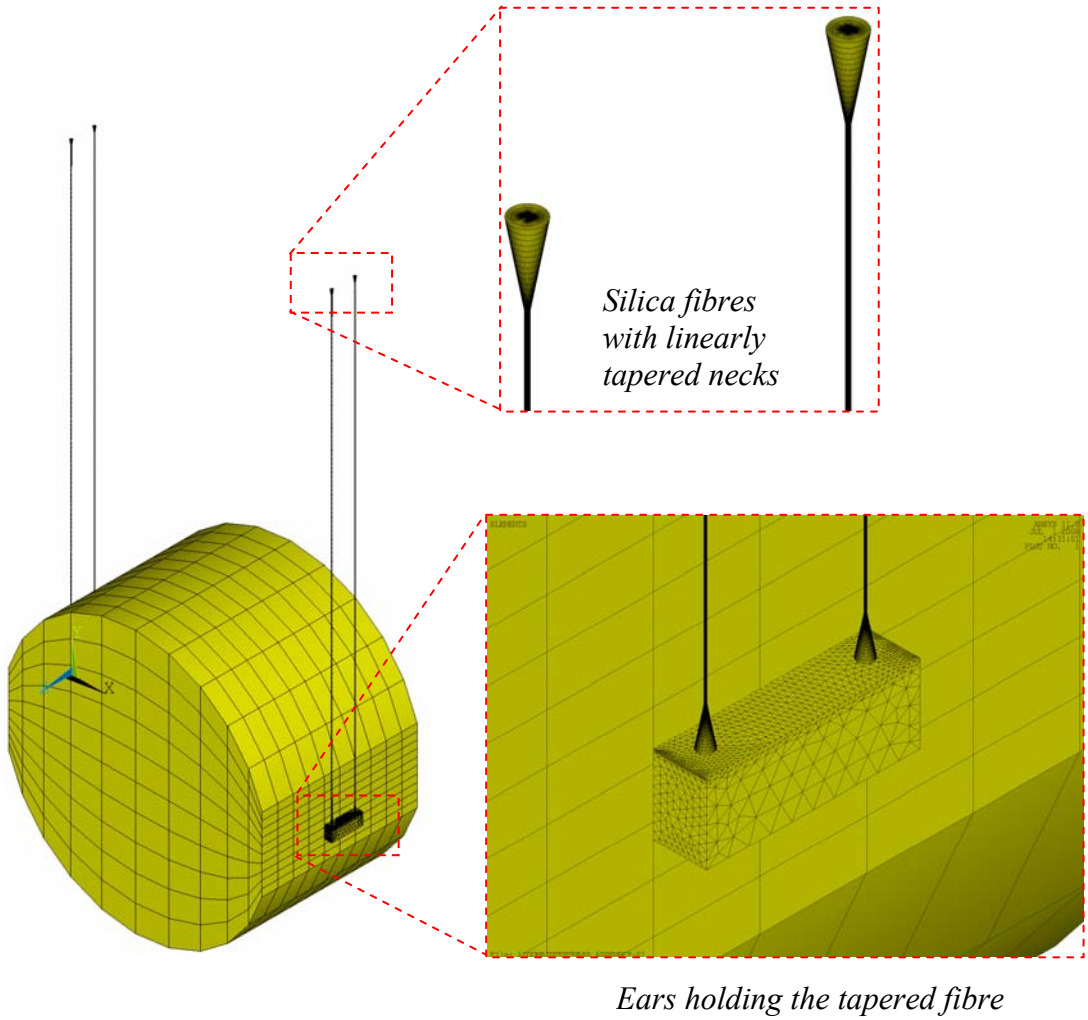

Figure 6.9. ANSYS® model of Advanced LIGO suspension system, built using silica fibres having linear tapered neck at the ends.

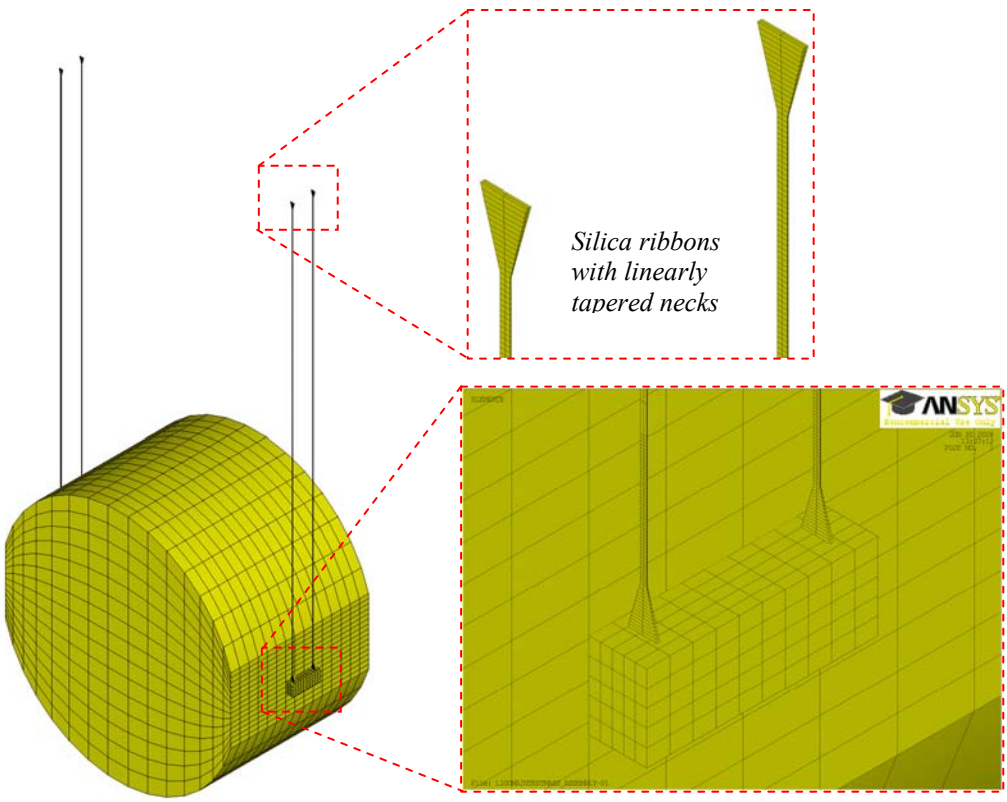

Figure 6.10. ANSYS® model of Advanced LIGO suspension system, constructed by [1] using silica ribbons having linear tapered neck at the ends.

A similar model was constructed by [1] in ANSYS® using ribbons and is shown in figure 6.10. The consequence of introducing necks in the fibre or ribbons in the advanced LIGO suspension was then studied.

6.3.2.1 Design and types of 'necks' in the fibre or ribbon

The neck design modelled in ANSYS® is a simple representation of the real ones, as shown in figure 6.11. The starting cross section area of the neck is 3 mm which tapers down till it merges into the diameter of the fibre. The neck for the ribbons starts at 5 mm wide and ends at 1.1 mm. The necks were studied for two given lengths, 7.5 mm and 15 mm respectively.

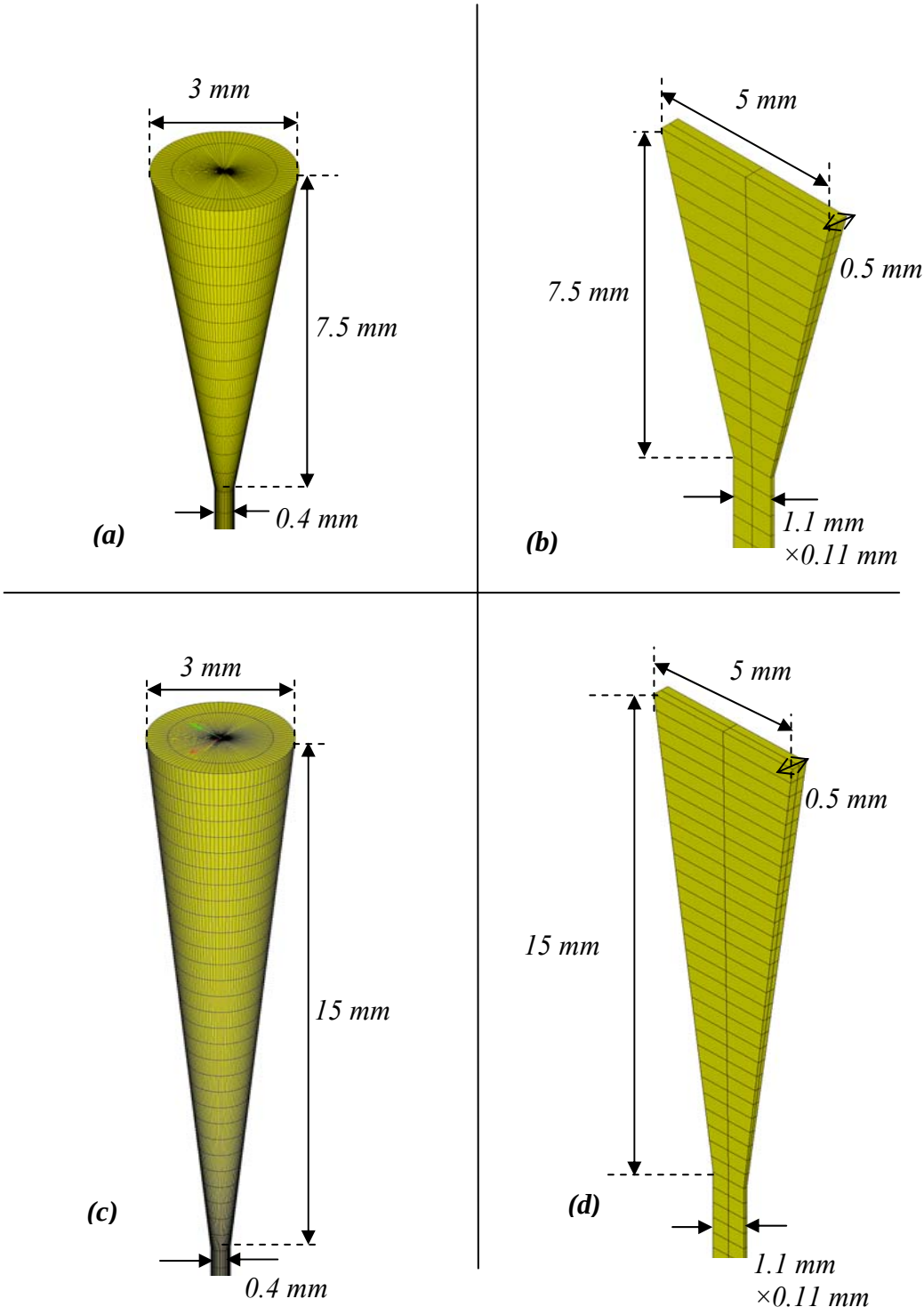

Figure 6.11. ANSYS® model of tapered neck used in the fibres or ribbons of the advanced LIGO suspension wires. (a) 7.5 mm long linear tapered neck for fibre (b) 7.5 mm long linear tapered neck for ribbon (c) 15 mm long linear tapered neck for fibre (d) 15 mm long linear tapered neck for ribbon.

6.3.2.2 Analysis of tapered fibres or ribbons in the Advanced LIGO model (for the longitudinal pendulum mode)

The flexure point and the stress distribution in the linearly tapered fibres and ribbons of the Advanced LIGO suspension system are similar to those discussed in chapter 4 (single fibre pendulum case) as both employ fibres and ribbons of same dimension. However in this case there is bending at the bottom of the element as well as at the top.

Figure 6.3 shows the value of the bending length estimated from ANSYS® for the linearly tapered fibre and ribbon of the Advanced LIGO suspension system.

Type of the neck used in fibre/ribbon	Bending length (ANSYS®), mm
7.5 mm linear tapered fibre	8.02
15 mm linear tapered fibre	13.47
7.5 mm linear tapered ribbon	3.766
15 mm linear tapered ribbon	4.89

Table 6.3. Bending length value (calculated from ANSYS®) of the tapered fibres and ribbon used in ANSYS model of advanced LIGO suspension design.

The stress distribution at the top of the fibre and ribbon of the Advanced LIGO suspension is shown in figure 6.12. A similar distribution is obtained at the bottom.

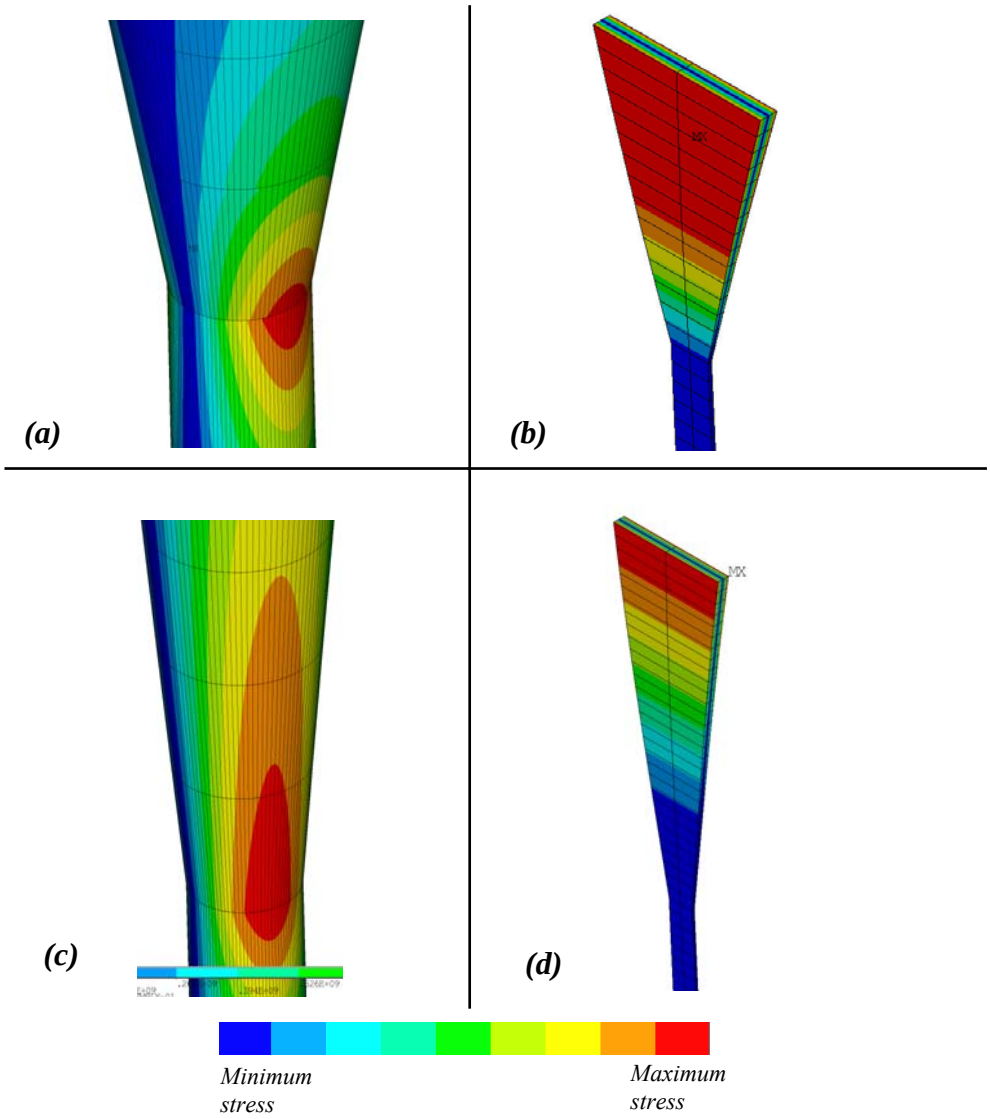

Figure 6.12. Contours showing stress in fibre and ribbons due to bending in the longitudinal pendulum mode. (a) 7.5 mm long linear tapered fibre (b) 7.5 mm long linear tapered ribbon (c) 15 mm long linear tapered fibre (d) 15 mm long linear tapered ribbon.

The graph in figure 6.13 shows the strain energy distribution along the length of the fibre and ribbon for the case of 7.5 mm and 15 mm long tapered sections. For the tapered fibre, the energy slowly increases, reaches a peak and then decreases gradually. The peak is seen at the joint of the tapered section and the uniform fibre. The tapered ribbon stores most of its energy in the tapered region and then decreases gradually. These results are in full agreement with those observed in the previous chapters.

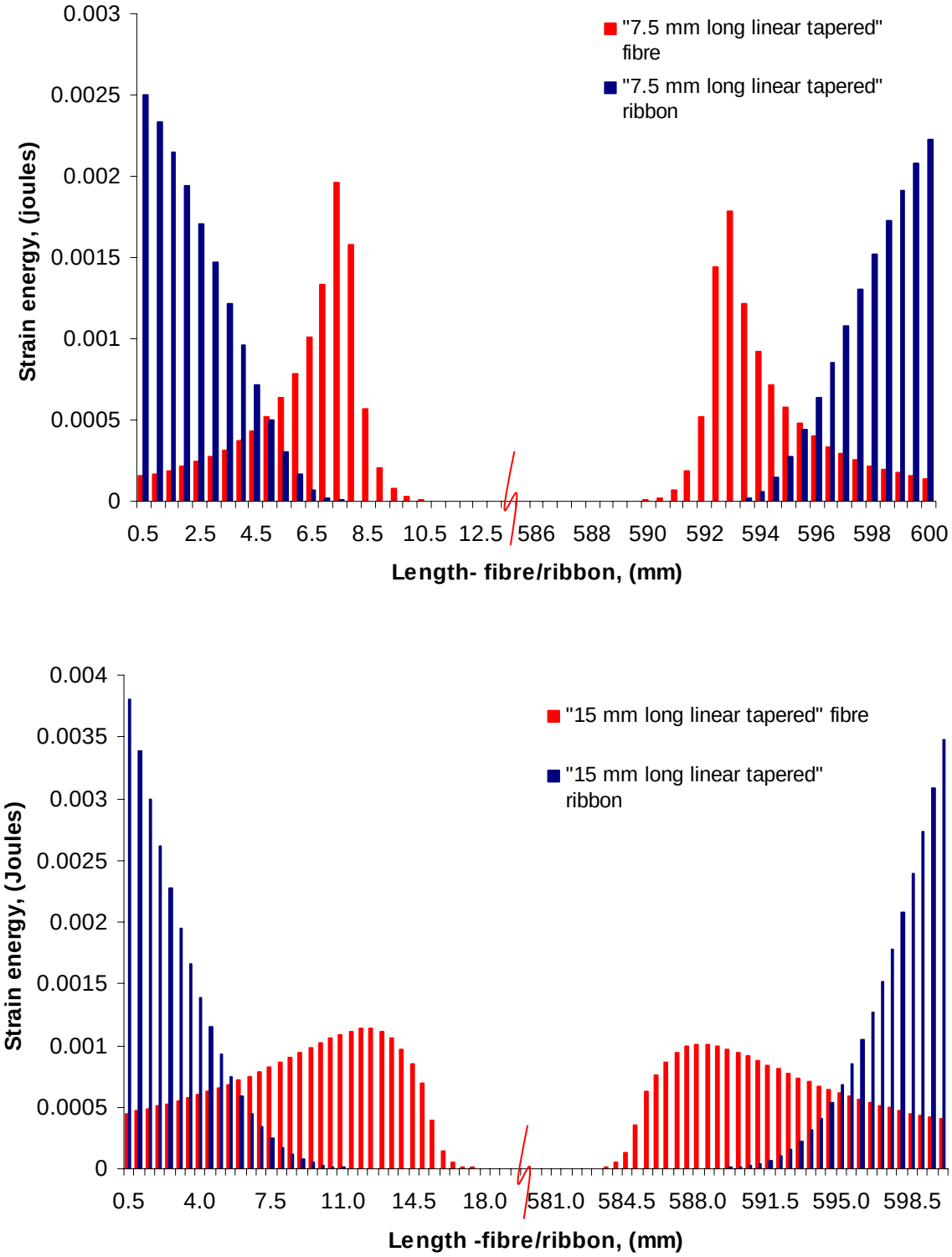

Figure 6.13.
Top: - strain energy distribution in the 7.5 mm linear tapered fibre/ribbon used in ANSYS® model of advanced LIGO suspension.
Bottom: - strain energy distribution in the 15 mm linear tapered fibre/ribbon used in ANSYS ® model of advanced LIGO suspension.

As observed in earlier chapters the dilution factor is significantly reduced in the presence of the tapered necks and the effect has been more severe in the case of ribbons than the fibres.

Case (fibre/ribbon)	Dilution Factor (ANSYS®)	Dilution Factor (Theory- no neck case)
linear tapered (neck – 7.5 mm) fibre	396	625
linear tapered (neck-15 mm) fibre	185	625
linear tapered (neck- 7.5 mm)ribbon	273	2048
linear tapered (neck- 15 mm) ribbon	174	2048

Table 6.4. Dilution factor comparison between tapered (7.5 mm/15 mm) fibre and ribbon used in the ANSYS® model of the Advanced LIGO suspension design.

This degradation of the dilution is significant for the design of Advanced LIGO and makes it important to carry out full calculations of the thermal noise expected. This will be addressed in the next chapter. However, before moving to this it is important to examine the dilution factor obtained with realistic fibres and ribbons of dimensions that can be obtained experimentally. This is discussed next.

6.4 F. E analysis of laser pulled fibres for the Advanced LIGO suspension system

6.4.1 Introduction

The fibres studied up to this point had linearly tapered ends. However because of experimental constraints the fibres or ribbons to be used in the advanced LIGO design will have tapers of a curved form. Such fibres or ribbons were fabricated in the laboratory at University of Glasgow. The shapes of these real fibres or ribbons were then incorporated into an ANSYS® model for the Advanced LIGO suspension in order to gauge its performance with respect to strain energy distribution and dilution factor.

6.4.2 Fabrication of tapered fibre from silica rod using CO_2 laser pulling machine

The fibres were fabricated using a CO_2 laser pulling machine set up by A. Heptonstall and G. Hammond at University of Glasgow. The design and set up of the machine is described in [69]. Figure 6.14 shows the picture of the laser pulling machine installed in the laboratory. The configuration shown is for pulling circular fibres from polished silica rods. The CO_2 laser pulling machine can be used to manufacture silica fibres or ribbons with large cross section area at the two extremes which gradually decreases towards the middle.

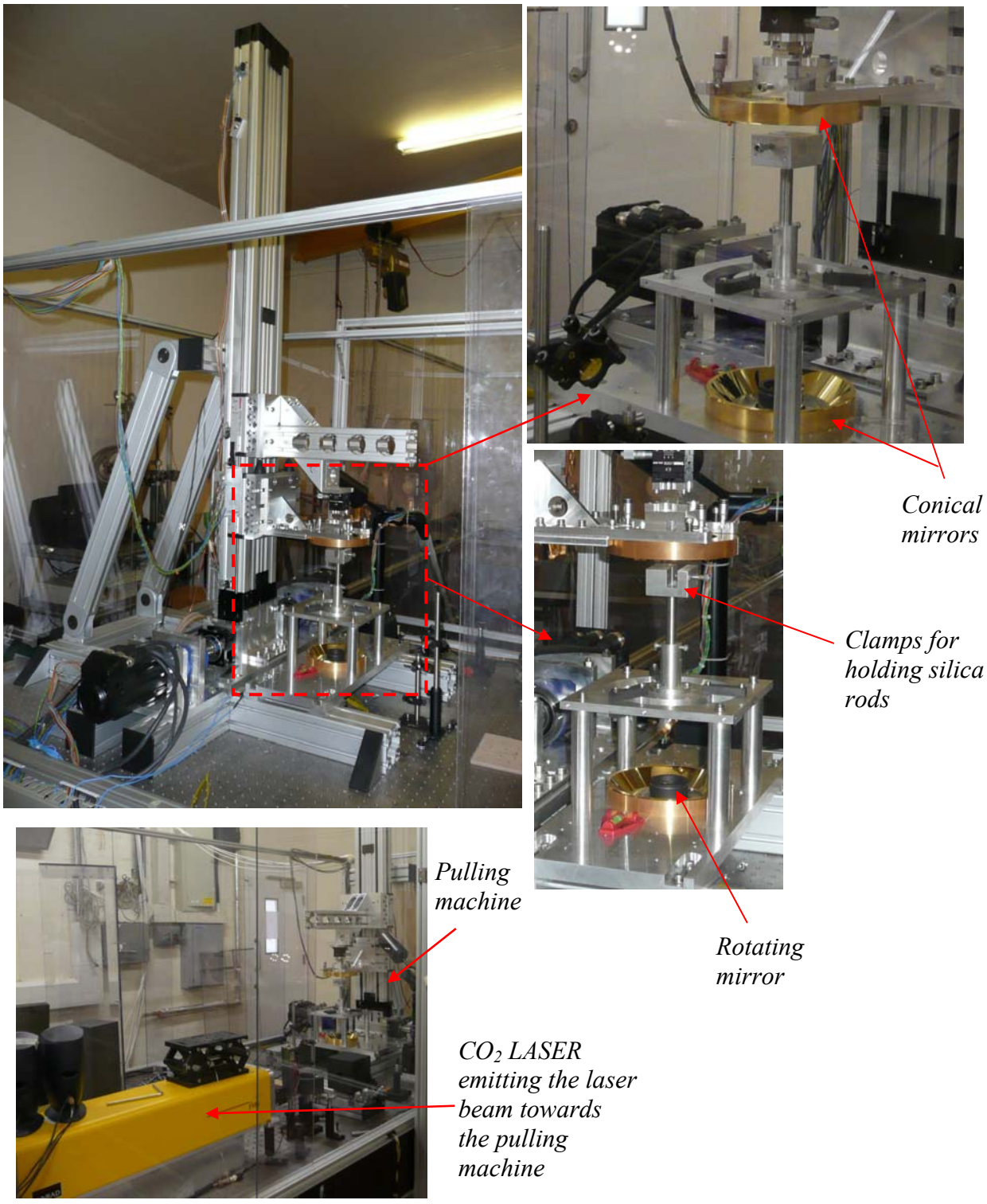

Figure 6.14. Top left- picture of the laser pulling machine set up at University of Glasgow, top right- zoomed image of the pulling machine showing the area where the silica rods are kept and other components of the machine. Bottom left- CO_2 laser installed at the IGR lab. directing laser beams towards the pulling machine.

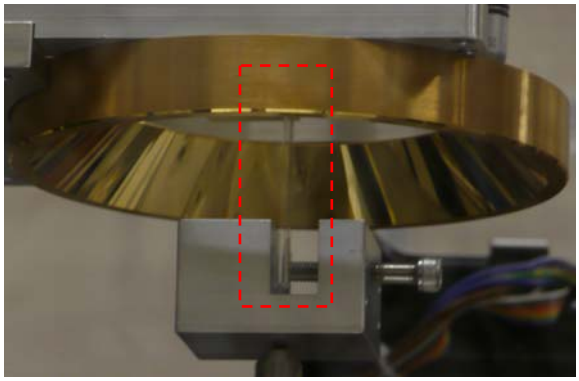

Silica rod of uniform diameter 3 mm, fixed in the pulling machine

Silica rods being heated by the laser beam.

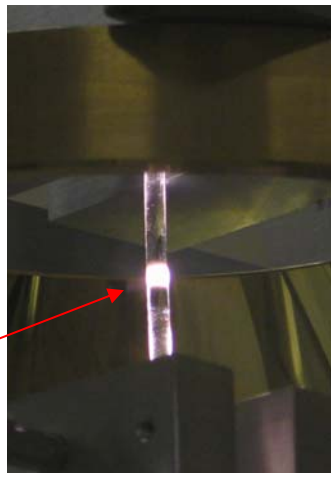

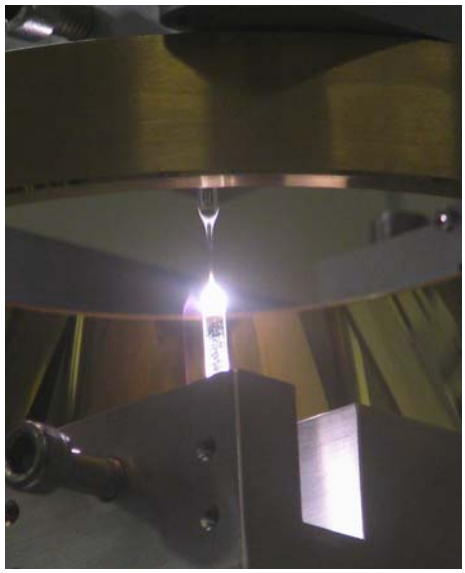

Silica rod begins to be pulled into a thin fibre; necks formed

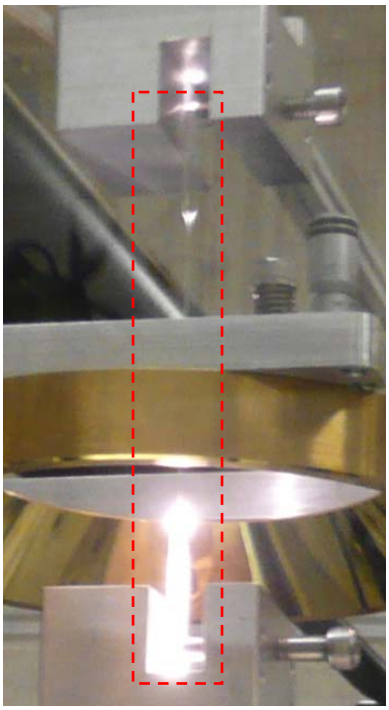

Thin silica fibre (diameter 0.4 mm) can now be seen, being pulled for desired length.

Figure 6 .15. Image showing the fabrication of advanced LIGO cylindrical silica fibre of diameter 0.4 mm and length 60 cm, having small necks at its ends, from silica rod of diameter 3 mm, at University of Glasgow.

Figure 6.15 shows the steps involved in the fabrication of silica fibre from a silica rod. At first a polished silica rod having 3 mm diameter was clamped in the pulling machine. The pulling machine was then programmed (in terms of pulling speed and the rate of feed etc.) such that the fibre is of desired length, diameter and different cross section. The silica rod is now ready to be heated by the CO_2 laser, the hot part being indicated by the bright section on the silica rod in the figure 6.15. Once the rod reaches the desired temperature the motor starts to pull it slowly. At first small necks are created which is seen the third step in the figure and then the motor speed is increased such that the thin uniform section of the fibre is formed.

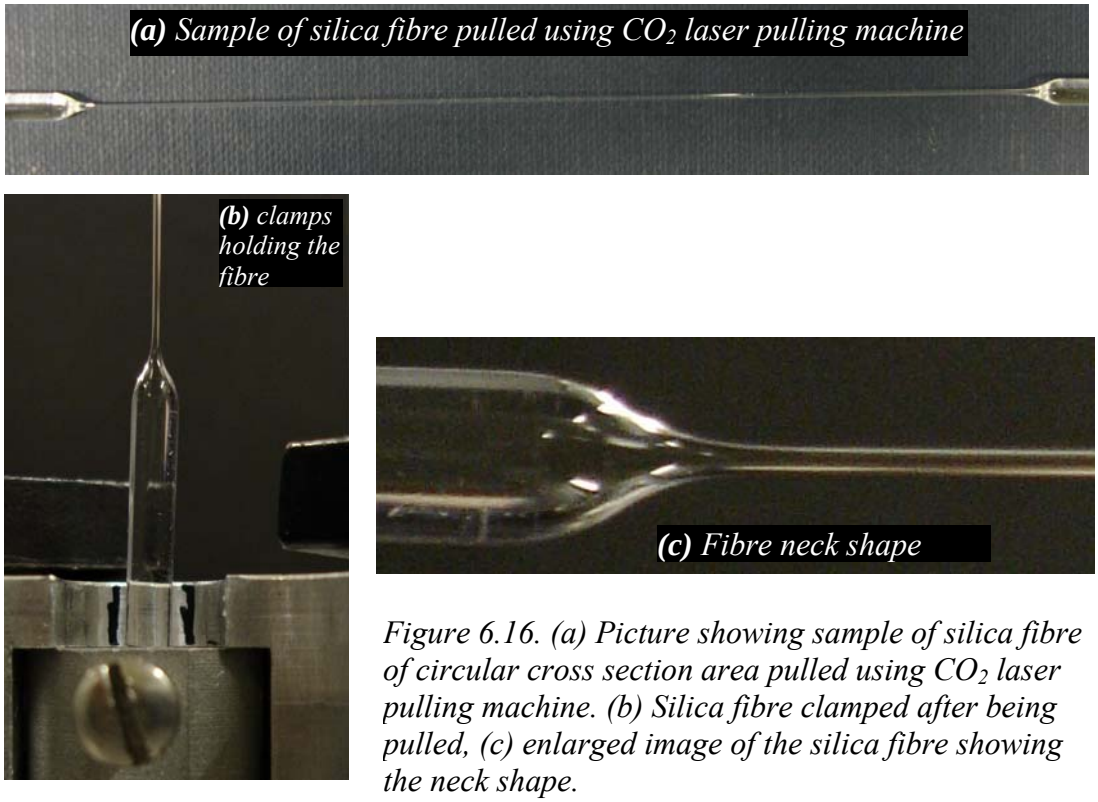

Figure 6.16. (a) Picture showing sample of silica fibre of circular cross section area pulled using CO_2 laser pulling machine. (b) Silica fibre clamped after being pulled, (c) enlarged image of the silica fibre showing the neck shape.

The fibre is then carefully removed from the pulling machine and clamped. Figure 6.14 (a) shows a sample of the silica fibre of circular cross section, fabricated at Glasgow. The starting cross section of the fibre is 3 mm followed by the neck section. The neck gradually decreases and forms the thin cylindrical section of the fibre having an approximate diameter of 0.4 mm. The cylindrical section of the fibre runs for some distance and then gradually starts to increase in diameter to form the other neck. Thus the fibre is dumbbell shaped, having exponential tapers. The shape of the neck can be seen closely in figure 6.16(b). The dimensions of the fibre are then measured.

6.4.3 Characterization of the laser pulled silica fibre

The measurement of the laser pulled silica fibre was done with the help of a fibre profiler. The profiler consists of two orthogonally positioned, high magnification travelling camera systems which scan the entire length of the fibre, allowing measurement of its diameter. The image of the fibre can be seen on a computer screen. The profiler was designed by A. Cumming and the details of the set-up can be found in the literature [1].

As the camera travels along the length of the fibre, the fibre diameter is recorded at regular intervals. The generated data is then imported into Microsoft® excel.

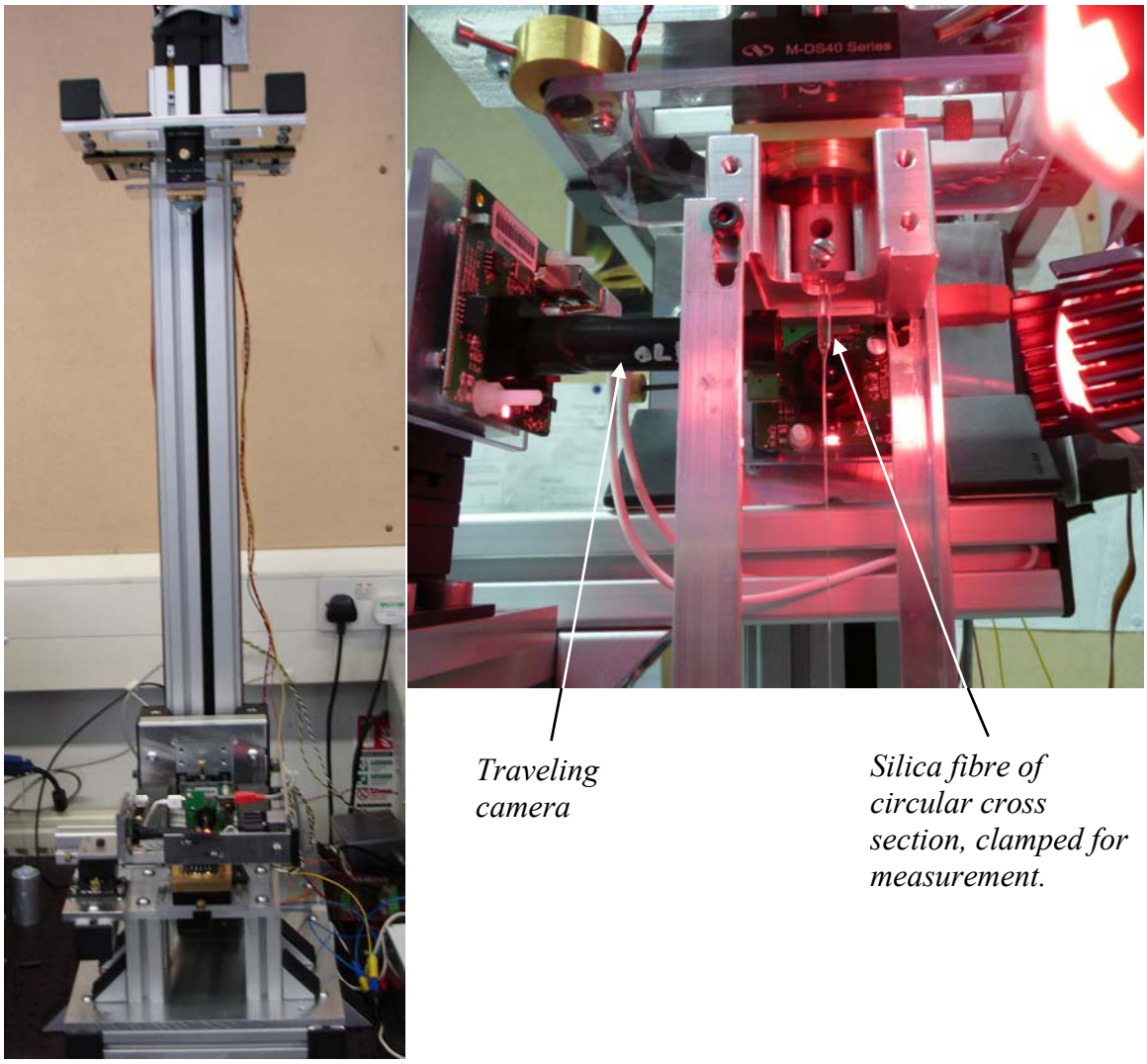

Figure 6.17. Set up of the dimension characterisation machine for profiling of the laser pulled silica fibre, on the right the fibre can be seen, clamped for measurement.

Figure 6.17 shows the dimension characterisation machine used for profiling of the laser pulled silica fibre. The silica fibre can be seen clamped for measurement.

The data obtained from the profiler is then plotted in a graph as shown in figure 6.18. On the graph is plotted the diameter of the fibre against its length. The fibre of circular cross section starts at around 2.8 mm diameter and gradually reduces to 0.4 mm.

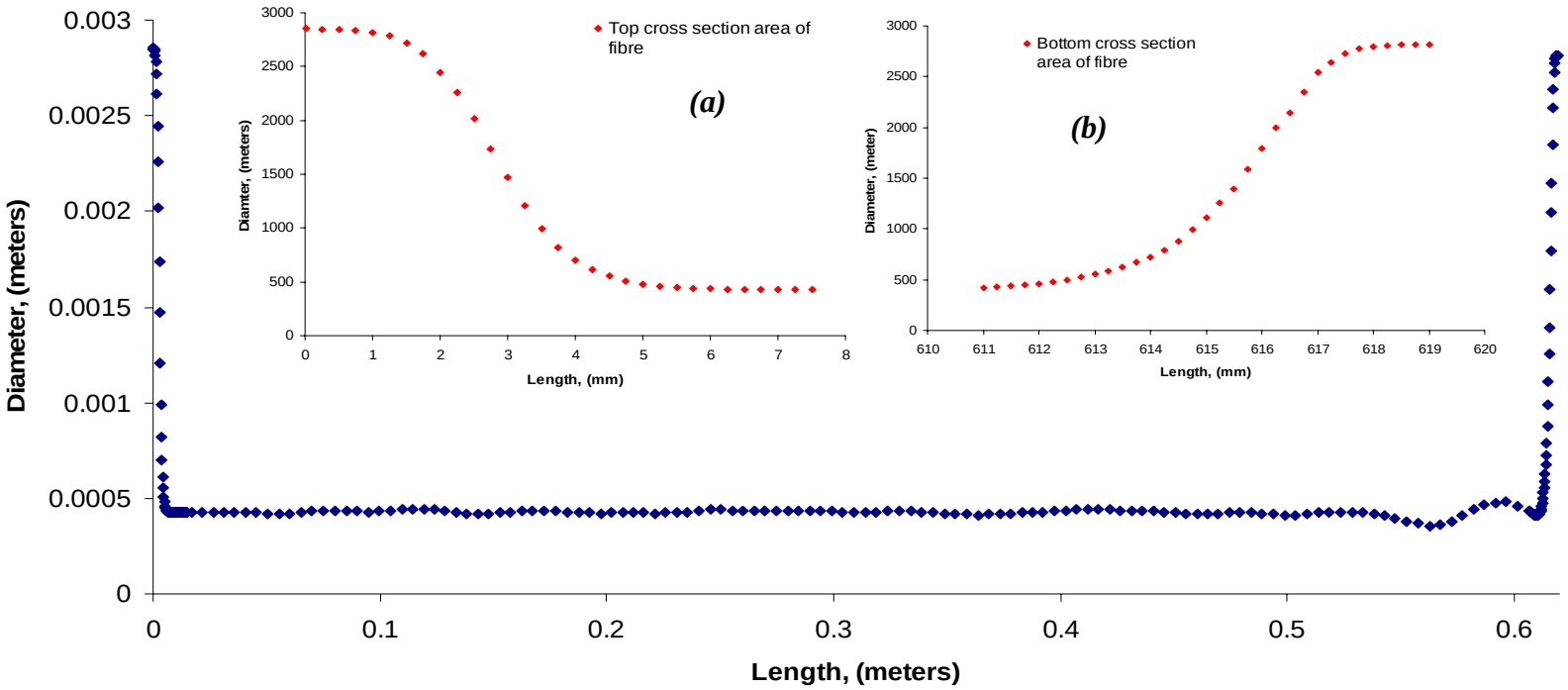

Figure 6.18. Plot showing the diameter of the full length (600 mm) silica fibre, fabricated in lab and measured in the profiler. (a) graph focusing on the diameter of the top section of the fibre (b) graph focusing the diameter of the bottom section of the fibre.

The curve of the top neck is shown in figure 6.18(a). The curved neck is approximately 5 mm in length. The uniform circular section runs for 600 mm (approx.) and a slight bump is observed at its lower ends due to a slight imperfection during the fabrication stage. The bottom neck extends from 6 mm approximately as shown in figure 6.16 (b). The bump is not observed here as the graph focuses around the neck area and not the thin uniform section of the fibre.

6.4.4 ANSYS® model of laser pulled silica fibre

Creating an ANSYS® model out of the real pulled silica fibre is a somewhat time consuming process. The steps are shows in figure 6.19 in the form of a chart. Following pulling and profiling of the fibre, the data from the profiler is then pulled out in a 'Microsoft office Excel spreadsheet'. The data (which runs into hundreds of lines) are then sorted and plotted as a graph for easy inspection. The sorted data are then fed into a LabVIEW® (Laboratory Virtual Instrumentation Engineering Workbench) program. The LabVIEW® generates codes which are then compatible with ANSYS® codes or log files.

Figure 6.19 shows a comparison of the design of the fibre fabricated in lab and its ANSYS® model created by following the four step process explained above.

An Advanced LIGO suspension model was then designed and studied using these fibres. This is discussed in the next section.

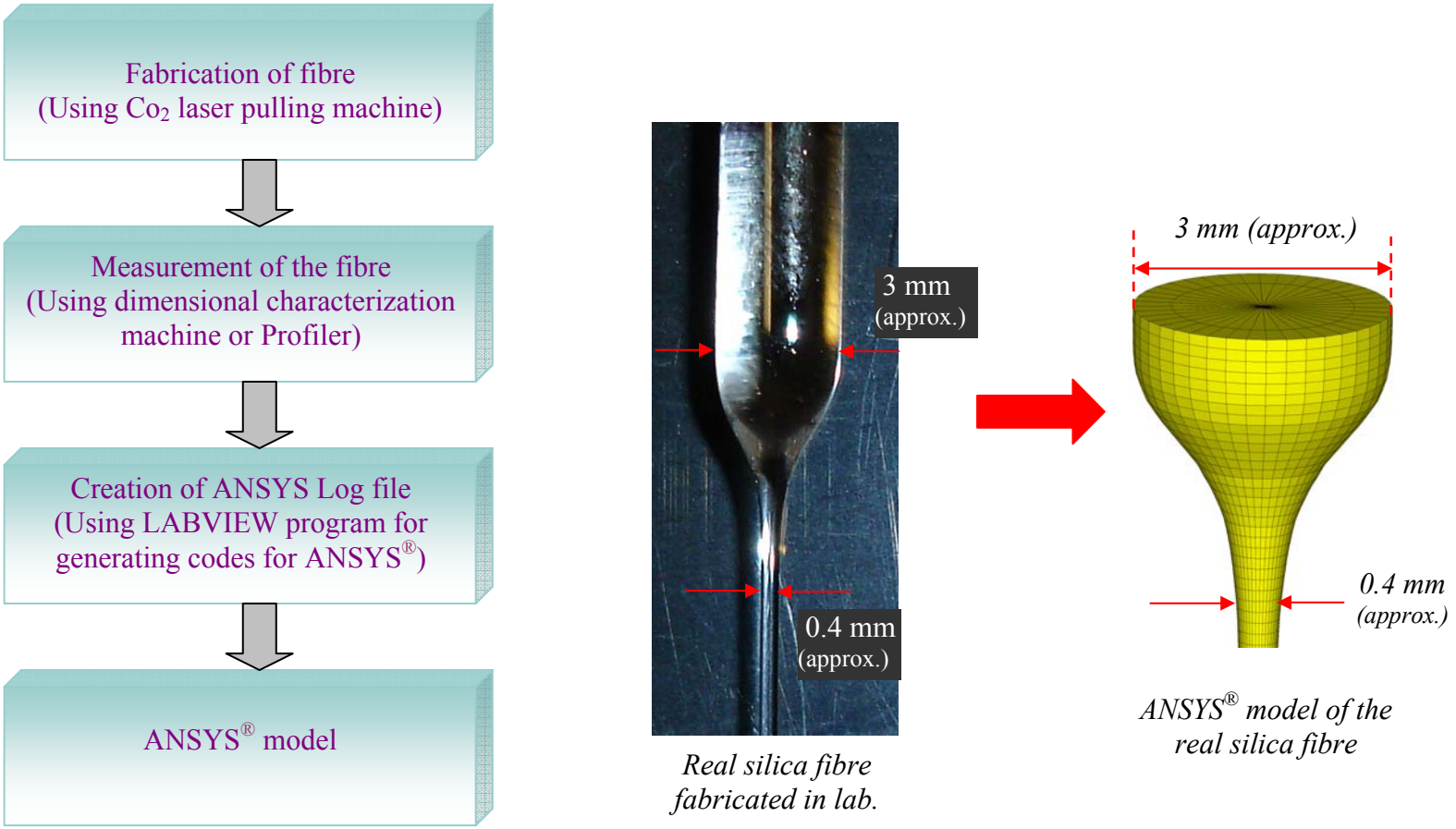

Figure 6.19. Chart showing the steps involved in creating ANSYS® model of silica fibre fabricated in lab. The picture on the right shows the sample of silica fibre pulled in lab and then converted into its ANSYS® model (extreme right side), by following the steps show in the chart.

6.4.5 ANSYS® model of Advanced LIGO suspension having laser pulled silica fibre

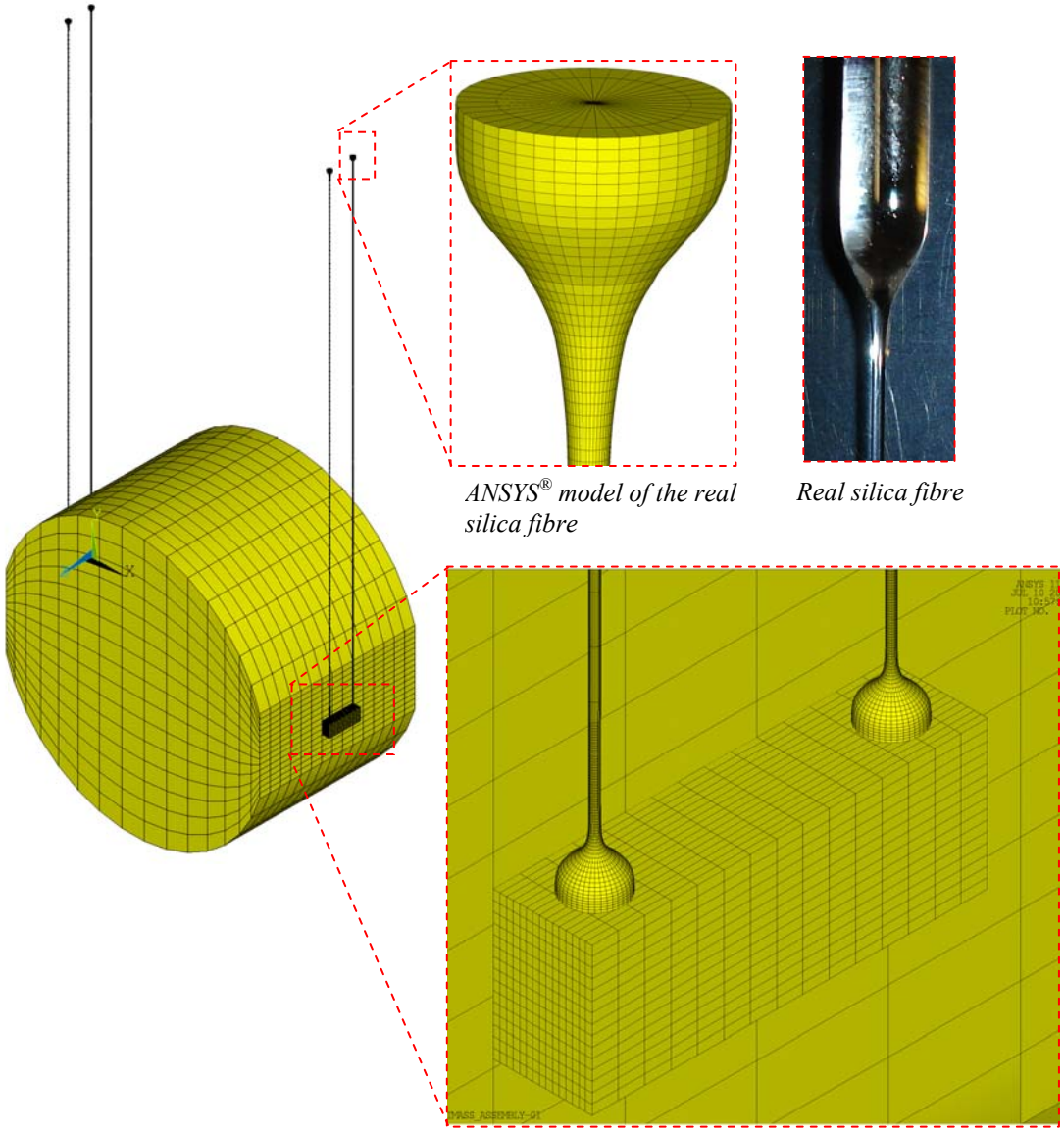

Figure 6.20. ANSYS® model of Advanced LIGO suspension model built using four silica fibres having real curved taper design. The picture of real fibre used to build the ANSYS model shown on the top right side for comparison.

Figure 6.20 shows the ANSYS® model of Advanced LIGO suspension model built using laser pulled silica fibres with curved neck design. The neck region is approximately 6-7 mm long. The stress distribution in the fibre is shown in figure 6.21.

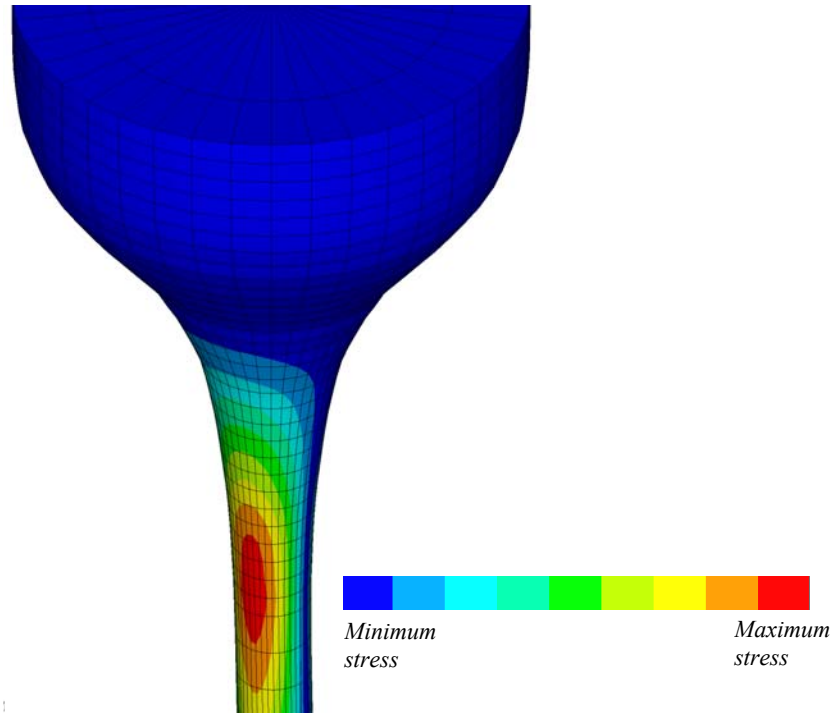

Figure 6.21. Stress distribution in the real laser pulled fibre for the Advanced LIGO suspension ANSYS® model.

The stress due to bending in this fibre is mostly seen to occur in the 0.4 mm diameter section. The neck region is mostly stress free. However the stress plot suggests that the lower section of the taper region does show some stress due to bending. If one compares the stress distribution between the real fibre and the linear taper fibre, one can see that the area of stress has increased in the former case. This is because the exponential neck gradually decreases and meets the fibre whereas as in the linear taper neck there are sharp corners which results in concentration of stress at that point.

The strain energy distribution in the fibre is plotted in figure 6.21. The thicker ends of the fibre contain negligible energy. Most of the energy can be seen to be stored after the neck region and extending into the thin fibre.

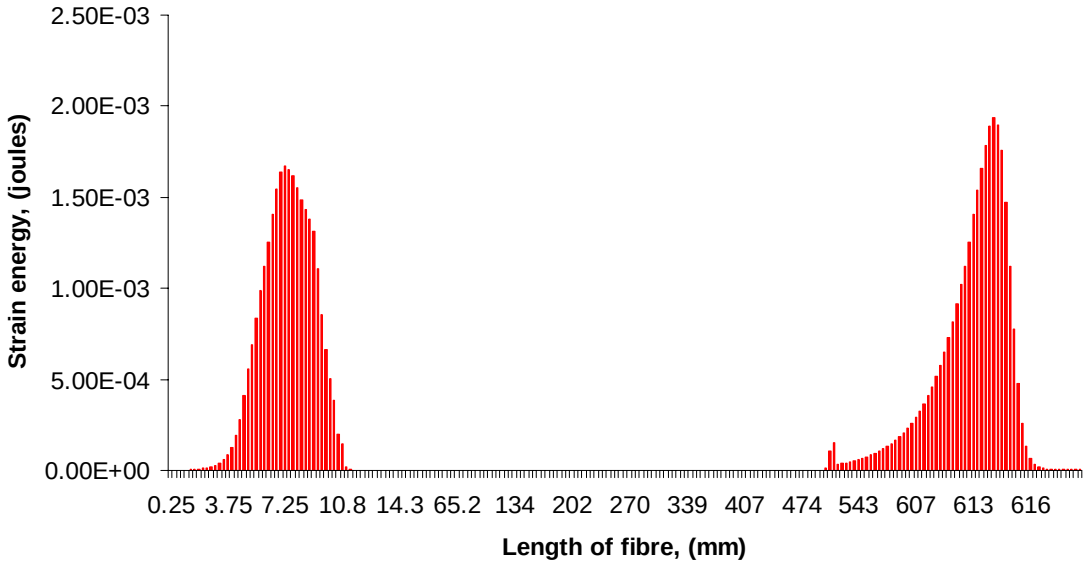

Figure 6.22. Strain energy distribution in the real laser pulled fibre for the advanced LIGO suspension.

A similar analysis for a realistic silica ribbon manufactured on the CO_2 pulling machine was carried out by A. Cumming [1]. Results from this are combined with those from the fibre in table 6.5.

Case for Advanced LIGO suspension design	Fibre Dilution Factor (ANSYS)	Fibre Dilution factor (Theory)	Ribbon Dilution factor (ANSYS)	Ribbon Dilution factor (Theory)
Uniform cross section fibre/ribbon	646	625	2048	2048
7.5 mm linear taper neck	396	625	273	2048
15 mm long linear taper neck	185	625	174	2048
Laser pulled fibre/ribbon (long neck)	139	625	146	2048

Table 6.5. Summary of dilution factor results for the Advanced LIGO suspension system. Fibres denoted in red and ribbons in blue.

This analysis clearly suggests that the laser pulled fibre and ribbon with their curved necks have poorer dilution factor than those idealised example with linear tapers.

6.5 Conclusions

The finite element analysis method has proved to be very useful in judging the performance of the suspension elements in the Advance LIGO suspension system. The dissipation dilution results evaluated in this chapter have shown that there is little difference between real silica fibres and ribbons in terms of dilution factor. In practice fibres are somewhat easier to manufacture than ribbons and thus may be a better choice.

However with low dilution factor thermal noise might be expected to become a significant problem with either fibres or ribbons and this issue will be addressed in the next chapter.

Chapter 7

Optimisation of Advanced LIGO fibre design to minimise thermal loss

7.1 Introduction

The results obtained in the previous chapter suggest that the dilution factor of both the realistic ribbon and fibres will be much lower than originally conceived and the significance of this for the pendulum thermal noise in the Advanced LIGO needs to be evaluated.

It should be noted however that the full expression for the thermoelastic dissipation as discussed in chapter 2 contained a term for the thermoelastic strength.

$$\Delta = \frac{ET}{\rho C}\left[\alpha - \frac{\sigma}{Y^2}\frac{dY}{dT}\right]^2, \tag{7.1}$$

and these symbols have their usual meaning with σ the stress in the ribbons or fibres.

This full expression had not been developed at the time when ribbons were first envisaged for the Advanced LIGO suspension. In fact the Advanced LIGO design was originally based on using ribbons of high dilution factor with the main loss term being that associated with thermoelastic loss when σ (stress) is assumed to be zero. This assumption is incorrect for the suspensions envisaged and gives a loss, and thermal noise level, which is over-optimistic. When the full expression for thermoelastic loss is used the loss, and the noise level, are significantly higher (see 7.1.1 below). Intuitively, as dilution factors are much lower when tapered ends are used, loss and thermal noise levels might be expected to be worse still. However there is potential for ameliorating the increase in thermal noise resulting from the reduction of the dilution factor associated with the use of tapered ends. This amelioration is achieved by choosing the stress in the suspension elements such that the overall thermoelastic loss factor is significantly reduced, as suggested by Cagnoli [68].

The situation can be analysed by first looking at the baseline ribbon loss leading to thermal noise which had high dilution factor. Secondly the real ribbon situation, where the dilution is reduced but partial cancellation of the thermoelastic loss takes place due to the stress in the ribbon, is considered. Thirdly the thermal noise in the real fibre needs to be estimated.

Then the fibre design needs to be further optimised if possible to minimise the loss leading to thermal noise and then compare the resulting loss level with that from the ribbon.

7.1.1 Baseline mechanical loss calculation for Advanced LIGO suspension

This calculation is based on suspension ribbons of length 60 cm, uniform width 1.1 mm and thickness 0.11 mm, loaded with 40 kg. As discussed in chapter 6 this gave a dilution factor of 2048.

We may use,

$$\phi_{thermal} = \phi_{thermoelastic} + \phi_{surface-loss} + \phi_{bulk-loss}. \tag{7.2}$$

where $\phi_{thermal}$ is the loss of the material of the ribbon or the pendulum, $\phi_{surface\text{-}loss}(\omega)$ is the loss associated with any surface damage of flame polished or flame drawn fused silica samples due to absorbed contaminants etc [70] and $\phi_{bulk\text{-}loss}(\omega)$ is the loss in the body of the material, now thought to be associated with the strained Si-O-Si bonds in silica as discussed fully by Penn et al [71].

The total loss for the pendulum was calculated using equation number 2.27 in chapter 2, by colleagues A. Heptonstall and A. Cumming, as reported in [1], and this is shown as a function of frequency in figure 7.1.

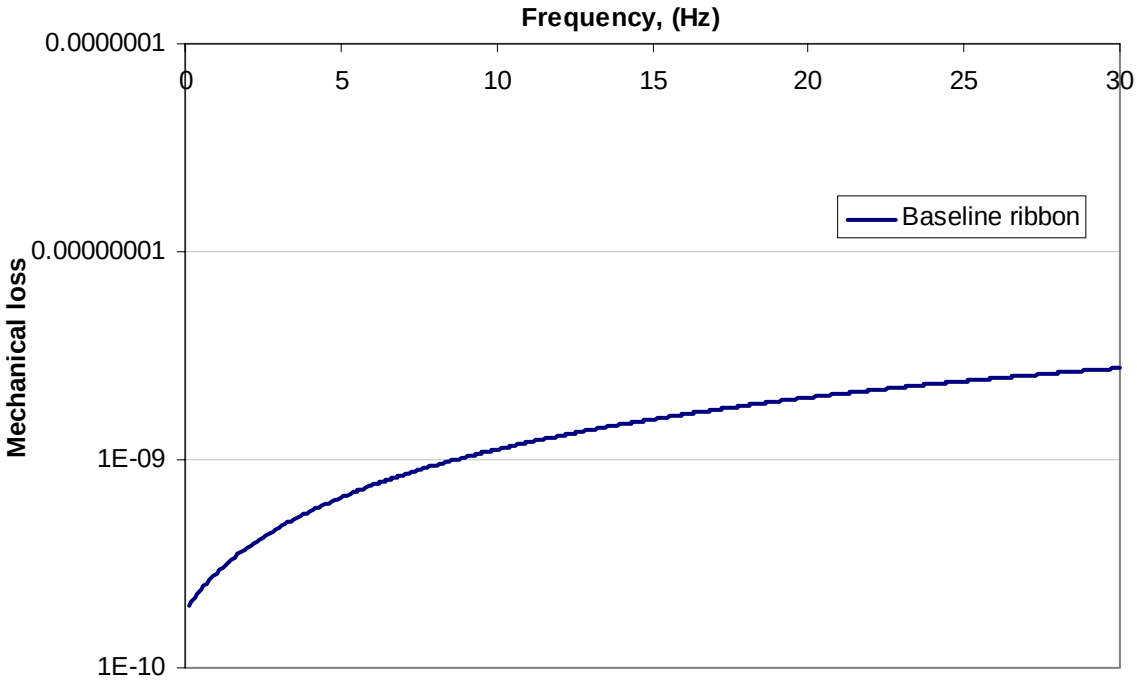

Figure 7.1. Mechanical loss estimated for the baseline ribbon in the Advanced LIGO suspension system.

7.1.2 Mechanical loss calculation for a suspension using real ribbons for Advanced LIGO

For this case A. Heptonstall and A. Cumming developed a MAPLE® code which allowed the energy stored in each section, δy , of the ribbon and the overall $\delta\phi_{\text{thermal}}$, including the full thermoelastic loss value, to be combined and integrated over the length of the ribbon. These ribbons were manufactured using a CO_2 laser pulling machine. The variation of mechanical loss with frequency for the system is shown in figure 7.2.

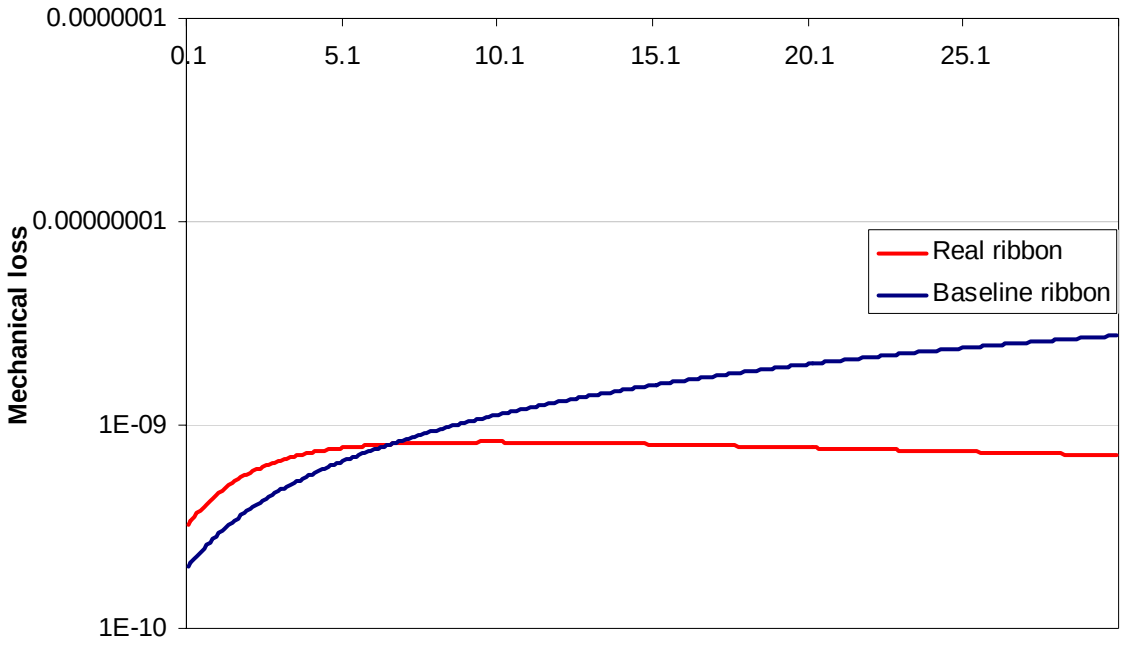

Figure 7.2. Mechanical loss estimated for the real ribbon compared with the baseline ribbon in the Advanced LIGO suspension system.

It can be seen that the overall mechanical loss associated with the pendulum movement is significantly better than that for the baseline case for frequencies above ~ 6 Hz.

This comes about because of partial cancellation of the thermoelastic loss due to the stress value in the tapered part of the ribbon where bending takes place, and is very significant for the potential performance of the Advanced LIGO detector.

7.1.3 Mechanical loss calculation for a suspension using real fibres for Advanced LIGO

A similar analysis to that above was carried out for real fibres as manufactured by the CO_2 laser pulling machine and the results are shown in figure 7.3

As can be seen the pendulum loss factor here is higher than that for a pendulum suspended from the real ribbons because the mechanical loss is not reduced by as much with this fibre geometry.

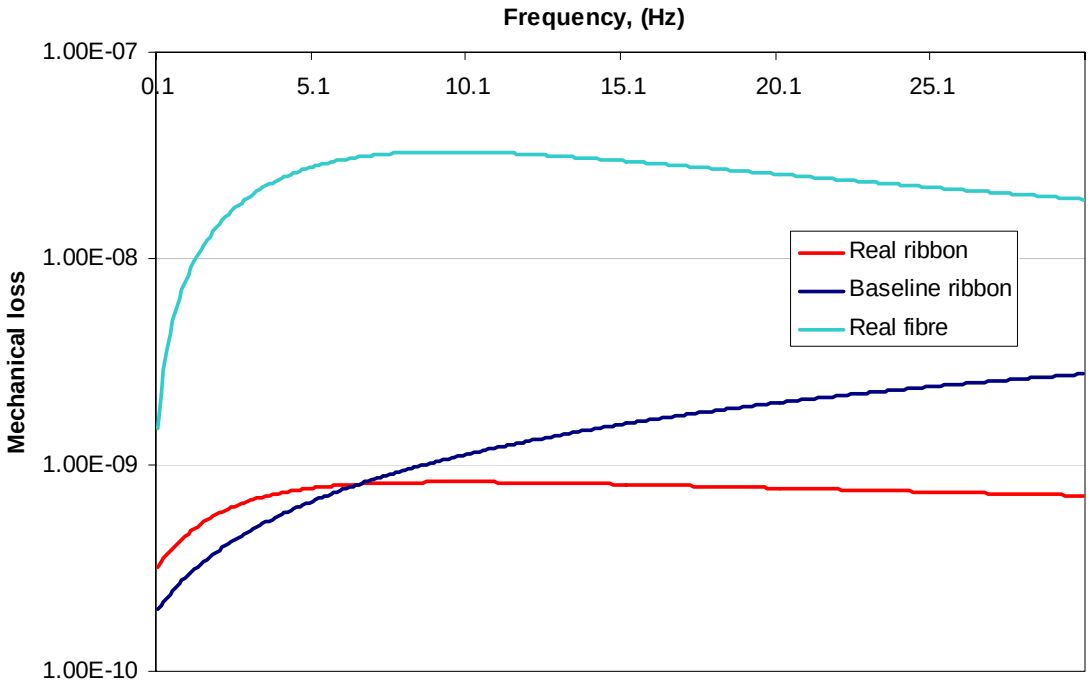

Figure 7.3. *Mechanical loss estimated for the real fibre which is then compared with the baseline ribbon and real ribbon in the Advanced LIGO suspension system.*

7.1.4 Idealised fibres to minimise the mechanical loss

From equation 7.1 it is clear that the thermoelastic loss will be zero if $\sigma = \alpha Y^2 / \frac{dY}{dT}$. Now $\alpha = 5.1\times10^{-7}\,\mathrm{K}^{-1}$, $Y = 7.2\times 10^{10}$ Pascal and $dY/dT = 1.1\times10^{7}$ Pascal K^{-1} [68]; hence the required $\sigma = 2.45\times10^{8}$ Pascal. For a loading of each fibre of 10 kg (100 N) this corresponds to choosing a fibre diameter ~ 800 microns. However with a fibre of such diameter the vertical bounce mode will be higher than acceptable for Advanced LIGO and the violin mode will be too low. To reduce the vertical bounce mode a thinner section can be put into

the fibre between the 800 micron diameter sections where the fibre is bending, as suggested by Willems [72]. A suitable fibre for Advanced LIGO is shown in figure 7.4.

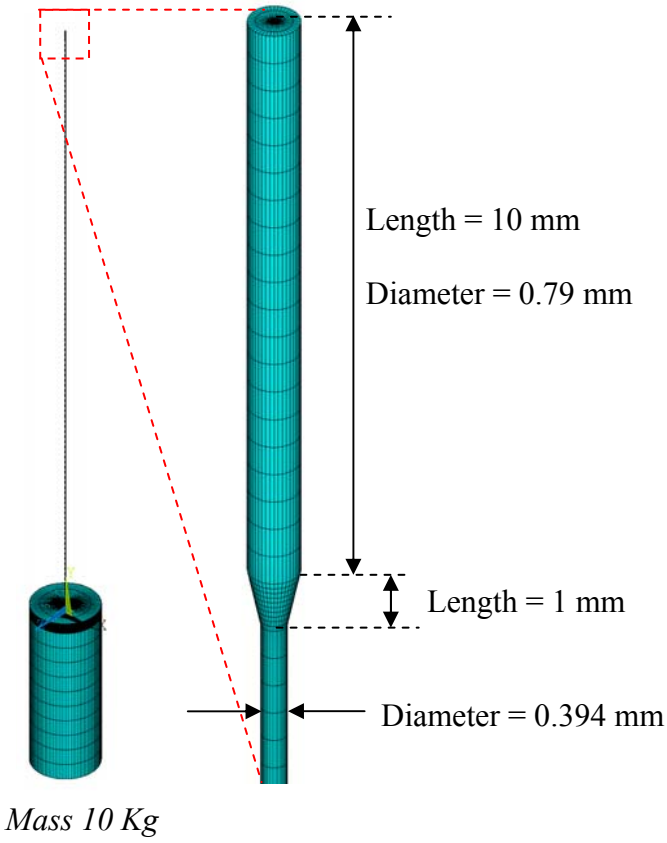

Figure 7.4. ANSYS® model of a single wire pendulum system, built using fibre of two different cross section area, suspending a mass of 10 kg

The length of the fibre here is taken as 600 mm, which is the same as planned for use in the Advanced LIGO suspension system. The structure of the fibre comprises portions of different cross sectional area. The starting diameter of the fibre is 0.79 mm over a length of 10 mm, followed by a linear taper of length 1 mm. The tapered section is joined to another section of the fibre having a diameter of 0.394 mm which is 578 mm long. The bottom section of the fibre is same as that of the top section, thus making a total length of 600 mm.

This pendulum model was then clamped from the top and gravity was applied and solved in ANSYS® to obtain the vertical bounce mode and first violin mode.

Mode shape	Bounce mode	First violin mode
Mode frequency	6.205	510

Table 7.1. Relevant mode frequencies of the pendulum model built using re-designed fibres (for thermoelastic damping)

These results fit well with the Advanced LIGO specifications, where the bounce mode was to be less than 10 Hz and the first violin mode was required to be above 400 Hz as shown in table 7.1.

7.1.4.1 Bending length of the fibre

From the FE analysis the bending length of the fibre comes out to be 4.35 mm. The contour shown in figure 7.5 illustrates this situation. This shows that the fibre is bending at the top of the thickest section of the fibre. In the case of Advanced LIGO there will be an equivalent bending at the bottom of the fibre.

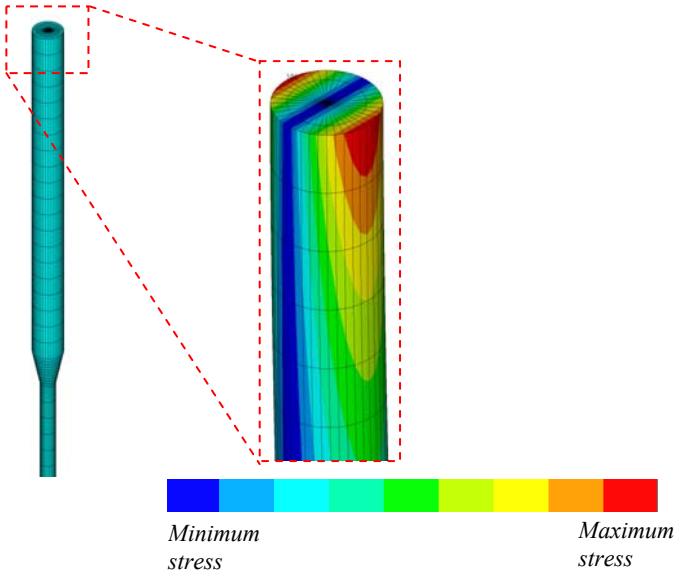

Figure 7.5. Contours showing the stress plot of the fibre which gives the bending point of the fibre.

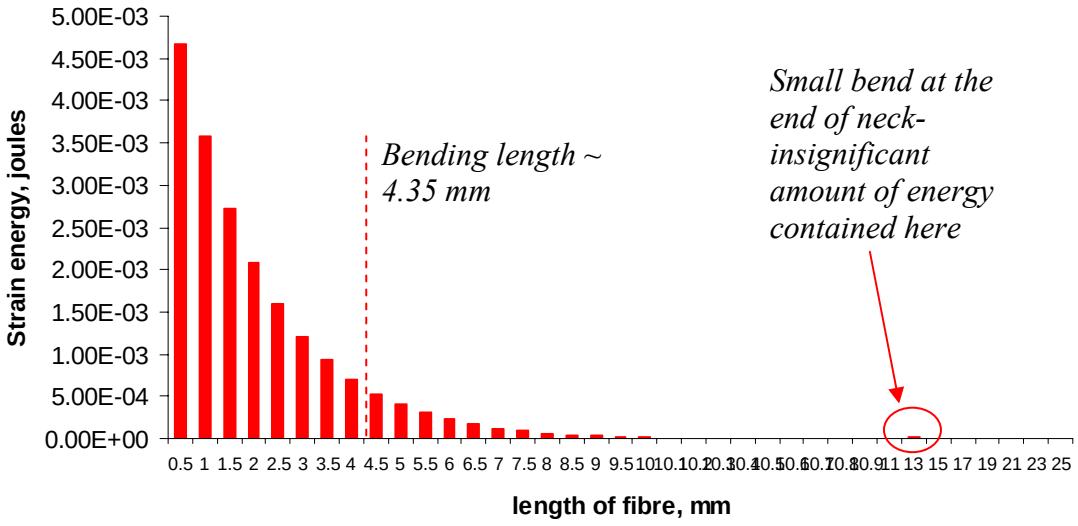

Figure 7.6. Energy distribution in the top part of the fibre suspending a mass of 10 kg.

The strain energy distribution graph (figure 7.6) shows most of the energy is stored in the top section of the fibre (i.e. at the thickest section) and it decreases exponentially along the length of fibre length. An equivalent condition holds at the bottom of each fibre in the case of Advanced LIGO suspension.

Dumbbell fibre (as shown in figure 7.1), suspending 10 kg	**Theory** (only bending at top) for 0.79 mm diameter fibre, suspending 10 kg	**Single pendulum** built using **Ad-LIGO fibre**, suspending 10 kg	**Theory** (only bending at top) for 0.4 mm tapered fibre, suspending 10 kg
371	360	872	1405

Table 7.2. Dilution factor comparison of the dumbbell fibre with the previous results of a single pendulum built using advanced LIGO fibre.

The dilution results are shown in table 7.2. The dumbbell fibre modelled in section 7.1.4 is compared with theory and also with the previous design of single pendulum model (from chapter 4). The result shows a big drop in dilution factor as most of the energy is stored in the thicker section of the fibre.

However it is important to remember that the reduction in dilution factor is expected to be ameliorated by the low level of thermoelastic loss.

A real fibre, approximately of this idealised design was manufactured by 'A. Heptonstall' and its profile was measured by 'A. Cumming' [1] and is shown in figure 7.7.

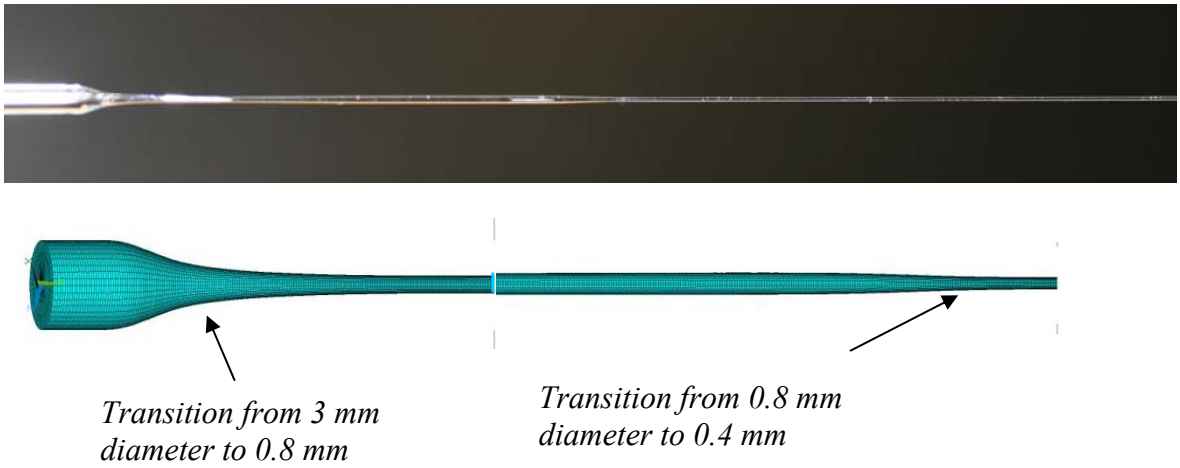

Figure 7.7. Top: Picture of a real dumbbell fibre fabricated in laboratory. Bottom picture is the ANSYS® model of the same.

The total pendulum mechanical loss was calculated for this dumbbell fibre and is shown in figure 7.8, where it can be compared with the pendulum loss expected using the real ribbons, real fibres and baseline ribbon design discussed earlier.

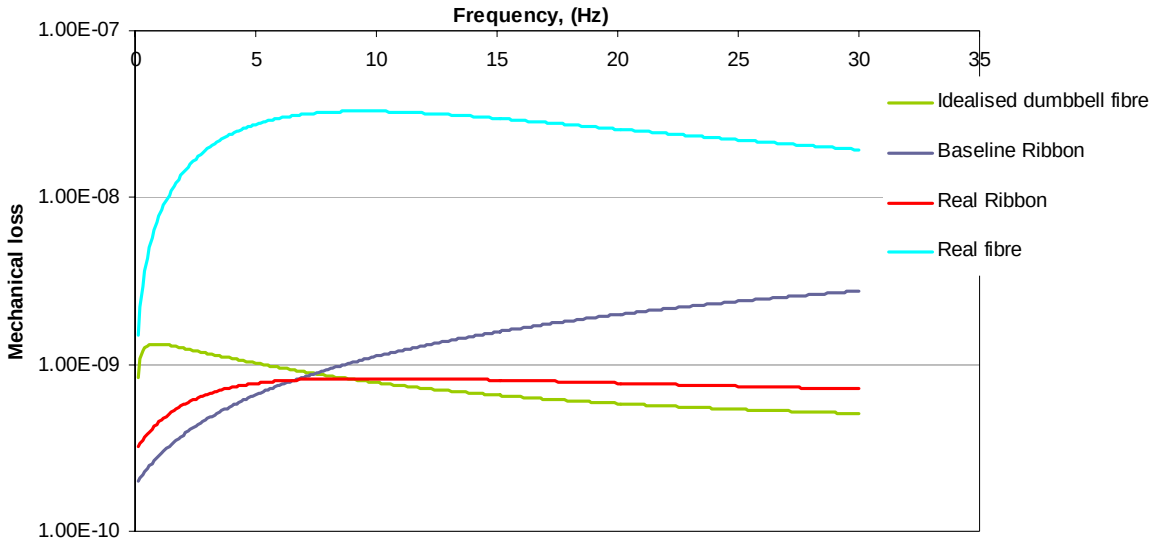

Figure 7.8. Mechanical loss plotted for the case of idealised dumbbell fibre and compared with other designs. The idealised fibre is clearly showing a low mechanical loss as compared to others above 8 Hz.

As can be seen the performance of this fibre is better than the idealised ribbon or real ribbon above 8 ~ Hz.

Thus such fibres have significant potential for the baseline design of the Advanced LIGO suspension system.

7.2 Basic "Ear" and "Weld" representation in the dumbbell shaped fibre

The ends of the ears and the "welds" have been included into the model of the dumbbell fibre as discussed in the next three sections. The ends of the ears are modelled here as silica cylinders 5 mm long and 3 mm diameter.

7.2.1 Ear-ends directly bonded to the fibre

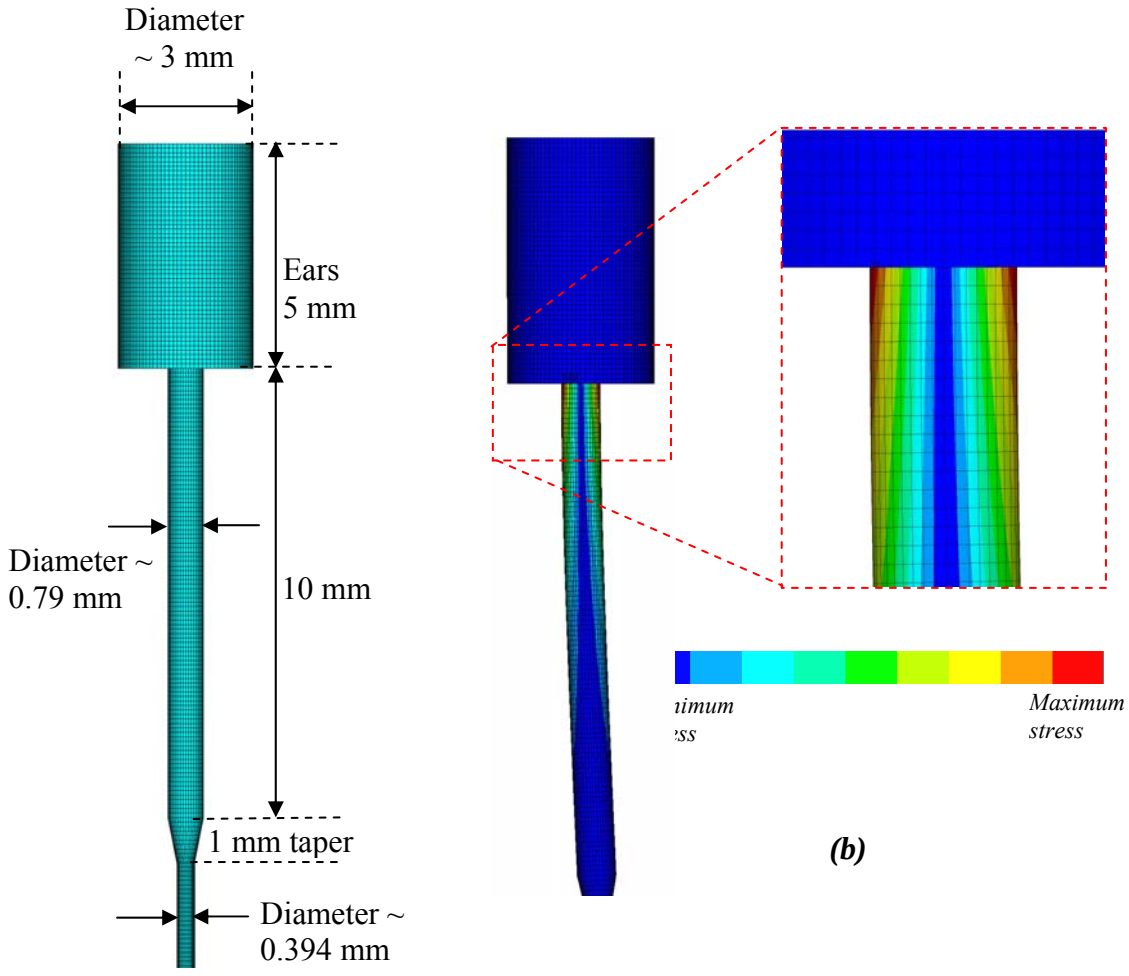

(a) *Design 1*

Figure 7.9. (a) ANSYS® model of 'end of Ear' attached to the dumbbell fibre. (b) Contours showing stress plot of the fibre designed in ANSYS and tested by suspending a mass of 10 kg at its end.

Ends of ears of this dimension have been chosen so as to be sufficiently stiff to prevent accumulation of significant energy in them as shown in figure 7.9.

The structure was subjected to a load of 10 Kg at one end and the other end was clamped as usual. The ANSYS results are discussed as followed.

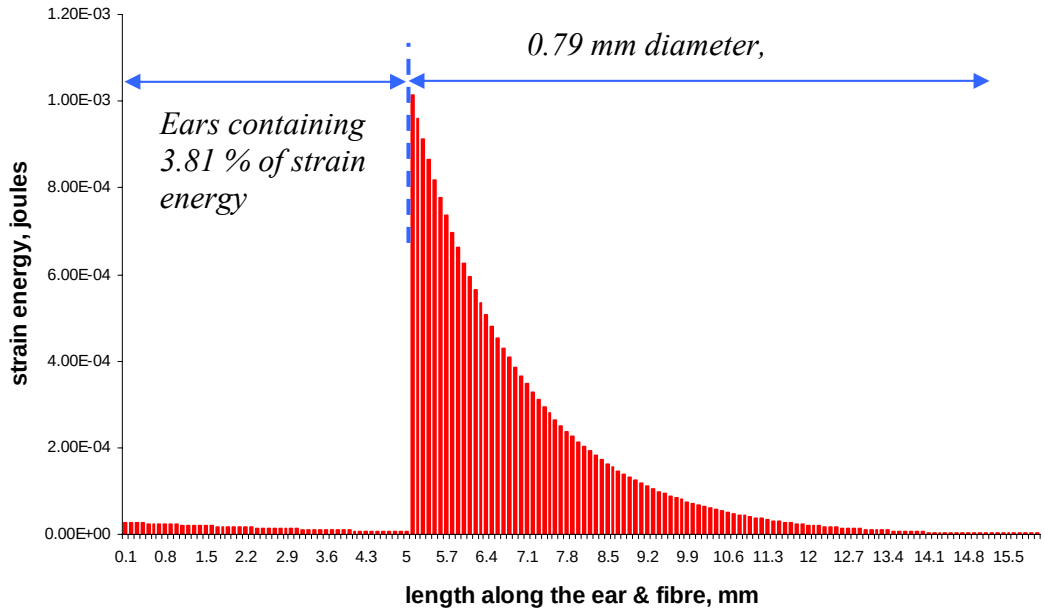

Figure 7.10. Energy distribution in the dumbbell fibre and the ears. The ears contain 3.81 % of total energy and the rest is in thin fibre (0. 79 mm diameter sections).

The contour plots shown in figure 7.9 (b) give an indication of the response of the structure under stress. The energy is mostly concentrated at the top edge of the thin fibre and it extends only slightly into the ear section. This is good as it shows that the designed ears are stiff enough to resist bending.

The stress plot from ANSYS is complemented by the strain energy distribution graph shown in figure 7.10. Energy is mostly (almost 96%) concentrated in the 0.79 mm diameter section and an insignificant (3.81%) amount in the ears.

7.2.2 Representation of 1-2 mm long weld in the fibre-ear-ends structure

The next step was to add small "welds" between the dumbbell fibre and the ears and then vary the lengths of the welds to study their effects on the over all energy distribution.

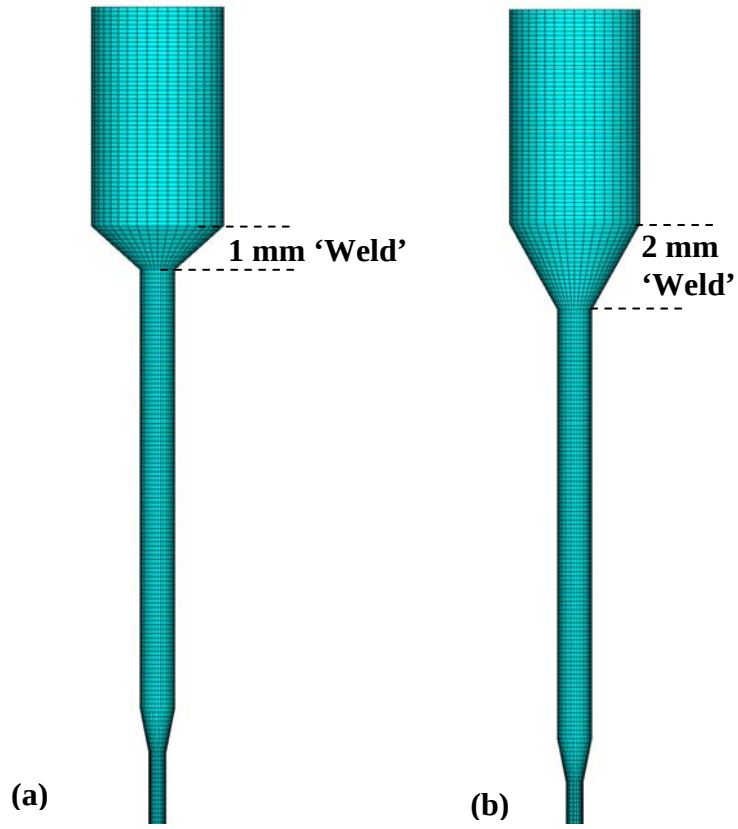

Figure 7.11. ANSYS® model of dumbbell fibre welded to Ear. (a) 1 mm long 'weld' (b) 2 mm long 'weld'.

Lengths of welds of 1 or 2 mm are typical of what can be achieved with either flame welding or laser welding as shown in figure 7.11.

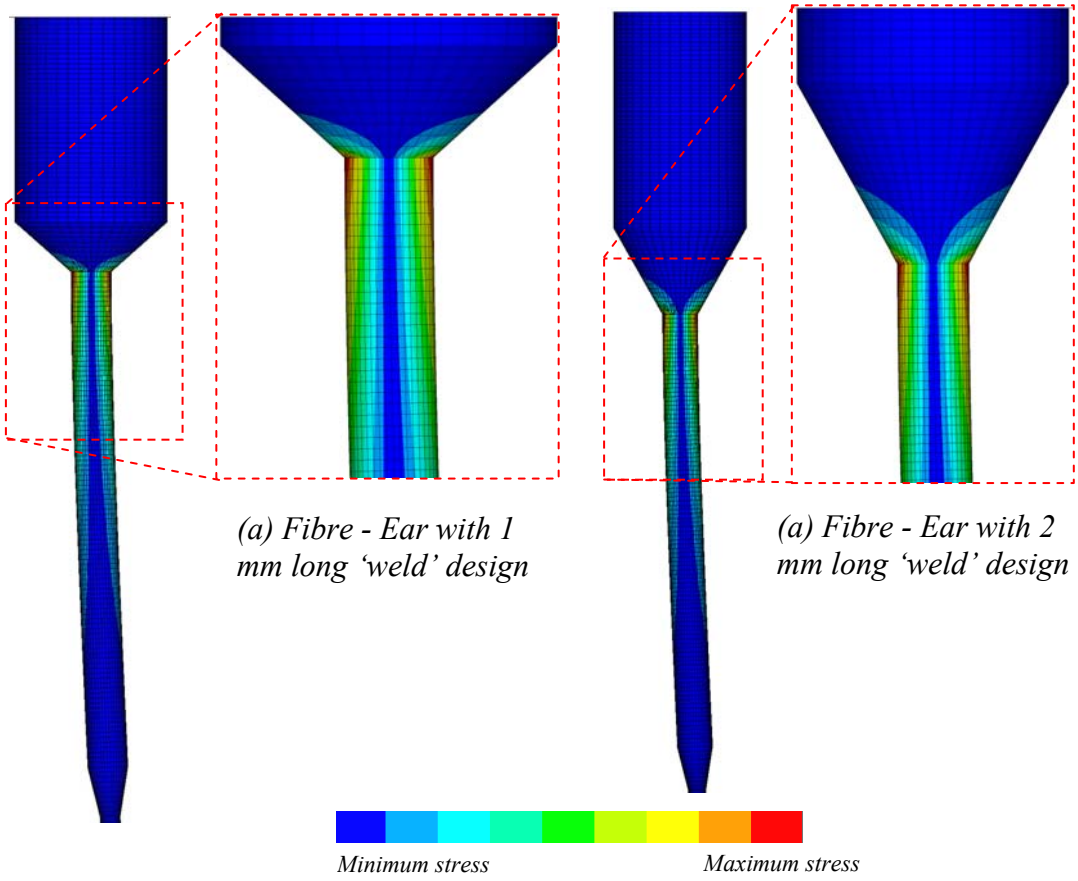

Figure 7.12. Contours showing the region of maximum and minimum stress in the body. (a) represents 1 mm weld fibre structure (b) represents 2 mm weld fibre structure

The stress plot shown in figure 7.12 suggests that the structure starts to bend from the lower edge of the 'weld'. However most of the bending is observed at the top section of fibre structure (0.79 mm diameter region). On comparing the 1 mm and 2 mm 'weld' region, the latter one seems to absorb more energy. This was expected as previous experience shows that longer tapers are not very good for the purpose of energy distribution. However the ears in either case are stiff enough to resist bending.

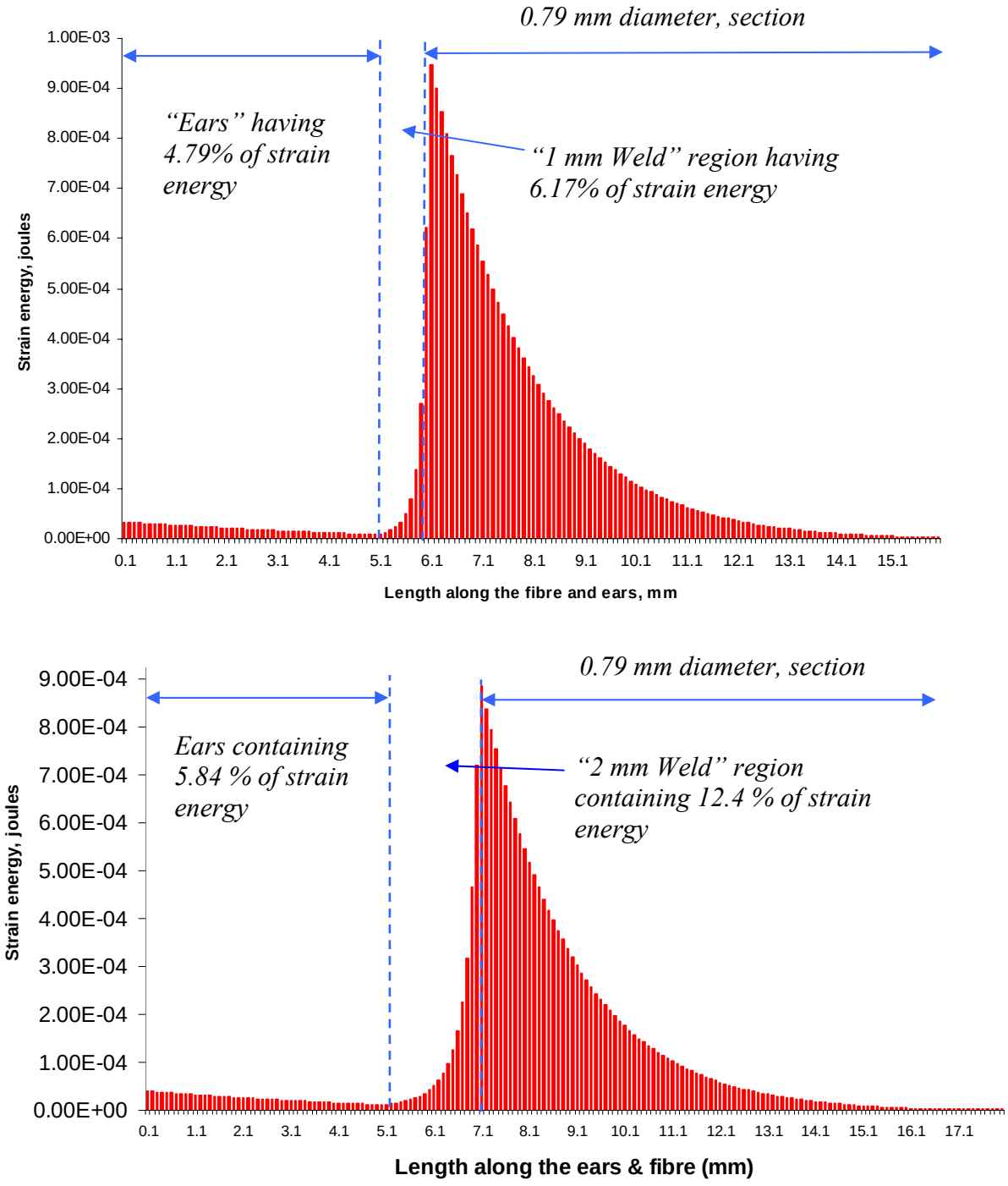

Figure 7.13. Energy distribution in the structure comprising of fibre-weld-ear-ends. The dotted line segregates the three sections for clarity. The inclusion of welds has led to slight infiltration of energy into ears and weld section,. The top graph represents the 1 mm long weld fibre structure and the bottom graph is for 2 mm long weld fibre structure.

The graph shown in figure 7.13 gives the distribution of energy in the entire structure. The ears contain a small percentage of total energy. For the 1 mm weld fibre structure 4.78% of the energy is stored in the ears and as the length of the weld is increased the energy in the ears goes up to 5.84%. It is believed this level of energy in the ears will not make significant difference to the thermal noise performance. The intention is to contain most of the energy in the dumbbell fibre region and not let it extend significantly into the ears.

Dumbbell fibre + Ear structure (no weld)	Dumbbell fibre + weld (1 mm long) + Ear structure	Dumbbell fibre + weld (2 mm long) + Ear structure
363	360	354

Table 7.3. Dilution factor comparison for the three different cases of dumbbell fibre bonded to ear and weld (1-2 mm long) structure.

On comparing the results for all the three cases as shown in table 7.3, one can infer that inclusion of 'welds' in the structure is not changing the dilution factor by much. However a problem could exist if welds have levels of excess mechanical loss associated with them. Such loss might results from high levels of stress in the welded region or possibly from a deposit of silicon oxide resulting from the welding process. Mechanical losses associated with welded silica is an area of future research.

7.3 Conclusions

A full analysis of the silica suspension system for the Advanced LIGO clearly shows that the optimum design of suspension element for this detector is silica fibre of dumbbell shape to minimise thermoelastic loss while observing the required constraints on internal resonance frequencies.

Chapter 8

Conclusions

As the sensitivities of interferometric gravitational wave detectors improve, the possibility of directly detecting gravitational wave signals becomes a reality. One of the most challenging areas of research is to reduce the effect of thermal noise in the suspension systems of these detectors. Significant progress has been made in the development of the suspension system of the Advanced LIGO detector. The work in this thesis is devoted towards the development of the suspension elements in these detectors, using the finite element analysis method.

Before analysing the suspension elements of the Advanced LIGO suspension system, a prototype design was modelled in ANSYS®. This was of a single fibre or ribbon pendulum system suspending a 10 kg mass (which approximately makes a quarter section of the Advanced LIGO pendulum model). At first pendulum suspensions comprising of fibres or ribbons of uniform cross sectional area were analysed and subsequently fibres or ribbons with tapered ends were included and studied for various taper lengths. The study of tapered ends in the fibre or ribbon is very important as any real system requires such necks for joining purposes. Through this model important aspects of the pendulum design were studied which included the evaluation of strain energy distributions in the fibres or ribbons, with the help of which the dilution factor of the pendulums were estimated. The most

important finding from this area of research was the extent to which the tapered ends reduced the dilution factor of the pendulum.

The single fibre pendulum design was then extended to a two-fibre pendulum system comprising of a 20 kg mass. This model was studied as a step between the single fibre system and the four fibres/ribbons system for the Advanced LIGO detector. There are some other important issues in the two-fibre pendulum model which were observed while studying it and these are related to coupling of the pendulum and tilt modes which leads to reduced dilution factor. The importance of attaching the fibre or ribbons close to a plane through the centre of mass was very clear.

The Advanced LIGO suspension system was then modelled. The focus was on comparing the performance of silica fibres and ribbons and the associated dissipation dilution factor of the pendulum system. Similar to the single fibre and two fibre pendulum cases here the fibres or ribbons were first studied for uniform cross section and then for tapered ends. Further the performance achievable using real fibres and ribbons fabricated in the laboratory was also modelled. The strain energy distribution in these suspension elements was used to compare their performance and again it was found that the dissipation dilution factor was seriously impaired compared with that of uniform fibres or ribbons.

Finally given the poor dilution factor which can realistically be obtained it became very important to investigate whether the major factor contributing to the material loss, i.e. the thermoelastic effect, could be reduced. This can be achieved by tailoring the stress level at the point where the fibres or ribbons bend. Realistic designs of fibres or ribbons were analysed and shown to be acceptable for use in the Advanced LIGO detector.

Bibliography

[1] Cumming A (2008) *Aspects of mirrors and suspensions for advanced gravitational wave detectors* Department of Physics and Astronomy University of Glasgow PhD Thesis

[2] Rowan S et al. (2000) *Gravitational wave detection by interferometry (ground and space)* from http://www.livingreviews.org/lrr-2000-3

[3] Einstein A (1916) *Die grundlage der algemeinen relativitatstheorie* Annalen der Physik 49 769

[4] Einstein A et al. (1937) *On gravitational waves* Journal of the Franklin Institute 233

[5] Weber J (1969) *Evidence for discovery of gravitational radiation* Physical Review Letters 22 1320

[6] Weber J (1970) *Anisotropy and polarization in the gravitational-radiation experiments* Physical Review Letters 25 180

[7] Pallottino G V (1998) *The resonant mass detectors of the Rome group* Eds. E Coccia G Veneziano and G Pizzella Gravitational Waves, Second Edoardo Amaldi Conference held in CERN Switzerland World Scientific press

[8] Prodi G A (1998) *Initial operation of the gravitational wave detector Auriga* Eds. E Coccia, and G Veneziano and G Pizzella Second Edoardo Amaldi Conference held in CERN Switzerland Edoardo Amaldi Foundation Series

[9] Hulse R (1994) *The discovery of the binary pulsar* Reviews of Modern Physics 66 699

[10] Taylor J (1994) *Binary pulsars and relativistic gravity* Reviews of Modern Physics 66 711

[11] Will C M (1993) *Theory and experiment in gravitational physics* Cambridge University Press Cambridge UK

[12] Saulson P (1994) *Fundamentals of interferometric gravitational wave detection* World Scientific Singapore

[13] Heptonstall A (2004) *Characterization of mechanical loss in fused ribbons for use in gravitational wave detector suspensions* Department of Physics and Astronomy University of Glasgow PhD Thesis

[14] Schutz B (1996) *The detection of gravitational waves* Eds. J A Marck and J P Lasota in Proceedings of the Les Houches School on Astrophysical Sources of Gravitational Radiation Springer Berlin

[15] Lobo J A (1996) *Sources of gravitational waves* Eds. G S Hall J R Pulhamin General Relativity: Proceedings of the Forty Sixth Scottish Universities Summer School in Physics Aberdeen CRC Press

[16] Abbott B et al. (2007) *Search for gravitational-wave bursts in LIGO data from the fourth science run* Classical and Quantum Gravity 24 5343

[17] Hough J et al. (2005) *The search for gravitational waves* Journal of Physics B: Atomic and Molecular Physics 38 S497

[18] Abramovici A et al. (1994) *Gravitational Wave Astrophysics* Eds. E W Kolb and R Peccei in Proceedings of the 1994 Snowmass Summer Study on Particle and Nuclear Astrophysics and Cosmology Colorado Word Scientific Singapore 398

[19] Pitkin M et al. (2008) *Beating the spin-down limit on gravitational wave emission from the Crab Pulsar* arXiv:0805.4758v2 [astro-ph]

[20] Hough J et al. (1989) *Proposal for a joint German-British Interferometric gravitational wave detector* Max-Planck-Institut fur Quantenoptik Report 147 and GWD/137/JH(89)

[21] Abbott B et al. (2007) *Searching for a stochastic background of Gravitational waves with LIGO* The Astrophysical Journal 659 918

[22] Forward R L et al. (1961) *Upper limit for interstellar millicycle gravitational radiation* Nature 189 473

[23] Forward R L (1978) *Wideband laser-interferometer graviational-radiation experiment* Physical Review D 17 379

[24] Weiss R (1972) *Electromagetically coupled broadband gravitational antenna quarterly progress report* Research Laboratory of Electronics MIT 54

[25] Drever R W P et al. (1983) *Gravity-wave detector using optical cavity sensing in general relativity and gravitation* Ed. E Schmutzer in proceedings of the 9th International Conference on General Relativity and Gravitation Jena Cambridge University Press UK

[26] Meers B (1988) *Recycling in laser-interferometric gravitational-wave detectors* Physical Review D 38 2317

[27] Drever R W P (1983) *Interferometric detectors of gravitational radiation* North Holland Publishing Elsevier

[28] Danzman K (1997) *Gravitational wave observatory in heliocentric orbit* Eds K Tsubono M-K Fujimoto K Kuroda in Proceedings of the TAMA International

Workshop on Gravitational Wave Detection Japan Universal Academy Press Inc. Tokyo

[29] Hough J et al. (1989) *Proposal for a Joint German-British interferometric gravitational wave detector* Max-Planck-Institut fur Quantenoptik Report 147 and GWD/137/JH(89)

[30] Husman M et al. (2000) *Modeling of multistage pendulums: triple pendulum suspension for GEO 600* Review of Scientic Instruments 71(6) 2546

[31] Rudiger A et al. (1981) *A mode selector to suppress fluctuations in laser-beam geometry* Optica Acta 641

[32] Hughes S et al. (1998) *Seismic gravity-gradient noise in interferometric gravitational-wave detectors* Physical Review D 58 122002

[33] Plissi M et al. (2000) *GEO 600 triple pendulum suspension system: seismic isolation and control* Review of Scientic Instruments 71 2539

[34] Torrie C (2000) *Development of suspensions for the GEO 600 gravitational wave detector* Department of Physics and Astronomy University of Glasgow Ph. D. Thesis

[35] Gossler S et al. (2002) *The mode cleaner system and suspension aspects of GEO 600* Classical and Quantum Gravity 19 1835

[36] Hough J et al. (1997) *GEO 600: Current status and some aspects of the design* Eds. K TSubono M KFujimoto and K Kuroda TAMA International Workshop on Gravitational Wave detection Japan Universal Academy Press Inc Tokyo

[37] Gossler S et al. (2004) *Damping and tuning of the fibre violin modes in monolithic silica suspension* Classical and Quantum Gravity 21 923

[38] Acernese F et al. (2004) *Results of the Virgo central interferometer commissioning* Classical and Quantum Gravity 21 S395

[39] Takahashi R et al. (2004) *Status of TAMA300* Classical and Quantum Gravity 21 S403

[40] Brown R (1828) *A brief account of microscopical observations made in the months of June, July and August, 1827, on the particles contained in the pollen of plants; and on the general existence of active molecules in organic and inorganic bodies* Edinburgh New Philosophical Journal 358

[41] Einstein A (1956) *Über die von der molekularkinetischen theorie der wärme geforderte bewegung von in ruhenden flüssigkeiten suspendierten teilchen* Annalen der Physik 322 549

[42] Callen H B et al. (1951) *Irreversibility and generalized noise* Physical Review B 83 34

[43] Rowan S et al. (2005) *Thermal noise and material issues for gravitational wave detectors* Physics Letters A 347 25

[44] Saulson P (1990) *Thermal noise in mechanical experiments* Physical Review D 42 2437

[45] Zener C (1937) *Internal friction in solids* Physical Review 52 230

[46] Nowick A S et al. (1972) *Anelastic relaxation in crystalline solids* Academic press New York and London

[47] Zener C (1948) *Elasticity and Anelasticity in Metals.* University of Chicago Press

[48] Willems P et al. (2002) *Investigations of the dynamics and mechanical dissipation of a fused silica suspension* Physics Letters A 297 37

[49] McLachlan N (1951) *Theory of Vibrations* Dover New York

[50] Logan J et al. (1993) *Aspects of the thermal motion of a mass suspended as a pendulum by wires* Physics Letters A 183 145

[51] Gonzalez G et al. (1994) *Brownian motion of a mass suspended by an anelastic wire* Journal of the Acoustical Society of America 96 207

[52] Young W et al. (2002) *Roark's formulas for stress and strain* McGraw-Hill

[53] Shackleford J H et al. (1999) *CRC materials science and engineering handbook* 3rd ed. CRC Press, USA

[54] Cagnoli G et al. (2000) *Damping dilution factor for a pendulum in an interferometric gravitational waves detector* Physics Letters A 272 39

[55] Barton M (2008) *Dissipation dilution* Private communication LIGO DCC T070101-00 1

[56] Robertson N et al. (2005) *Advanced LIGO suspension system conceptual design* Private communication LIGO DCC T010103-04-D 1

[57] Robertson N et al. (2002) *Quadruple suspension design for Advanced LIGO* Classical and Quantum gravity 19 4043

[58] Gonzalez G (2000) *Suspensions thermal noise in the LIGO gravitational wave detector* Classical and Quantum Gravity 17 409

[59] Jones R (2007) *private communication*

[60] Cantley C (2006) *Monolithic stage conceptual design for advanced LIGO ETM/ITM* Private communication LIGO DCC T050215-02-K

[61] Fritschel P (2001) *Advanced LIGO systems design* Private communication LIGO DCC 1

[62] Armandula H et al. (2004) *Silicate bonding, "ears", ribbon/fiber status / research and development plan* Private communication LIGO DCC T040170-00-D 4

[63] Jones R (2006) *Advanced LIGO_SUS_N-Ptype_refined ear (Type A)* D060055-02 Private communication LIGO DCC

[64] Armandula H (2004) *Ribbons / dumbbell fibers (moving from parallel to serial effort)* Private communication LIGO DCC LIGO-T040223-01-D 1

[65] Logan J et al. (1996) *Towards the development of monolithic fused silica suspensions for laser interferometric gravitational wave detectors* Eds. T Robert G Jantzen M Keiser and R Ruffini in proceedings of 7th Marcel Grossman Meeting World Scientific USA

[66] Gretarsson A et al. (2000) *Pendulum mode thermal noise in advanced interferometers: a comparison of fused silica fibers and ribbons in the presence of surface loss* Physics letter A 270 108

[67] Rowan S et al. (2000) *Fused silica suspensions for advanced gravitational wave detectors in gravitational wave detection II* Eds. S Kawamura and N Mio 2nd Tama Int. workshop on Gravitational wave Detection Tokyo Universal Academy Press Japan

[68] Cagnoli G et al. (2002) *Effects of nonlinear thermoelastic damping in highly stressed fibers* Physical Review B 65 174

[69] Cagnoli G et al. (2006) *Silica suspension and coating developments for Advanced LIGO* sixth Ediardo Amaldi Conference on Gravitational Waves Journal of Physics Conference series 32 386

[70] Lunin B (2005) *Physical and chemical bases for development of hemispherical resonators for solid-state gryroscopes* Moscow Aviation Institute Moscow

[71] Penn S D et al. (2006) *Frequency and surface dependence of the mechanical loss in fused silica* Physics Letters A 352 3

[72] Willems P (2002) *Dumbbell-shaped fibers for gravitational wave detectors* Physics Letters A 300 162